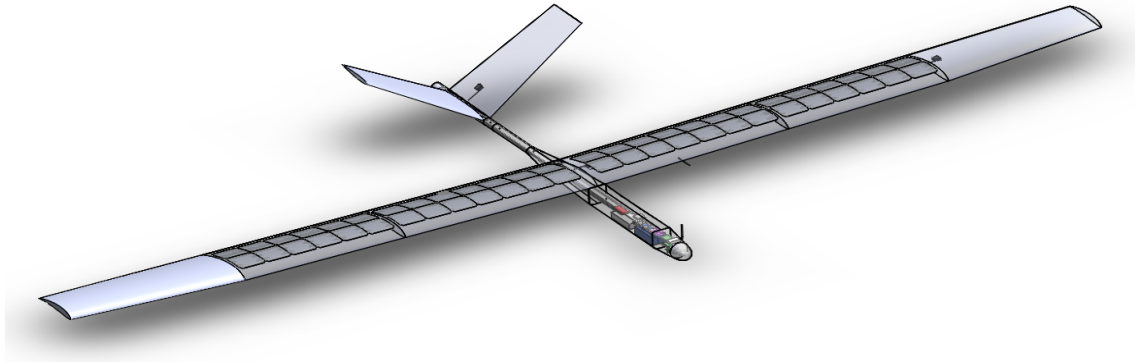# Conceptual and Preliminary Design of a Long Endurance Electric UAV

Luís Miguel Almodôvar Parada

Thesis to obtain the Master of Science Degree in

Aerospace Engineering

Supervisor: Prof. André Calado Marta

Examination Committee

Chairperson: Prof. Filipe Szolnoky Ramos Pinto Cunha
Supervisor: Prof. André Calado Marta
Member of the Committee: Dr. José Lobo do Vale

November 2016

Pela minha família, por ter permanecido.

Acknowledgments

First of all, I would like to express my gratitude to my thesis supervisor, professor André Calado Marta, for all technical guidance, patience and moral support throughout the period of time it took me to write this document.

Moving on to the extracurricular plan, a word of appreciation is due to the Autonomous Section of Applied Aeronautics (S3A). It was thanks to the work developed at this hands-on organization of students that I started gaining interest in model aircraft, which made me look at this thesis subject twice.

Furthermore, I want to thank a few friends and acquaintances that helped me through my academic life. Borrowed class notes, car rides, sleepless nights working for course projects, miraculous pieces of code, etc... all genuine contributions mattered.

Finally, I must dedicate this work to my family, the foundation that allowed me to harvest a higher education level. To my parents, for supporting me financially and emotionally, while respecting my decisions and daily struggles. To my grandparents, for diligently nurturing me over the years with all the resilience they could possibly seed. And last but not least, to my brother and to my sister, for being the best distractions of my life.

Resumo

A presente tese documenta o projeto conceptual e preliminar de um veículo aéreo não tripulado de grande autonomia movido a energia solar. Tendo em conta propósitos de vigilância, o perfil da missão requer uma subida inicial, a uma taxa que permita ascender 1000 m sobre pista em 10 minutos, seguido de voo nivelado com uma autonomia de 8 horas e um alcance de 200 km durante o equinócio. Na fase conceptual, várias configurações de aeronaves foram avaliadas considerando os requerimentos da missão. Recorrendo à metodologia de um processo analítico hierárquico, o conceito de avião com cauda em V e motor montado na traseira da fuselagem foi escolhido através de comparações emparelhadas entre os 10 critérios da missão (Aerodinâmica, Estruturas e Peso, Integração de Painéis Solares, Propulsão, Fabrico e Manutenção, Estabilidade e Controlo, Volume de Carga, Integração de Visão Remota na 1ª Pessoa, Descolagem e Aterragem, e Características Portáteis) e 8 possíveis configurações. Uma pesquisa no mercado dos UAV proporcionou uma estimativa inicial para o peso vazio e dimensões da aeronave. Através de uma pesquisa bibliográfica, o sistema de comunicações ficou definido de antemão e o sistema propulsivo também foi alvo de uma estimativa inicial. Durante o projeto preliminar, a aeronave foi redimensionada realizando um conjunto de iterações de ponto fixo, cujo ponto de projeto resultante garante que é fisicamente possível cumprir os requisitos do voo. Aliando múltiplas análises aerodinâmicas, realizadas numa ferramenta computacional que suporta baixos números de Reynolds, com a eficiência apurada para o sistema de propulsão, os consumos de potência de cada fase da missão foram determinados assumindo condições meteorológicas ideais. A energia solar recebida pelos painéis fotovoltaicos instalados foi determinada para uma única localização, aplicando um modelo teórico de irradiação em diferentes estações do ano. Verificou-se que no equinócio de Março a autonomia alcançou as 7.5 horas, enquanto que no de Setembro o seu valor máximo aumentou para quase 10 horas. Um conjunto das partes da aeronave foi desenhado em CAD sem detalhar soluções estruturais para o seu interior. As partes desenvolvidas incluem uma asa de três peças com 5 metros de envergadura, uma fuselagem composta por duas peças desmontáveis, perfazendo 1.9 metros de comprimento, e duas metades individuais de uma cauda em V. Os componentes aviónicos e do sistema de propulsão também foram modelados de forma simplificada no interior da aeronave, como sólidos de densidade uniforme. Uma análise de estabilidade de voo foi levada a cabo, resultando numa margem estática de 5.6% com C_m nulo em condições de voo nivelado. Visionando um futuro projeto detalhado, o envelope de voo cruzeiro foi gerado e a distribuição de pressão na asa foi obtida.

Palavras-chave: UAV Solar, Processo Analítico Hierárquico, Ponto de Projeto, Baixo Número de Reynolds, Autonomia, Envelope de Voo.

Abstract

The present thesis documents the conceptual and preliminary design of a solar long endurance Unmanned Aerial Vehicle (UAV). Having in mind surveillance goals, the mission profile requires an initial climb, at a rate that allows to ascend 1000 m above runway in 10 minutes, followed by cruise with an endurance of 8 hours and a range 200 km during the equinox. In the conceptual stage, several aircraft configurations were evaluated considering the mission requirements. Resorting to the Analytic Hierarchy Process methodology, the rear pusher V-tail airplane concept was chosen through pairwise comparisons between 10 mission criteria (Aerodynamics, Structures an Weight, Solar Panels Integration, Propulsion, Manufacturing and Maintenance, Stability and Control, Payload Volume, Remote-Person View Integration, Take-off and Landing and Portable Capabilities) and 8 prospective candidate configurations. A UAV market investigation provided an initial estimate of the empty weight fraction and airframe dimensions. Through bibliographic research, the communications system was defined beforehand and the propulsion system also received an initial estimate. In the preliminary design phase, the airframe was resized by performing a set of fixed point iterations, whose resulting design point ensured it is physically possible to fulfill flight requirements. Allying multiple aerodynamic analyses, performed on a low Reynolds number computational tool, with the ascertained efficiency of the propulsion system, power consumption at each mission stage was determined under ideal weather conditions. The solar energy received by the photo-voltaic arrays installed was determined in a single location applying a theoretical irradiation model in different seasons of the year. It was verified that in the March equinox endurance reached 7.5 hours, while in September its maximum increased to almost 10 hours. An aircraft CAD assembly was modeled without internal airframe detail. The developed parts include a three-piece 5 meter span wing, a fuselage composed by two connectable pieces, totaling 1.9 meter length, and two individual V-tail halves. On-board propulsion and avionics components were also modeled in a simplified way, as solids of uniform density. A flight stability analysis was performed, resulting in a static margin of 5.6% with null C_m in cruise conditions. Looking at a future detailed design, the cruise flight envelope was created and the wing pressure distribution was obtained.

x

Contents

List of Tables

List of Figures

Nomenclature

Greek symbols

α Angle of attack.

$\alpha_{0\,lift}$ Zero lift angle of attack.

γ Matrix eigenvalue.

Δ Difference between values.

δ Sun declination.

η Efficiency.

η_{camber} Cambered surface efficiency.

η_{energy} Energy collection sub-system efficiency.

η_{panels} Solar panels efficiency.

θ Pitch angle.

λ Stability mode eigenvalue.

μ Equivalent mass ratio.

μ_0 Atmospheric dynamic viscosity.

ν Dihedral angle.

ξ Damping factor.

ρ Density.

τ Torque.

φ Climb angle.

ψ Latitude.

Roman symbols

a Speed of sound.

A_{solar} Aircraft solar panels area.

AR Wing aspect ratio.

AR_H Horizontal tail aspect ratio.

AR_{V-tail} V-tail aspect ratio.

AoA   Angle of attack.

B Beam irradiance.

b Wingspan.

$\bar{c}$ Wing section mean chord.

C Battery capacity.

c Wing section chord.

C_D Three-dimensional drag coefficient.

C_d Two-dimensional drag coefficient.

C_I Consistency index.

C_L Three-dimensional lift coefficient.

C_l two-dimensional lift coefficient.

C_M Three-dimensional moment coefficient.

C_p Pressure coefficient.

C_R Consistency ratio.

$C_{D,0}$ Three-dimensional zero lift drag coefficient.

$C_{L\alpha}$ Three-dimensional lift vs angle of attack curve slope.

$C_{l\alpha}$ Two-dimensional lift vs angle of attack curve slope.

$C_{M\alpha}$ Three-dimensional moment vs angle of attack curve slope.

D Aircraft drag, Difuse irradiance.

d Square matrix dimension.

d_r Optical thickness.

E Energy.

E^* Mass specific energy.

E_e Daily irradiation.

f Frequency.

G Irradiance.

g Gravitational acceleration on Earth.

h Altitude.

h_0 Solar altitude.

I Electric current.

I_0 Solar constant.

j' Day angle.

K Response coefficient.

k_c Clear sky index.

K_n Static margin.

L Aircraft lift.

m Aircraft total mass.

$m_{actuators}$ Servos mass.

$m_{airframe}$ Airframe mass.

$m_{battery}$ Battery subsystem mass.

$m_{communications}$ Communication systems mass.

m_{opt} Relative optical air mass.

$m_{payload}$ Payload mass.

$m_{propulsion}$ Propulsion system mass.

m_{wiring} Mass of wires and cables.

n Load factor.

n_{gust} Gust load factor.

P Power.

p Pressure.

P_{solar} Network daily solar power.

R Aircraft range.

R^2 Correlation coefficient.

Re Reynolds Number.

RI Random index.

S Wing planform area.

S_H Horizontal stabilizer planform area.

S_V Vertical stabilizer planform area.

S_{V-tail} twice the V-tail semispan planform area.

T Thrust.

t Time.

t/c Airfoil relative thickness.

T_0 Stagnation temperature.

T_H Hour angle.

T_{LK} Linke turbidity.

T_n Transmission function.

$\hat{u}$ Absolute gust velocity.

U Velocity vector.

u Gust velocity normal component.

V Voltage.

W Aircraft weight.

x_{AC} Aerodynamic center longitudinal coordinate.

x_{CG} Center of gravity longitudinal coordinate.

Z_D Drag correction function.

Z_L Lift correction function.

Subscripts

∞ Free-stream condition.

c Clear sky conditions.

com Communication system.

D Dive.

h Horizontal surface condition.

i, j, k Computational indexes.

max Maximum conditions.

min Minimum conditions.

mvr Maneuver.

$prop$ Propulsion system.

PV Photo-voltaic condition.

s Stall.

x, y, z Cartesian components.

Glossary

AHP   Analytic Hierarchy Process.

ANAC   Autoridade Nacional de Aviação Civil.

APC   Advanced Precision Composites (propeller manufacturer).

ASSURE   Alliance for System Safety of UAS through Research Excellence.

AeroG   Aeronautics and Astronautics Research Center.

AoA   Angle of attack.

CAA   Civil Aviation Authority.

CAD   Computer-aided design.

CFD   Computational Fluid Dynamics.

CG   Center of Gravity.

CSM   Computational Structural Mechanics.

ESC   Electronic Speed Controller.

FAA   Federal Aviation Administration.

FAR   Federal Aviation Regulations.

FEM   Finite Element Method.

FEUP   Faculdade de Engenharia da Universidade do Porto.

GPS   Global Positioning System.

HALE   High Altitude Long Endurance.

IDMEC   Instituto de Engenharia Mecânica.

INEGI   Instituto de Ciência e Inovação em Engenharia Mecânica e Engenharia Industrial.

IST   Instituto Superior Técnico.

LAETA   Laboratório Associado de Energia, Transportes e Aeronáutica.

LALE   Low Altitude Long Endurance.

LEEUAV	Long Endurance Electric Unmanned Aerial Vehicle.
LLT	Lifting Line Theory.
LRS	Long Range System (radio control).
LTA	Lighter-than-air.
LiPo	Lithium Ion battery on a flexible polymer enclosure.
MAC	Mean Aerodynamic Chord.
MPPT	Maximum Power Point Tracker.
MTOW	Maximum Take-off Weight.
NP	Neutral Point.
OSD	On Screen Display.
PV	Photovoltaic.
RC	Radio Control.
RPV	Remote-Person View.
Rx	Receiver.
Tx	Transmitter.
UAS	Unmanned Aerial System.
UAV	Unmanned Aerial Vehicle.
UBI	Universidade da Beira Interior.
USA	United States of America.
VLM	Vortex Lattice Method.
VTOL	Vertical Take Off and Landing.

Chapter 1

Introduction

1.1 Motivation

Since a very early age in the History of Aviation, Mankind has shown notorious insight regarding the unmanned aerial vehicle (UAV) main philosophy - the absence of pilot in an aircraft. The earliest recorded endeavor to successfully operate an UAV dates from 1849, when Austria attempted to strike the Italian city of Venice with unmanned balloons loaded with explosives having time fuses to be dropped. The aerial bombardment ended up being inaccurate due to a change of wind that caused the balloons to drift away [1].

Indeed, lately, throughout the 20th century, the development of UAVs was triggered by military needs. Countless fixed wing UAVs, such as the Ryan Firebee in Figure 1.1, have been deployed during the Vietnam War, proving their usefulness for reconnaissance purposes. A few decades later, following the success of battlefield UAVs during the Gulf War, United States Military personnel fully recognized the worth of aerial unmanned systems [2].

Figure 1.1: Jet-powered surveillance UAV Ryan Firebee [3].

UAV settling in the daily routine environment could not possibly happen as fast. It is a fact that unmanned systems latent potential for civil applications has been perceived throughout the years, technically enabling missions involving Earth science research, land management, delivery tasks, amongst some other social and customer services. However, usage progress is far from being steadily estab-

lished because, unlike in the defense sector, where air space is properly prepared and the completion of the mission is supra to the economics of the vehicle, for civilian procedures cost sustainability and operational complexity are still major barriers.

Most existing mission profiles for modern UAVs require a platform, or series of platforms, which clearly extend range and endurance beyond the capability of existing affordable electric vehicles. At the same time, the use of renewable energies in vehicles is becoming more and more demanding by society due to its growing environmental awareness. Taking this factors into account, it has become clear in the last years that the key to enhance UAVs long endurance capabilities can be found within solar aviation.

Nowadays, with the relatively easy access to numerical and experimental design tools and with the current efficiency of electric systems (solar panels, motors and batteries) there is a real chance to expand UAVs applications. The aim of this thesis is to achieve the preliminary design of a solar powered UAV, meant to be used for long endurance civilian surveillance missions.

1.2 UAVs in Contemporary Society

The UAV sector is dynamically expanding at a quick pace in the aerospace industry, with predictions that point towards that tendency over the next years. According to an analysis released by an independent information provider, the global defense and security market for UAVs will expand at 5.5 percent per year over this decade, almost doubling from the current Figure to $10.4 billion by 2024 [4]. On the civilian side, small drones mass consumer market appeal has skyrocketed sales. The safe integration of unmanned systems into air space is an issue that revolves around creating mechanisms to handle the lack of regulation for people flying drones, whether they are amateurs or specialized operators.

Nevertheless, more and more people, organizations and institutions have felt encouraged to come up with new ways for drone technology to revolutionize society. A large set of fields in which drones are increasingly present can be summarized as follows:

- Environmental monitoring: UAVs have been used as platforms to access data concerning meteorology, the state of ecosystems or geological phenomena. During a volcanic eruption at island of Fogo, in Cape Verde, the company TEKEVER used small drones to capture images in high definition and with thermal imaging cameras. This course of action allowed local authorities to predict the advance of lava with certainty [5]. Another example can be found in the university of Aveiro, that has developed a UAV to monitor forests. The drone uses a multi-spectral sensor that allows the detection of effects such as drought, diseases and fungi on trees [6].

- Transportation of goods: Many drone-based delivery systems are being tested and conceived by renowned companies. Amazon intends to use small UAVs to safely get ordered packages into customers hands in 30 minutes or less [7]. DHL is working on a parcelcopter to perform emergency delivery of medications and other urgently needed goods [8].

- Medical services: The contribute drones can give to medical services around the globe can go beyond medication transportation. Alec Momont of TU Delft's Faculty of Industrial Design Engi-

neering designed a prototype of an ambulance drone. It can quickly deliver a defibrillator to where it is needed with the presence of the emergency operator via the drone's loudspeaker, which significantly increases the chance of survival following a cardiac arrest [9].

Figure 1.2: Ambulance drone [10].

- Wildfire combat: There have been several reports of drone hobbyists interfering with fire fighting aircraft operations in California [11]. Such episodes illustrate the need to further regulate the use of UAVs. Notwithstanding, drones usefulness to battle wildfires is starting to be recognized by the proper authorities [12, 13]. Lockheed Martin's unmanned helicopter K-MAX is an available solution capable of aerial fire suppression. It maintains its capabilities in hot temperatures and can provide automated water pick-up, delivery, and line-building [14].

- Agriculture: The market variety for drones with technology used for inspection of farms is increasing in such a way that the United States based Association for Unmanned Vehicle Systems International predicts that agricultural uses will eventually account for 80 % of the commercial market for drones [15]. Spraying crops is also a possible use for drones, the Yamaha RMAX is an exemplar used in Japan for seeding and spraying rice [16].

- Structures surveying: Aerial imaging capabilities facilitate the detection and resolution of issues in large structures with difficult access, while reducing costs and risks. Bridges, train lines, solar farms, wind turbines, oil and gas pipelines, dams, cooling towers and monuments can all be inspected using unmanned systems. In recent years, the company Albatroz Engineering has been involved in several technical and scientific publications concerning small UAV systems capability to perform power line maintenance inspection [17, 18, 19, 20, 21].

- Natural disasters response: Surveillance capabilities have also allowed UAVs to monitor devastation areas, making damage assessments and searching for survivors [22, 23].

- Social Media: Unmanned aerial technology allows to cover news and social events, like sports or festivals, from a different perspective. Shooting of advertisements and movies can also be originally engineered with drones [24].

- Law enforcement: Police forces have deployed UAVs for patrolling borders and surveillance roles during major crowd events [25, 26].

1.3 UAV Operation Legislation

With Unmanned Aerial Systems (UAS) assuming a wide variety of new applications worldwide, regulating the sector became an unavoidable issue for governments. Australia pioneered with the first operational regulation for unmanned aircraft set back in 2002 [27]. In the last few years, UAV operation regulations have been emerging across the globe, assuming different formats in major economies.

In the United States of America (USA), non-recreational civilian UAV operations are prohibited without a special clearance from the Federal Aviation Administration (FAA). In order to efficiently integrate unmanned aerial systems into the USA Airspace with minimal changes to the current system, the FAA formed the Alliance for System Safety of UAS through Research Excellence (ASSURE), a partnership with 22 research institutions, including Mississippi State University (manager member), Embry-Riddle Aeronautical University and Kansas State University, So far ASSURE has been allowing more advanced UAS research and operational concept validation in six designated test sites, namely, North Dakota Department of Commerce, State of Nevada, University of Alaska Fairbanks, Texas A&M University Corpus Christi, Virginia Polytechnic Institute & State University and Griffiss International Airport [28, 29].

In the United Kingdom, anyone who wishes to operate an UAV for non-recreational purposes needs a permission from the Civil Aviation Authority (CAA), which requires a demonstration of sufficient understanding of aviation theory and a practical flight assessment. The CAA approves several national qualified entities that run assessment courses and make formal recommendations about the pilot's competence. Additionally, authorizations for regular UAV flights also depend on the submission of an operating manual to the CAA for permanent approval [30, 31].

European regulations of civil aviation sector do not include UAV categories below 150 kg, for that reason it is up to each country to create such specific set of laws [32]. In Portugal, the national authority of civil aviation (ANAC) has been finalizing a legislation proposal, in which the access of UAVs to segregated aerial space would be limited, depending on required authorizations from ANAC. Portuguese companies remain generally concerned, as the existent legal void brings difficulties with flight insurances and uncertainty to the industry sustainability [33]. A discussion on the regulation of UAV flights has been presented by ANAC in [34].

1.4 Solar Powered UAVs

Solar power is ordinarily recognized as the most innovative feature brought from the field of renewable energies to aviation. A solar powered aircraft can in theory fly for an indefinite period of time as long as it has an energy storage system to maintain its flight and other activities when no sufficient solar radiation can be collected into electric energy by its solar panels.

However, solar photovoltaic cells are not very efficient, the consequence being is that the airframe will require larger wing area in order to accommodate the photovoltaic cells needed for charging electric batteries. A lightly built structure is also a common characteristic that contributes to fulfill lower power requirements.

Given the mentioned particulars, along with the knowledge that for a given energy storage electric batteries occupy up to four times the volume of that of fossil fuels [35], the first solar aircraft would certainly be an UAV. It was in the 4th November of 1974 that project Sunrise, developed by Roland Boucher of Astro Flight in California, took off as the first solar powered radio controlled aircraft [36]. With a wingspan of 9.76 m and a maximum take-off weight of 12.25 kg, it flew for 20 minutes at an altitude of around 100 m. Sunrise I made other flights, lasting 3 to 4 hours, until it was severely damaged during a windstorm later that winter. In September of 1975, the second version, Sunrise II, made its first flight with more efficient solar cells and the weight decreased by more than 2 kg. Despite all the improvements, Sunrise II met its end due to a control system failure. In spite of the adversities, this pioneer project disclosed the potential of solar aviation, leading the way for future works.

In the years that followed dozens of solar UAVs were conceived, but it was the performance of an improved manned solar airplane, the Solar Challenger, who covered 262.3 km in 5 hours and 23 minutes with no inboard energy storage system, that led the US government to fund the study of high altitude long endurance (HALE) platforms [37]. AeroVironment Inc. was left responsible for the project, coming up with Pathfinder in 1993. This solar-powered UAV was built primarily of composites, plastic and foam and had solar arrays covering most of the upper wing surface. Since it did not have rudder, roll and yaw control were accomplished by slowing down or speeding up the motors on the wing.

(a) Pathfinder [38].

(b) Helios [39].

Figure 1.3: HALE UAVs built during NASA ERAST program.

In 1994, Pathfinder became a part of NASA's Environmental Research Aircraft Sensor Technology (ERAST) program, reaching an altitude of 15392 m in 1995, such value would increase two years later to 21802 m [38]. From there on, NASA built more UAVs from the same family, Centurion (1997-1999) [40], Pathfinder plus (1998-1999) [38] and Helios (1999-2003) [39]. In 2001, Helios achieved an unofficial world-record altitude of 29524 m, but two years later its final prototype disintegrated in mid air due to structural failures, falling towards the Pacific Ocean.

Another developed HALE platform that proved that the power of the sun can be successfully used to fly a plane for considerable periods of time is Zephyr [41]. This series of lightweight solar-powered UAVs was originally designed and built by the United Kingdom company QinetiQ and is actually part of the Airbus High Altitude Pseudo-Satellite programme. The last prototype built in 2010, Zephyr 7, with a wingspan of 22.5 m and a loaded weight of 50 kg, holds the official record for an unmanned aerial vehicle for a flight that lasted about 2 weeks [42].

More recently, the Facebook company has been developing a stratospheric solar-powered drone, named Aquila, meant to stay airborne for several months, providing internet infrastructures in remote

parts of the world. Aquila is a delta flying wing with 42 m wingspan and 4 wing mounted engines. It weighs a third as much as an electric car and about half its mass is devoted to batteries. The internet is intended to be transmitted in the form of free-space optical communication, which passes on data using infrared laser beams. In June of 2016, a full-scale prototype of Aquila completed its first test flight, having flown 96 minutes at low altitude [43].

Figure 1.4: Facebook's drone Aquila in flight [43].

Google also has aspirations of providing internet services to remote areas with solar HALE UAVs. The unmanned Solara 50, built by Titan Aerospace, the company Google acquired in 2014, crashed during a flight test on May 1st 2015 shortly after take-off on Albuquerque, New Mexico. It is a conventional configuration airplane with one engine upfront that has a wingspan of 50 m and a payload of 32 kg. With an estimated endurance of 5 years, Solara 50 was intended to function as an atmospheric satellite with laser technology. In spite of the drawback, Google is going to continue developing the solar-powered stratospheric unmanned aircraft for internet delivery. [44, 45]

Low Altitude Long Endurance (LALE) UAVs are often limited to small-scale applications due to their low flight endurance. The Suiss Federal Institutes of Technology have been addressing that issue by administrating research projects concerning solar LALE UAVs. One of those is the Sky-Saylor, a conventional tractor with V-tail designed to support planet Mars exploration. It was developed by André Noth under its PhD thesis, from 2004 to 2008, ending up with a wingspan of 3.2 m and a total take-off mass of 2.444 kg. In june 2008, this small aircraft, built with carbon and aramid fiber and balsa wood, made a continuous flight of more than 27 hours, incorporating solar cells with an efficiency of 16.9 % [46].

(a) Sky-Sailor [47]   (b) AtlantikSolar [48]

Figure 1.5: LALE UAVs developed with the support of Suiss Federal Institutes of Technology.

The AtlantikSolar is a more recent project, started in 2012 and coordinated by ETH Zurich, it aims for the first transatlantic flight of a solar powered UAV. The final planned flight route goes from Bell Island (Canada) to Lisbon (Portugal), making a 5000 km distance. The actual prototype is a 5.6 m wingspan T-tail tractor with 88 SunPower C60 cells (up to 22.8 % efficiency) installed on the wing. Its wing and stabilizers were built with a traditional rib-spar construction method. The wing's main element is an

inner cylindrical carbon-fiber spar to resist torsional wing loads. Four carbon-fiber belts of trapezoidal and laterally-varying cross-section are attached to the spar to optimally resist bending loads and to provide maximum wing stiffness to avoid bending of the solar cells [49, 50]. In the 2nd of July 2015, in Switzerland, the fourth flight test of the AtlantikSolar 2 (AS-2) took place, in which the aircraft made its first day/night flight, flying 28 hours. Only 16 days later at the same place, AS-2 established a new milestone for LALE aircrafts for flying continuously its 6.8 kg during 81.5 hours. Future work for the AtlantikSolar project is going to focus on extended endurance flights with payloads including optical and infrared cameras as well as atmospheric sensors [51].

Development of manned solar aircraft has always presented more challenges when compared to UAVs. All increased difficulties related to enlarged payloads, required power, airworthiness and funding makes the amount of solar manned aircraft developed so far substantially low. Major progresses have been made though, a remarkable example is the project Solar Impulse, a piloted long range solar aircraft made with the purpose of circumnavigating the Earth with several planned stops [52]. So far, the Solar Impulse has developed two airplane prototypes. The first one, HB-SIA, had its flight debut on 2010 and its first night flight (that lasted about 26 hours) on July of the same year, many other demonstration flights with this aircraft followed across Europe, Morocco and America. The second version of Solar Impulse, HB-SIB, possesses four high density energy electric batteries and engines, a wingspan of 72 meters, a unladen weight of 2300 kg and more than 17000 solar cells spread across the wings, fuselage and horizontal stabilizer.

(a) Flying over Abu Dhabi

(b) Finished landing in Hawaii

Figure 1.6: Solar Impulse 2 [52]

HB-SIB, presented to the public in April 2014, has successfully circumnavigated the globe. It departed from Abu Dhabi in March of 2015 and made 17 legs, while breaking records such as the longest solar powered straight distance and free distance flight. It finished the Round-The-World mission by returning to Abu Dhabi in July of 2016 [53].

1.5 Project Background

This work started as a part of a project of a Long Endurance Electric Unmanned Aerial Vehicle (LEEUAV) that is being developed with the collaboration of three research centers: Aeronautics and Astronautics Research Center (AeroG) at Universidade da Beira Interior (UBI), Instituto de Engenharia Mecânica (ID-MEC) at Instituto Superior Técnico (IST), and Instituto de Ciência e Inovação em Engenharia Mecânica e Engenharia Industrial (INEGI) from Faculdade de Engenharia da Universidade do Porto (FEUP). All

units involved are a part of Laboratório Associado de Energia, Transportes e Aeronáutica (LAETA).

The main goal of the project is to develop a low cost, small footprint electric UAV, that is capable of being deployed from short airfields, easy to build and maintain, and highly flexible to perform different civilian surveillance missions. The main UAV specifications include:

- Long Endurance: accomplished by using green power technologies such as an electric propulsion system with solar power. This includes the use of highly efficiency solar cells, high capacity/density batteries, efficient compact motors and appropriate long endurance aerodynamic design;

- Autonomous Flight: accomplished by equipping the UAV with autopilot navigation systems such as inertial guiding systems and GPS;

- Obstacle Avoidance: accomplished by implementing an obstacle avoidance technique that includes detection, estimation, and avoidance planning of the obstacle;

- High-strength, Low-weight Structure: accomplished by using composite materials, with fuselage/wing critical areas designed for good impact resistance on landing, using easy to manufacture techniques;

- Multiple Mission: accomplished by designing a sufficiently large payload range capability and developing upgradable modular avionics, to enable an easy software upload and/or hardware swap to meet the selected mission requirements.

To achieve the specifications and requirements of the UAV, several tasks have already been addressed, namely:
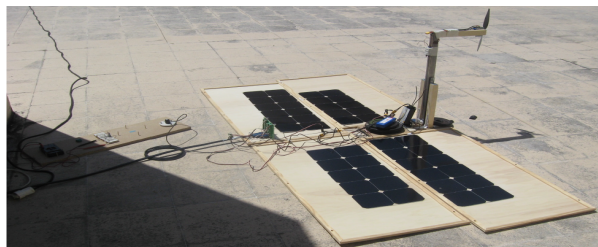
Figure 1.7: Assembly used to test the propulsion system [54].

1. Propulsion System - In this task several different electric propulsion system configurations were evaluated in terms of performance, overall weight and cost. The selection of solar panels was followed by the selection of possible brushless motors. A secondary energy source was considered in the form of high-density rechargeable batteries. Thus, an hybrid alternative to the all-electric system was also evaluated. Two master students, Héctor Vidales and Tiago Ferreira, have already poured over this work, as part of their master's dissertations [55, 54]. Figure 1.7 shows the most recent apparatus used to test the hybrid propulsion system. This task is nearly accomplished and by the end of it, the propulsion system configuration will be selected and the auxiliary available power for electronics estimated;
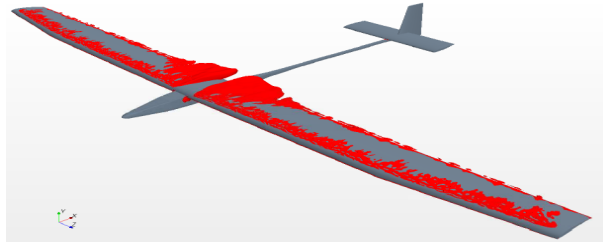
Figure 1.8: Wing flow separation in a conventional configuration UAV, AoA=8° [35].

2. Aerodynamic Design - Using high-fidelity Computational Fluid Dynamics (CFD) analysis, the aero-dynamic design will define the wing geometry keeping in mind the solar panel dimensions. The fuselage and tail will also be modeled. For this purpose, a computational process to enable the swift design of different UAV configurations and their aerodynamic analysis has been developed by Nuno Silva as part of his published master's dissertation [35]. Figure 1.8 displays a CFD analysis output obtained for the wing of a conventional configuration UAV;

(a) UAV testebed.

(b) Ground station.

Figure 1.9: UAS communications testing equipment [56].

3. Communication and Electronics - In this task the communications and electronic systems were designed. Autopilot and Remote Person View hardware and software design have been subject of work in two other published master thesis, written by Duarte Figueiredo and Pedro Miller, respectively [57, 56]. Figure 1.9 shows the latest setup used to test the communications systems;

(a) Wing structure manufacturing.
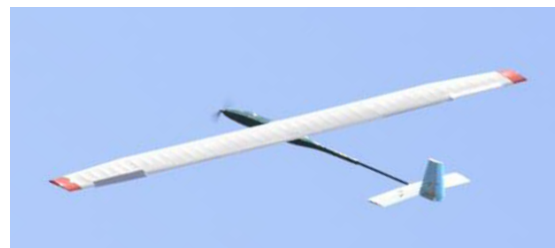
(b) LEEUAV prototype in flight.

Figure 1.10: Development of the first generation LEEUAV in UBI [58].

4. Manufacturing - A first generation prototype has been built under a master's thesis from UBI written by Luís Cândido [58]. Using advanced building techniques, airframe parts, such as the wing in figure 1.10a, were manufactured. Although that prototype is far from being final, the construction tests that were performed allowed to reach relevant conclusions related to applicable materials and manufacturing processes;

5. Flight Testing - The prototype built in UBI had its systems checks on ground and was also test flown, as seen in figure 1.10b, while being operated with radio controlled mode. Again, in spite of not being the final prototype, important qualitative performance knowledge was attained for a prospective solar UAV configuration.

1.6 Thesis Objectives

The purpose of this thesis is to perform preliminary studies regarding the feasibility of a small wingspan electric solar UAV for surveillance missions. In an early stage, it will be a priority to generate the best concept, that accommodates enough electric power, with solar panels installed on its airframe, to fulfill a specific endurance requirement for a given scenario of useful payload. Then, by allying knowledge from previous related works with data obtained from a UAV market research, an initial estimate will be gauged for the dimensions, weight fractions and on-board systems of the LEEUAV.

Thereafter, the aircraft design will undergo an iterative process in which its aerodynamic, propulsion and flight stability characteristics will be progressively evaluated and readjusted as a whole until all mission requirements are met. For that to be possible, a swift aerodynamic computational analysis method will have to be arranged, as well as CAD assembly modeling tools. Knowing that endurance depends on the solar energy available, a daily irradiation model will also have to be conceived.

Once the preliminary design comprises converged airframe external dimensions along with all on-board systems, the cruise flight envelope and an associated wing load distribution estimate are expected to be retrieved for a prospective detailed structural design.

1.7 Document Outline

The work presented in this thesis is divided into seven chapters. The first chapter consisted foremost in an overall description of the growing applicability of UAVs in worldwide society, while addressing benefits and issues and how the incorporation of renewable energies on aircraft evolved over time. Moreover, came a brief introduction of the LEEUAV project.

The second chapter deals with the selection of the airframe concept that best fits the LEEUAV mission. In the third chapter, the initial sizing of the airframe dimensions takes place. It includes a summarized description of the first generation LEEUAV, an introdution of all on-board systems as well as a mass estimation model for the airframe.

Chapter 4 handles preliminary project where several iterative calculations were performed to define the final dimensions of the LEEUAV and the correspondent assembly of flight systems. Chapter 5 appears as an extension of the preliminary project dedicated solely to solar energy management.

Chapter 6 describes some extra work that has been done in preparation for a future detailed design. It includes computational treatment of wing loading data and CAD modeling aspects.

Finally, Chapter 7 features concluding remarks providing a working balance of what has been achieved in this thesis. Coupled with that there are also recommendations for future works.

Chapter 2

LEEUAV Concept

The conceptual design stage is one of the most determinant tasks of the Long Endurance Electric UAV (LEEUAV) project. The mission is thoroughly described and afterwards several different configurations are evaluated to meet or exceed the mission requirements in terms of endurance, size and cost. By the end of this chapter, one airframe configuration is selected to become the basis of a further refined design.

2.1 Project Requirements

The particular requirements of the LEEUAV project were deliberated having in mind the ultimate goal of flying for a long time with low power requirements while carrying a payload of up to 10 N.

Specific mission requirements are summarized as follows:

- Climb 1000 m in 10 minutes, which corresponds to a climb rate of approximately 1.667 m/s. At the average altitude of the Portuguese locations considered, displayed in Appendix A, flying at 1300 m altitude allows the RPV camera to record ground footage with acceptable resolution display. Bearing that in mind, for computation purposes it is assumed that the take-off altitude and the project service ceiling are fixed at 300 m and 1300 m, respectively;

- Fly for 8 hours in the equinox (21 March or 21 September) and reach a range of 200 km. This requirement obliges the aircraft to travel at a speed equal or greater than 6.94 m/s. To increase the margin for mission accomplishment, the project's cruise speed was augmented to 7.53 m/s;

- The aircraft's size must allow operations in very small airfields (eventually no airfield will be required). Take-off can be done by hand-launching or using a ground support system purposely designed for that purpose;

- The UAV must possess portable capabilities that allow small vehicle transportation on the ground;

- The minimum bank angle for the aircraft's turn is 45º, with an associated load factor of 1.414.

2.2 Mission Profile

The mission starts with take-off at any altitude, followed by climb until the defined steady flight altitude. Cruise is the longest phase of the mission in which there must be a time window of 8 hours to fly over specified locations and to turn around, returning to base. Descent and landing can be executed with thrust, but it is preferable to have those stages performed with negligible energy consumption (i.e. by gliding). Occasionally, loiter may be needed before landing. The mission profile scheme is represented in Figure 2.1.
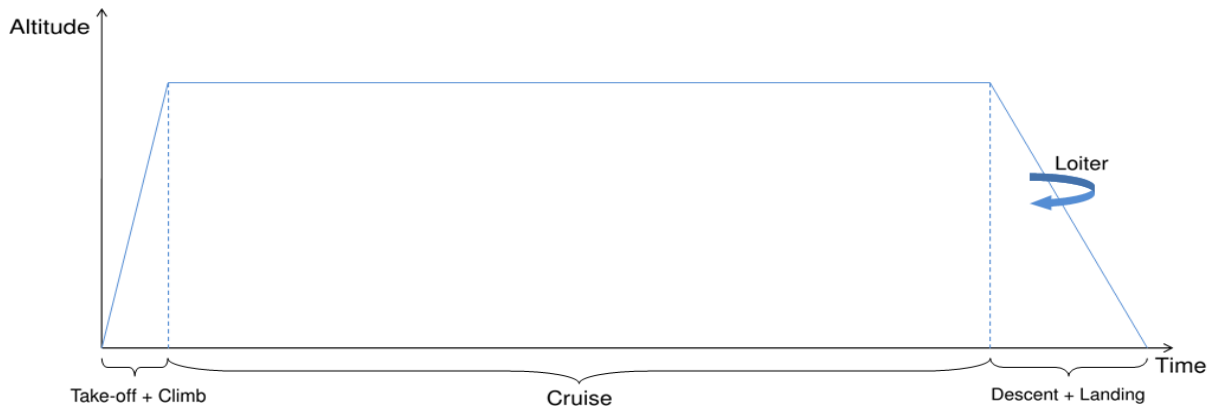
Figure 2.1: Representative scheme of the LEEUAV mission.

The flight stage altitude is characterized by temperature and pressure, presenting derived atmospheric parameters such as density, sound velocity and dynamic viscosity. For this mission's route, it is assumed that these parameters vary according to the International Standard Atmosphere model (ISA). Atmosphere parameters for take-off at several Portuguese airfield locations and different cruise altitudes are presented in Table A.1 in Appendix A.

2.3 Airframe Concept Generation

UAVs come in many shapes and sizes, having their own unique advantages and disadvantages. Only by understanding those key attributes, the surveillance mission can be accomplished with success. In order to decide which platform best fits the application, four main types of UAVs have been analyzed: rocket types, lighter-than-air, rotary-wing and fixed-wing.

2.3.1 Rocket Configuration

Rocket engine vehicles obtain thrust by Newton's principle of action and reaction, expelling the exhaust backwards, typically at extremely high speeds. Due to their typical axisymmetric geometry shape with a nose cone at the top and increased fineness ratio, along with aft-swept wings with low aspect ratio, rockets are a design solution for supersonic and hypersonic flight regimes and the only one so far that allows launching devices outside the Earth's gravitational pull. Naturally, all existing operational research rockets far exceed the LEEUAV mission requirements and constraints in terms of dimensions,

payload, altitude, velocity and budget. Adaptations for a design aiming much lighter payloads and lower ceiling altitudes, near 2000 m, can be arranged in a sustainable way by applying high-power rocketry construction techniques, suitable for take-off weights above 1.5 kg [59, 60]. However, there are still major technological and physical restrictions that disable the feasibility of an electric rocket drone configuration for this specific mission.

Since rockets have very low wingspan, they must rely on extremely high exhaust speeds to remain stable in horizontal flight. For that reason, cruise cannot take place at low speeds. Figure 2.2 illustrates the differences between high powered rocket's typical flight pattern and the mission profile. A standard high power rocket reaches the apogee when all propellant is spent. Ideally, on an electric powered rocket, there would still be plenty energy to satisfy the 8 hour endurance requirement, however, to keep it from surpassing the mission ceiling the impulse would have to be gradually diminished, describing the same ascending pattern as a chemically powered rocket. Then, only a huge increase of thrust would allow the transition to high speed cruise, which is not only technologically unattainable, but also not fit for long endurance surveillance missions.
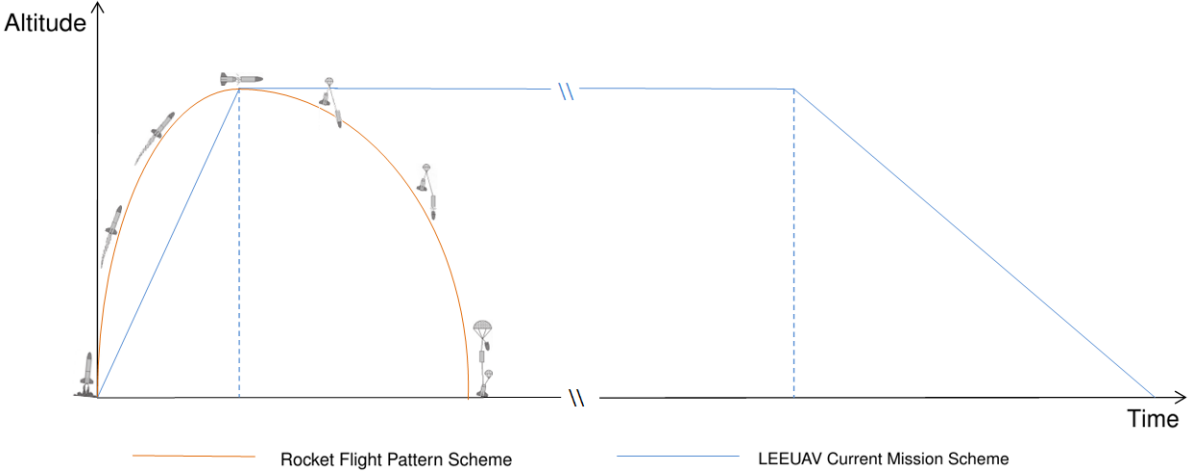
Figure 2.2: Comparative scheme between rocket flight pattern and LEEUAV mission.

Usually, following the climb phase model rockets descend. To prevent destructive landing, a dual deployment technique can be used [61].

It is noted that take-off and climb may be attainable for electric rockets in the future, if technological progress concerning electric powered propulsion in high-power rocketry occurs. On the other hand, their descent and landing already have practical means of being executed. Notwithstanding, the incapacity to cruise at low speed is the main cause that dooms rockets has an impracticable design for the LEEUAV mission. For those reasons, rockets are categorically excluded as a conceptual option.

2.3.2 Lighter-Than-Air Configurations

Lighter-than-air (LTA) aircraft, also known as aerostats, acquire aerostatic lift through the positive difference in the pressure between atmospheric air and an enclosed buoyant gas. Thanks to such particularity, aerostats may remain airborne for long periods of time without being mechanically powered. In

spite of that, a simple balloon configuration will not satisfy the current mission profile because it lacks a propulsion system and effective control surfaces for a controlled powered flight, as well as a favorable aerodynamic shape to keep a steady velocity above 6 m/s.

Aerostat designs that make up for the missing features of balloons arise in the form of airships. Having an elliptical revolution envelope with dimensions that far exceed the size of their payloads, airships may come equipped with electric engines and empennage that grant small speed steered flight.
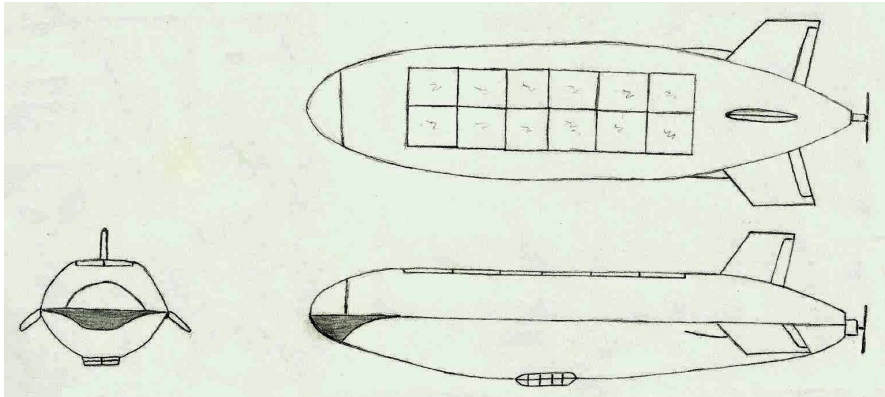
Figure 2.3: Design sketch of a rigid solar dirigible.

The solar dirigible design sketched in Figure 2.3 presents an empenage, a pusher propeller on the back and a gondola to carry communication systems and remaining payload. Assuming that the envelope will have a full structural internal framework, its upper surface may be used to harbor a large set of semi-rigid photo-voltaic arrays, that will be necessary to power cruise through long periods of time.

A rigid design comes with an increased weight penalty and changeless volume that makes ground transportation within small vehicles impossible. Nonetheless, the most critical disadvantages are performance related. Even considering a low speed mission, the drag coefficient generated as consequence of the large envelope still increases greatly when compared with other subsonic aircraft configurations, imposing more energy consumption to navigate at velocities much greater than 6 m/s. Moreover, attending to the small control surfaces in comparison to the whole airframe, the dirigible becomes susceptible to aggravated stability limitations when performing maneuvers or encountering gusts.

Accordingly, in the event the UAV needs to promptly increase velocity or execute a maneuver, to avoid harmful weather conditions or to make an urgent return to base for instance, the dirigible concept presents severe limitations. For those motives, along with ground handling disadvantages, the solar dirigible was not chosen as a LEEUAV concept.

On an additional note, it is observed that if an LTA UAV were to be projected, hydrogen could emerge as main lifting gas. The earth's lightest element can easily be produced with modest costs and has 8% more buoyancy in comparison with the more expensive inert helium gas, preferred to fill manned airships. In fact, flammability properties prevents hydrogen from being used in modern manned LTA aircraft, however an electric UAV may bring more favorable gas retention conditions that ensure airworthiness. All facts considered, the difference in specific density between both gases can translate into huge energy savings for long endurance missions.

14

2.3.3 Rotary Wing Configurations

In a rotary wing airframe blades revolve around the fuselage's vertical axis, generating vertical thrust, opposing the aircraft's weight, horizontal propulsive force and other forces and moments to control the attitude and position in three-dimensional space. Rotary wing UAVs come in wide range of rotor setups, including helicopters, quadcopters, hexacopters, as well as more unusual configurations.

This sort of UAV's most distinct characteristics are the ability to perform vertical take-off and landing (VTOL) and their capacity to hover and perform agile maneuvering. With those, rotary wings allow operations in small areas, with no substantial landing or take off area required, while granting greater flexibility with the payloads deployed. Nowadays there are several minimalist VTOL designs specially conceived for detailed inspection work, surveying closely hard-to-reach areas or transportation of goods in urban environments.

Nonetheless, scenarios that require maneuvering around tight spaces or the ability to closely maintain visual on a single target for extended periods clearly diverge from the mission profile described in Section 2.2. VTOL hovering and agile maneuvering are non-essential capabilities that come at the expense of high mechanical complexity and increased shaft power. Additionally, due to the present glide impossibility, a rotor system would need to constantly provide power throughout all stages of the mission, including descent and landing. For those reasons, power consumption increases and endurance tends to be significantly lower in VTOL configurations.
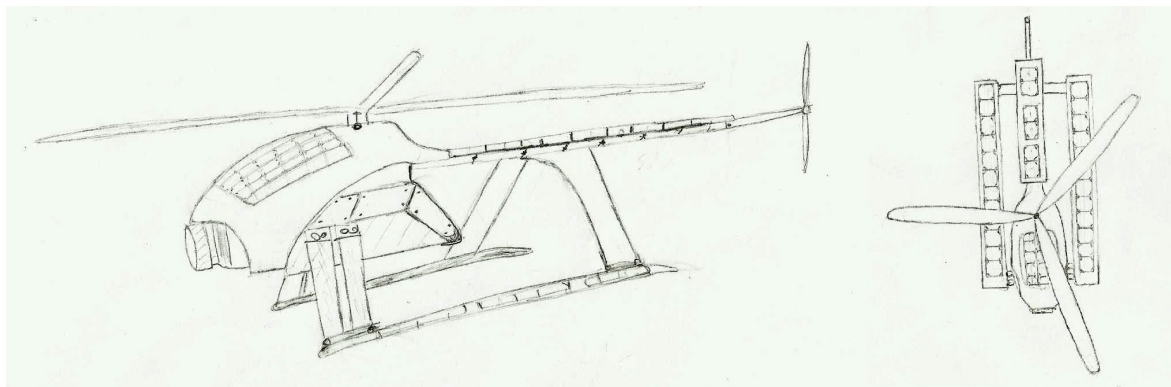
Figure 2.4: Design sketch of a solar helicopter.

Not likely to be chosen as a concept, a rotary wing UAV can still be effectively projected to obtain additional power by means of solar source. The helicopter design sketch present in Figure 2.4 has photo-voltaic arrays incorporated on larger skids and on a support structure attached above the tail. Also, flexible panels are installed on the fuselage front surface. The biggest drawbacks in the solar helicopter concept come from the unavoidable increase of wetted area and addition of further structures, that raise drag and the required lifting power.

Considering an eventual solar quadcopter, as the one in Figure 2.13a, the aerodynamic penalties that come from increasing whetted area can be attenuated when compared to the solar helicopter. The reason being is that the installation of solar panels will not require any further structures directly below the wakes generated by the propellers.

15

2.3.4 Fixed Wing Configurations

In every electric-powered airplane, propellers convert rotary motion into horizontal thrust, causing the vehicle to move forwards. With the resulting velocity, lift is obtained through wings, due to the pressure difference, explained by Bernoulli's principle, between lower and upper camber surfaces.

An high aspect ratio wing is an optimizing feature in airplanes operating at low subsonic speeds as it confers a smaller induced drag component. As a result, gliding is enhanced, that leads to energy savings. Conversely, a longer wing also brings less maneuverability, given that it has a higher moment of inertia to overcome in a steady roll, which is not critical for the current mission profile.

Aside from being an aerodynamic asset, a solar airplane's wing must also become a platform to install photovoltaic cells with unobstructed access to solar radiation during all day, to increase energy collection. Biplanes, winglets, endplates, upswept wings and C-wings are all avoidable design options because of the shadow they can generate, specially at the earliest and latest hours of sunlight.

Having in mind all aforementioned solar airplane design recommendations, practicable design configurations are discussed in qualitative terms of performance in the following subsections.

2.3.4.1 Conventional Derived Concepts

A conventional airplane configuration presents a single fuselage, as main body section that carries most cargo, an empennage that is a set of control and stabilization surfaces located to the rear, and a wing placed further ahead on the fuselage. As shown in the example of Figure 2.5, a high wing position has been adopted for all conventional concepts, not only to increase the available area for solar panels but also to facilitate disassembly.
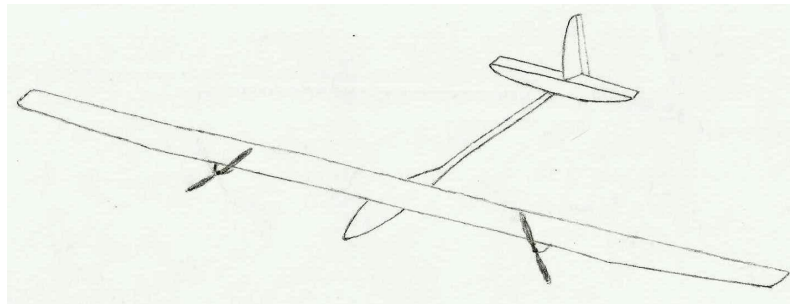
Figure 2.5: Design sketch of a conventional configuration UAV with twin wing-mounted engines

A conventional design tail, also known as inverted T-tail, portrayed in Figures 2.5 and 2.6a, has a vertical stabilizer and an horizontal counterpart, placed near the fuselage longitudinal centerline. Such positioning adds more flexibility to the design in terms of stability behavior since it minimizes the components of the moment, with respect to the center of gravity, created by the elevator during pitch control.

Alternatively, the horizontal stabilizer could be placed above the vertical tail, like in Figure 2.6b, where it stays clear from the main wing wake and propeller wash. The major disadvantage of a T-tail is that its vertical piece must be strengthened to support the load of the horizontal part, turning the whole empenage heavier. An increased tail weight may become a stability issue that is only rectified with a redistribution of other masses in the aircraft and/or a change in the longitudinal position of the wing.

| a: Inverted T-tail. | b: T-tail. | c: Cruciform tail. |

| d: V-tail. | e: Inverted V-tail. | f: Inverted Y-tail. |
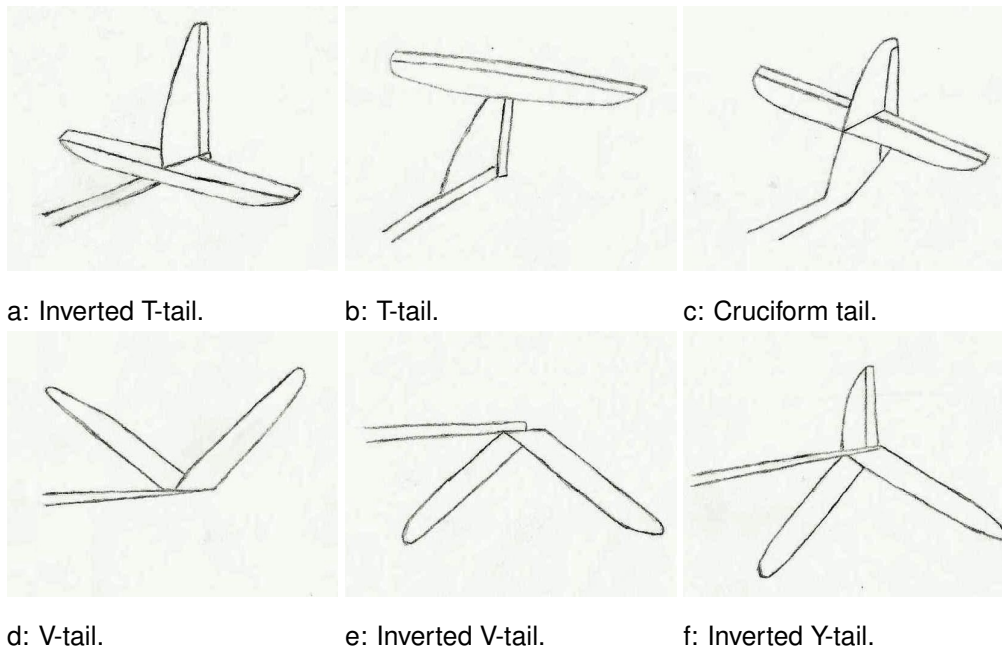
Figure 2.6: Several single fuselage tail configurations.

To benefit from an elevator's upper position while lessening the weight penalty, a cruciform tail could represent an attainable compromise. However, in a light-weight UAV, the cruciform tail weight is not significantly lower in comparison to a T-tail's, therefore it is not a selected option.

Figure 2.6d displays a set of two surfaces in a V-shaped configuration. The mobility of the hinged rear sections, known as "ruddervators", combine the functions of standard elevator and rudder, simplifying the setup of control actuators. To filter the additional control-actuation complexity, the rudder and elevator control inputs are blended in a mechanical "mixer", that allows aircraft control responses to be detected as they would in a conventional tail aircraft. A minor disadvantage of V-tail control has to do with adverse roll-yaw coupling. It can be observed when, for instance, a downward deflection of the left ruddervator and an upward deflection of the right ruddervator pushes the tail to the right, and thereby the nose to the left. This maneuver produces a roll moment toward the right, which opposes the turn but normally goes unnoticed to the pilot, as the arm of the force is very small.

An inverted V-tail, shown in Figure 2.6e, is a choice that would prevent the adverse yaw-roll coupling. In this set, the elevator deflections produce complementary roll moment, which enhances a coordinated turn maneuver. Inverted V-shapes can also be employed solely to avoid the wake of the main wing. That is the case in the inverted Y-tail, represented in Figure 2.6f, which has a third surface mounted vertically above, containing the rudder, whereas the remaining surfaces provide only pitch stability. In spite of their merits, both inverted V-tail and Y-tail present an eliminatory structural drawback that is the necessity of extra ground clearance at landing, that is hardly obtained without an attached landing gear.

Tail configurations that have two mounted rudders, like the H-tail or the twin tail, were not considered for one fuselage designs because they would require an heavier horizontal tail with extra resistance to bending and torsion. Tail sets having two rudders can be built with more structural ease through boom-mounted variations, approached in Sections 2.3.4.3 and 2.3.4.4.

2.3.4.2 Propulsion Arrangements

Wing mounting of engines, as in Figure 2.5, can provide extra wing bending relief and reduce fuselage drag, by having the propeller wakes generated from the wing outboard sections. On the other hand, engine-out control problems may also appear, forcing an increase in the size of the empennage. In fact, the performance of an airplane transporting a maximum payload of 10 N does not justify the installation of more than one electric engine.

(a) Upfront tractor location.   (b) Fuselage mounted pusher.

Figure 2.7: Sketches of possible engine sets.

The conventional tractor location, in Figure 2.7a, puts the engine up front in the fuselage, with the propeller in undisturbed air. It shortens the fuselage nose but favors overall stability and control. Figure 2.7b presents a fuselage-mounted pusher, that limits the propeller's diameter. Nonetheless, the inflow on that location allows a much steeper fuselage closure angle without flow separation than otherwise possible. An even more aerodynamically clean alternative with minimum propwash interference is a rear pusher propeller, like the one sketched in Figure 2.13e.

2.3.4.3 Twin Boom Conception

A twin-boom aircraft is characterized by two longitudinal booms fixed to the main wing symmetrically on either side. Tail-booms add more weight than a conventional fuselage construction, but can be desirable to achieve a prescribed stiffness on tail attachments. In a conventional variation, boom-mounted tails may have a low-mounted, mid-mounted or high-mounted horizontal tail. Having two mounting fins increases the elevator's efficiency, although the tail's wetted area ends up enlarged. Furthermore, twin booms allow unconventional empenage types to be installed without any ground clearance penalty. The tail assembly in Figure 2.8 is an example that is adaptable to a twin boom concept.

2.3.4.4 Twin Fuselage

A twin-fuselage aircraft may employ the same aft tail sets of a twin-boom concept, but instead of having one main body with two subsidiary boom structures, it carries its payload within two fuselages. Since wings experience maximum bending moments at points of contact with the fuselage(s), the structural benefits of span distributed loading with two fuselages are mainly felt on the central part of the wing, that will withstand a reduced load per unit span.
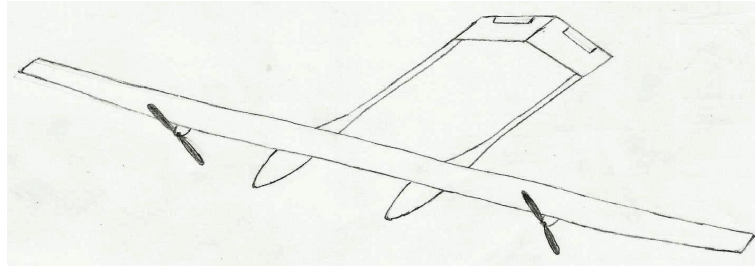
Figure 2.8: Design sketch of a twin-fuselage UAV.

Nonetheless, two narrow bodies cause more parasite drag than a wide body with the same payload volume. That fact wrote off the twin-fuselage as a conceptual option.

2.3.4.5 Canard Category

Canard airplanes incorporate a tailplane, also known as canard, ahead of the main lifting surface. Knowing that downwash can reduce the effective angle of attack of the wing, it is possible to design a canard to stall at an angle of attack lower than the wing's, offsetting the moment produced in level flight.

Assuredly, the canard is an inherently unstable configuration. For low subsonic speed applications, its main wing does not usually have flaps, because their deployment would cause an excessive nose-down pitching moment. Moreover, the canard flap is much closer to the center of gravity than an aft tail elevator would be. Therefore, to cope with the consequent reduction of trim and control effectiveness, bigger hinged surfaces are required, which leads to more trim drag when operating at fairly large deflections.
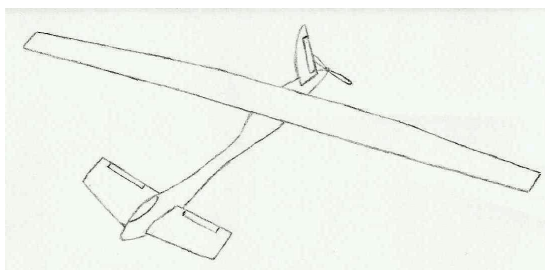
(a) Conventional pusher.
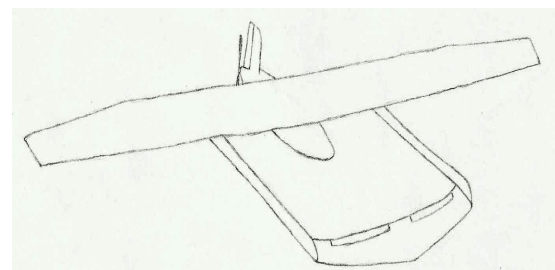
(b) Twin-boom pusher.

Figure 2.9: Sketches of canard configurations.

The canard sketches in Figure 2.9 have a rudder on the rear, for lateral control, and a pusher arrangement because placing the motor ahead of the foreplane would render the canard ineffective. Twin booms can also be used to narrowly attach the junctions of a foreplane, as illustrated in Figure 2.9b. Such solution may ease the installation of larger canards.

Ultimately, the unique canard design results on an highly maneuverable plane that only remains controllable by not achieving its full potential in terms of lifting capabilities. Given that the LEEUAV mission requires a long endurance flight with few maneuvers, the canard concept was not preferred.

2.3.4.6 Tailless Concept

The flying wing concept has been inspired by the idealization of an aeronautical vehicle in which all components not involved in the generation of lift are removed. Following that design philosophy, the wing becomes the only airframe component in an ideal airplane. Figure 2.10a presents a flying wing layout, entirely streamlined to minimize drag while maintaining a high lift-to-drag ratio. It is perceptible, though, that the volume provided by an extruded slender airfoil may be limited for all on-board cargo.

| (a) Flying Wing | (b) Blended wing body |
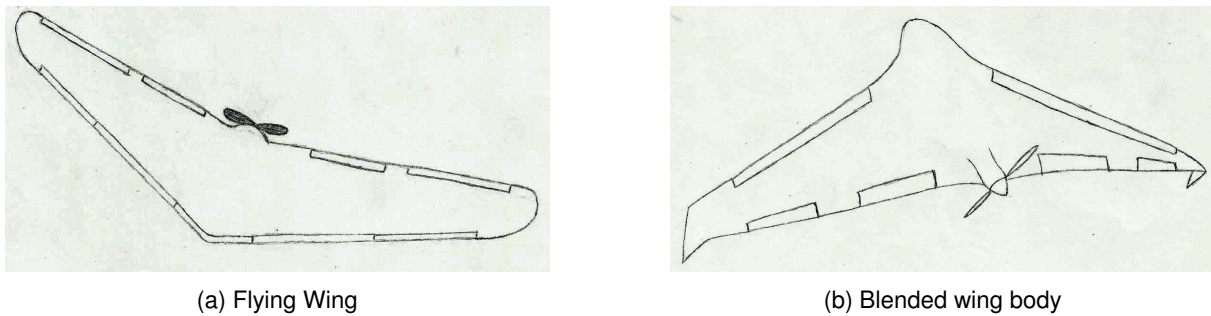
Figure 2.10: Sketches of tailless configurations.

The lack of payload volume can be attenuated resorting to a blended wing body configuration, illustrated in Figure 2.10b. It is a concept where a distinct fuselage is molded into a lifting body in the form of a low aspect ratio airfoil blended into high aspect ratio outboard wings. It provides more room upfront for cargo, while maintaining high aerodynamic efficiency.

Evidently, the most prominent challenge brought by a tailless design has to do with flight stability and control. To place outboard control surfaces behind the center of gravity, wing sweepback must be applied. The control lever arm will still be shorter than that of the conventional tail, hence, larger hinged areas are required.

Although it has been proven that, with suitable wing airfoil spanwise arrangement, this type of aircraft can be dynamically stable [62], the absence of constant chord surfaces will obstruct the installation of solar arrays, that have limited flexibility. In addition, the presence of solar cells would disable the possibility of adding wash-out twist on the wing to push the center of pressure forward.

Overall, stability and control complexity allied to a arduous integration of flight systems, make tailless aircraft, such as the flying wing and the blended wing body, hardly attainable designs for the LEEUAV.

2.3.4.7 Closed Wing Systems

An example of a non planar wing configuration, the biplane, has already been discarded due possible inefficient solar exposition of the wings, however, there are others that do not pose the same problem, such is the case of closed wing configurations. Two hypothesis have been analyzed, the box wing and the joined wing, whose sketches are in Figure 2.11.

The box wing configuration is characterized by a closed lifting system with a front wing and a rear wing of equal span connected by vertical fins. As for the joined wing design, it contains two wings joined together at the tips, arranged to form diamond shapes in both planform and front view.

According to [63], these configurations are able to distribute lift forces horizontally and vertically and gather conditions to be optimally twisted for minimum induced drag with high span efficiency.

(a) Box wing configuration   (b) Joined wing configuration
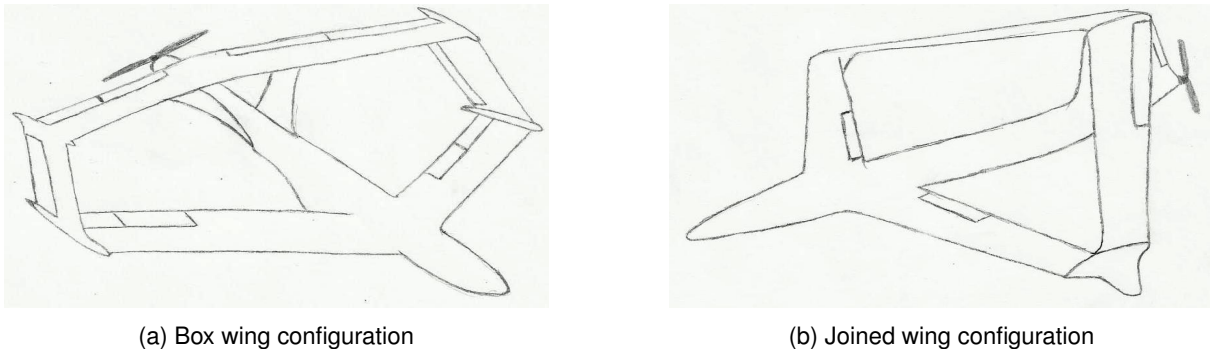
Figure 2.11: Sketches of closed wing UAVs.

For the LEEUAV project a highly span-constrained wing with low chord is disadvantageous because it limits the wing area available for solar arrays. Even if it was possible to retrieve some aerodynamic gain and still allocate enough solar cells, there would still be an extremely high level of structural complexity and many potential aeroelastic intricacies due to the presence of multiple lifting surfaces.

It is also clear that this sort of configuration poses additional manufacturing and maintenance costs. So, for all the reasons pointed out, closed wing systems are not a part of the design selection process.

2.3.4.8 Take-Off Devices

In low weight UAVs, cargo commodity during take-off and landing does not pose the same importance as in manned aircraft, thereupon, having an attached landing gear becomes an unnecessary feature.

Hand launching is the simplest take-off method that can be performed on small UAVs with a single fuselage. An example of a successful hand launched UAV is the solar powered Atlantiksolar mentioned in Chapter 1 (Figure 1.5b). However, it should be noted that hand launching can bring take-off speeds dangerously close to stall values, as reported during the first LEEUAV prototype development [58].

(a) Take-off launch trolley [58]   (b) Pneumatic catapult [64]
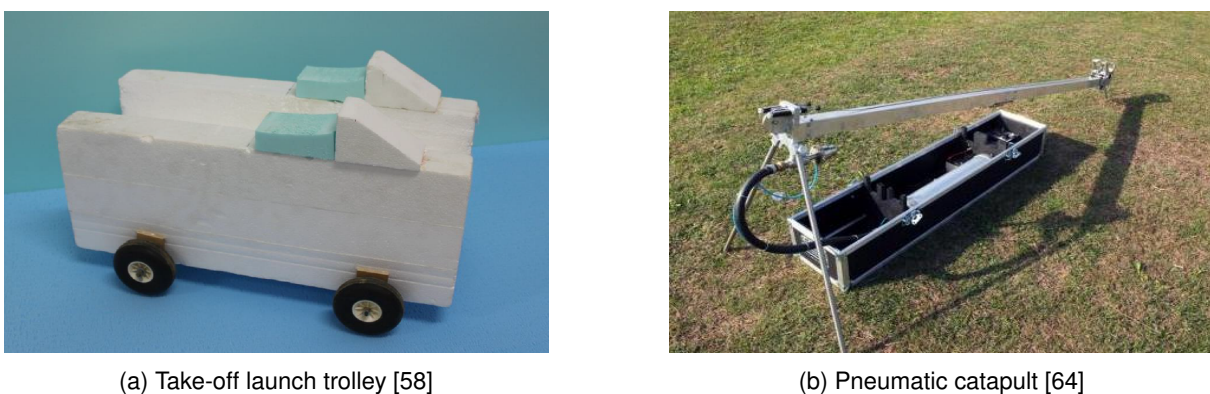
Figure 2.12: Possible take-off devices for the LEEUAV.

Take-off can also be achieved with a detachable launch trolley, such as the exemplar in Figure 2.12a, built in [58]. The launch trolley adds ground roll drag and inevitably decelerates after detachment. Due to

the transitioning difference in acceleration between flying and ground platforms, the trolley can get hit by the empennage. Under this circumstance, the airframe damage will depend on the tail's configuration.

Pneumatic technology offers the advantage of taking off anywhere with any sort of fixed-wing UAV. The UAV catapult in Figure 2.12b has a 2 meter launching run that can be disassembled and stored in a portable case. It operates with UAV take-off weight up to 10 kg and a maximum launching speed of 10 m/s. The only determinant drawback of this sort of device is the cost associated.

The pros and cons of every attainable take-off procedure are essentially related to the UAV's characteristics. Thus, the best take-off method can only be defined in agreement with other design variables.

2.4 Conceptual Design Selection

2.4.1 Prospective Aircraft Configurations

A total of 8 prospective aircraft configurations, illustrated in Figure 2.13, have been selected according to the arguments presented throughout Section 2.3.

Most of the approved airframe alternatives were chosen with the purpose of evaluating conjugated effects of features that did not present clear reasons to be excluded beforehand. The quadcopter is an exception that was hand-picked to demonstrate how the Analytic Hierarchy Process, detailed in the following section, precludes an evident poor solution.

2.4.2 Analytic Hierarchy Process Based Decision

The selection of the aircraft configuration was carried out using an Analytic Hierarchy Process (AHP). In this decision making methodology, introduced and developed by Saaty [65], a set of chosen criteria and alternatives undergo several pairwise comparisons in order to achieve an overall goal that, for this thesis, is to choose the most suitable UAV configuration to fulfill the mission requirements.

The range equation for battery powered electric aircraft can be used to recognize important selection criteria, it is deduced from [66] as

$$R = E^* . \eta_{total} . \frac{1}{g} . \frac{L}{D} . \frac{m_{battery}}{m} \, , \tag{2.1}$$

where E^* is the mass specific energy content [Wh/kg] of the battery system and η_{total} the systems total efficiency. It is clear that the range of the aircraft depends on the available energy, the propulsion system, the overall mass and aerodynamic properties of the aircraft. Hence, the chosen evaluation criteria that contribute for the mission goal include:

Aerodynamics) Assuming constant weight and energy efficiency, aircraft with higher C_L/C_D also present higher endurance. Flow separation and slipstream effects are also discerning factors.

Structures and Weight) Structural solutions that provide enough stiffness and can resort to low weight materials are given more importance.
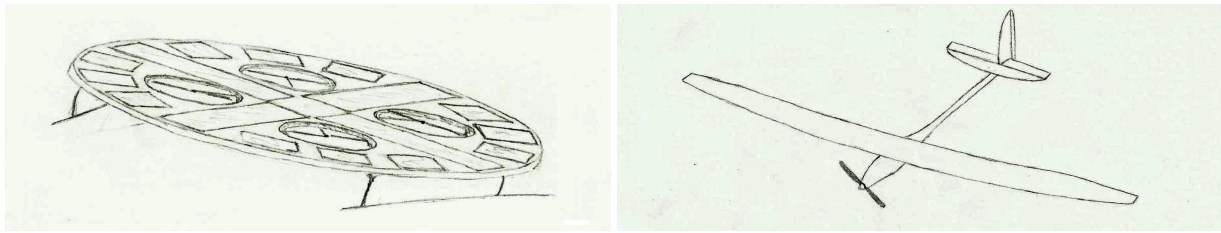
a: Quadcopter

b: Conventional tractor
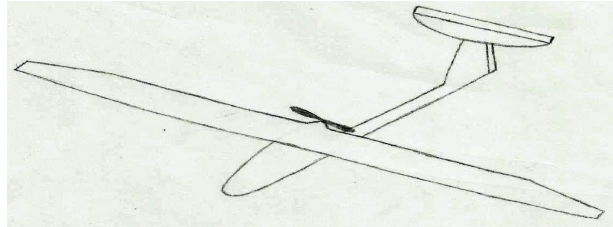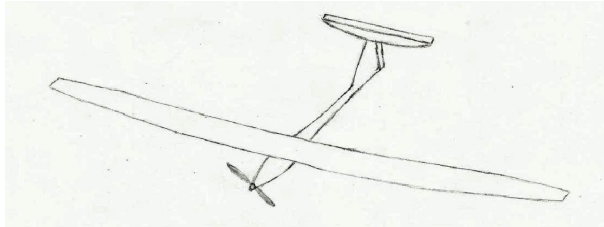
c: Tractor with T-tail

d: Fuselage mounted pusher with T-tail
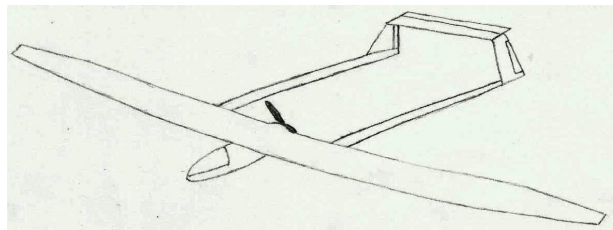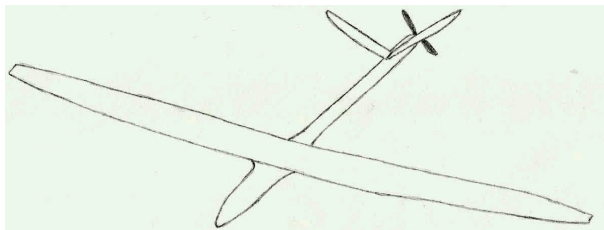
e: Rear pusher with V-tail

f: Double boom pusher
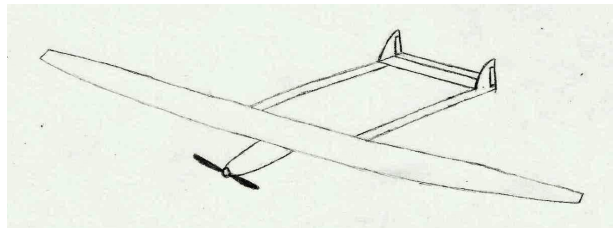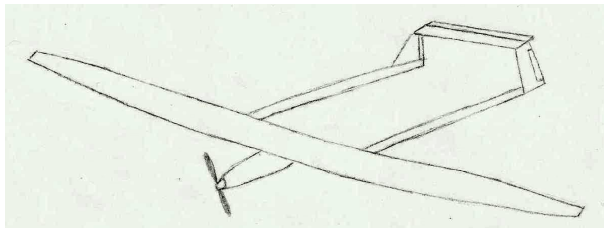
g: Double boom tractor with high mounted tail

h: Double boom tractor with low mounted tail

Figure 2.13: Selected airframe alternatives.

Solar Panels Integration) Having large surface areas available to install solar panels values a proper efficient design.

Propulsion) Propulsive efficiency is compared qualitatively. The space given to install large propellers is also taken into account.

Manufacturing and Maintenance) Low cost materials and less expensive manufacturing processes add focus to this criteria. Low cost non-regular maintenance also favors the aircraft.

Stability and Control) Given that the mission does not demand high maneuverability, inherent stability behaviour is preferred. Control surfaces mechanical complexity comes as a comparable factor.

Payload Volume) Being able to transport payloads with large volume adds value, however retaining the same payload within a lesser volume also distinguishes alternatives.

RPV Integration) Remote-person view is essential for surveillance. Having a proper installation site that allows equipment to obtain unobstructed field recognition footage is highly advisable .

Take-off and Landing) The range of feasible take-off methods for a given configuration is considered. Landing reliability is also evaluated.

Portable Capabilities) Disassembly characteristics that allow ground transportation with a small vehicle are a specific mission requirement that must be included in the AHP.

There are other prospect criteria that have been ruled out of the evaluating process, such as Electronics, for not diverging enough among configurations, and Aeroacoustics, since the mission neither takes place in urban or nature protected environments nor has additional stealth demands.

In the AHP method pairwise comparisons are made using a scale that consists of qualitative judgments ranging from equal to extreme with corresponding numerical values (1 = equal , 3 = moderate, 5 = strong, 7 = very strong, 9 = extreme importance). A pairwise comparison matrix for criteria was initially filled with the numerical judgments, respecting the reciprocal property ($a_{ij} = 1/a_{ji}$). Once that matrix was built, the priorities of the elements were estimated by finding the principal eigenvector of matrix A, $AQ = \gamma_{max}Q$, where γ_{max} is the maximum eigenvalue of matrix A. When vector Q is normalized, it becomes the priority vector. While building a pairwise comparison matrix, it is necessary to check consistency by calculating consistency ratio (CR) as the ratio of Consistency Index (CI) with Random Index (RI). As stated in [67], inconsistencies are tolerable and a reliable result may be expected if $CR < 0.1$. Consistency Index is calculated by $CI = (\gamma_{max} - d)/(d - 1)$, where d is the square matrix dimension. Random Index is a tabulated value, for $d = 10$, $RI = 1.49$ and for $d = 8$, $RI = 1.41$.

The global priority data matrix, with respect to criteria, is displayed in Table 2.1.

	A	B	C	D	E	F	G	H	I	J	Priority Vector
A	1	1	7	2	5	1/2	3	7	5	5	0.1934
B	1	1	5	2	5	1	3	7	5	5	0.1988
C	1/7	1/5	1	1/7	1/3	1/5	0.2	1/2	1/2	1/3	0.0220
D	1/2	1/2	7	1	5	1/2	1	5	3	5	0.1287
E	1/5	1/5	3	1/5	1	1/5	1/3	2	2	1	0.0439
F	2	1	5	2	5	1	2	5	5	5	0.2014
G	1/3	1/3	5	1	3	1/2	1	5	3	5	0.1098
H	1/7	1/7	2	1/5	1/2	1/5	1/5	1	1/2	1	0.0281
I	1/5	1/5	2	1/3	1/2	1/5	1/3	2	1	1	0.0378
J	1/5	1/5	3	1/5	1	1/5	1/5	1	1	1	0.0362
$\gamma_{max} = 10.4433$			$CI = 0.0493$			$CR = 0.0331$					
A - Aerodynamics B - Structures and Weight C - Manufacturing and Maintenance											
D - Propulsion E - Stability and Control F - Solar Panels Integration G - RPV integration											
H - Payload Volume I - Take-off and landing J - Portable Capabilities											

Table 2.1: Pairwise comparison matrix of evaluation criteria.

The global priority pie chart division (Figure 2.14) reveals three major criteria, Aerodynamics, Structures and Weight and Solar Panels Integration. Observing Equation (2.1), the term L/D is directly related to aerodynamics and the ratio $\frac{m_{battery}}{m}$ to weight. Seeing that these terms affect the range equation in the same proportion, Aerodynamics and Structures and Weight have been given equivalent
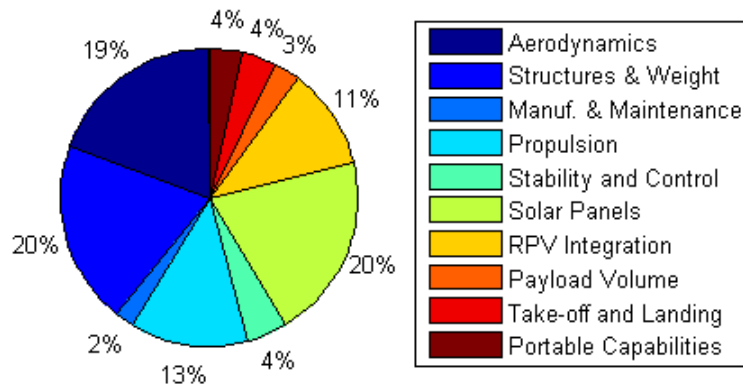
Figure 2.14: Global priority vector results

importance when compared with each other. Solar panels also show up in Equation (2.1) underneath the energy term E^* and, with less relevance, in the mass term.

Propulsion's percentage reflects its efficiency impact as this system presents by far the biggest slice of energy consumption. RPV integration also comes with a fair portion of importance since it fulfills the mission by retrieving surveillance data to the operator. The remaining criteria are residual, not rendering significant distinction among configurations. The least important factor, with 2% of influence, includes maintenance, which tends to be economic and swift for a low weight UAV, as well as the manufacturing parcel, since the airframe only represents a small portion of the total cost of the aircraft when accounting with propulsion and communication systems. After consulting the collaborative project financial data [68], it is discernible that the propulsive system is going to be the most expensive one, followed shortly by the communications system.

The same eigenvalue computing process was used to determine the comparison matrices of the candidate configurations with respect to the criteria and their local priorities. All ten pairwise comparison matrices of alternatives have been summarized in Tables B.1 - B.10 placed in Appendix B. The consistency ratio remained acceptable ($CR < 0.1$) in all pairwise comparisons, which is an indicator that the solution is not invalid. The final priority vector was obtained by multiplying the matrix of local priorities with the global priority vector, providing the raking of alternatives, illustrated in Figure 2.15, with data retrieved from annexed Table B.11.

2.4.3 Discussion of Results

In therms of aerodynamics, the rear pusher with V-tail (alternative 2.13e) is the most clean configuration, with no propwash flow interference, ranking above all others. On the extreme opposite is the quadcopter (2.13a) that has a null lift-over-drag ratio, suffering the most aerodynamic depreciating score. The fuselage mounted pusher (2.13d) presents a clean nose but makes it very difficult for the emmpenage to avoid propwash, on the contrary the T-tail tractor (2.13c) suffers propwash interference upstream on the fuselage but prevents wake interference on the horizontal tail. Comparing these two cases, the flow around stabilizing and control surfaces was considered more relevant than the aerodynamic interference generated on the nose. Therefore the fuselage mounted pusher scored slightly lower than the T-tail trac-
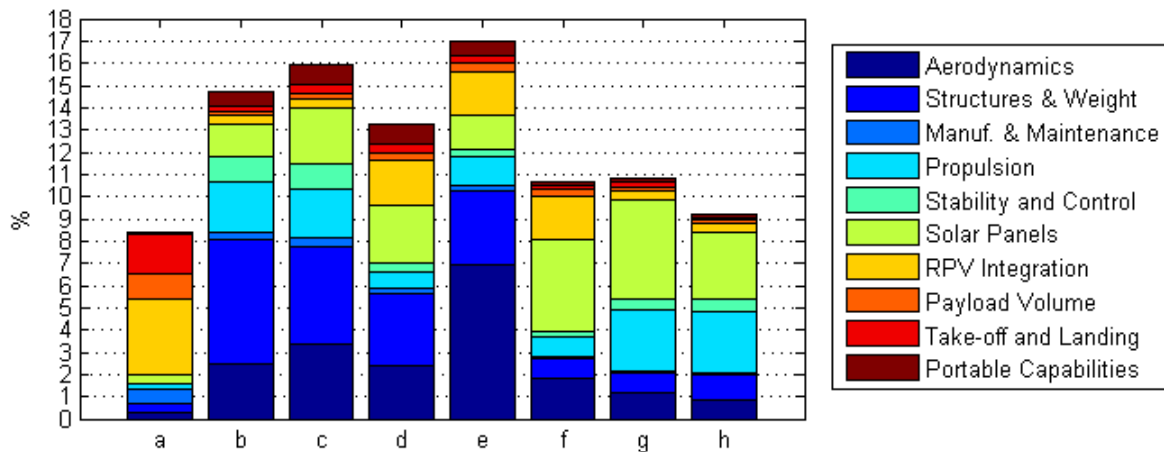
Figure 2.15: AHP final results (the bar numbering matches the configurations in Figure 2.13).

tor and broke even with the conventional tractor (2.13b), that has lower aerodynamic priority than the respective T-tail because of its wing's wake interference on the tail. The double-boom configurations suffered aerodynamic penalties, due to enlarged surface areas, and were distinguished among each other by the tail's positioning and the nose's obstruction.

Regarding Structures and Weight, the excelling option is the conventional tractor, because it possesses an inverted T-tail empennage, whose parts can be easily supported by a single tail boom. On the other hand, the quadcopter, in spite of having a simpler airframe design, cannot rely on its surface area to produce lift, therefore its inertia is penalizing. Looking at the pusher configuration, its V-tail is not necessarily heavier than a T-tail, but the engine positioning is considered disadvantageous because it requires a stiffer rear fuselage assembly, capable of withstanding higher torsion and bending moments. Due to structural simplicity, single fuselage options win relevance over heavier double boom variations.

Solar Panels installation is greatly penalized in the quadcopter because, for the same payload weight, the amount of solar cells it needs to power flight is exceedingly higher when compared with an airplane. It is assumed that all sketched airplanes have power requirements not too far from each other, so the ones with more useful surface area are given more importance. Double boom high-mounted tail configurations benefit the most with their large horizontal stabilizer area, next comes the double-boom low mounted tail, that is closer to T-tail alternatives due to the shadow its vertical stabilizers may cause. The least rated airplanes were the conventional tractor and the V-tail pusher, since their empennages do not favor the incorporation of solar cells.

Concerning Propulsion, the quadcopter is by far the most inefficient option, as each one of its 4 engines must provide simultaneously lift and thrust forces. Tractor configurations were given better evaluation than pushers, that are considered less efficient for operating in disturbed flow, in the wake of aerodynamic surfaces. Moreover, the pusher T-tail airframe limits the propeller diameter, which is why it is the most penalized alternative. The V-tail rear pusher was less penalized than the remaining pushers because it is located farther away from the flow disturbance of the main wing's wake.

Tractor alternatives present a clear obstacle to Remote-Person View Integration as the motor occupies a viewpoint from where a camera could record the whole horizon ahead of the aircraft. In addition to

that, the tractor's propeller may obstruct footage. Conversely, RPV capabilities are enhanced by quad-copters, that ultimately may provide 360 degree panoramic footage, which is not essential when the target of surveillance is on the ground. For that motive, the quadcopter's RPV Integration surpasses moderately clean nose configurations, that also provide an upfront location to the camera.

When it comes to Stability and Control, the quadcopter is evaluated as the worst option because it does not possess inherent static stability and is entirely dependent of flight control software to be piloted. Pushers are the most penalized among airplanes, since placing the engine behind the wing hampers the needed weight calibration. The lowest fixed wing score is the double boom pusher's because of the mechanical setup complexity of the mounted tail control surfaces. Among tractor configurations, double boom options lose to single fuselage designs, due to the number of control surfaces, and horizontal tails placed lower win over those placed higher because of the extra moment given by the distance to the fuselage's centerline. Adding up these arguments, the conventional tractor is the most stable concept.

Take-off and Landing adaptability is a major score bonus for the quadcopter, since it can perform both almost anywhere, without any extra devices or runway. The slight score variations between airplanes have to do with applicable devices to help take-off and the tail's ground clearance at landing. The double boom group has been given less importance because of the complex shape of a prospective launch trolley for such configurations. The double boom pusher (2.13f) is penalized in particular because its propeller location may endanger hand-launching.

In terms of Portable Capabilities, a considerable large area filled with solar panels makes the quad-copter much more difficult, if not impossible, to disassemble into smaller parts promptly enough only to ease transportation, so the rotary wing alternative has got the last portability rank. The extra amount of time and effort it takes to detach the parts of double boom UAVs places their portable capabilities below single fuselage airframes. High mounted tails can be dismantled with more straightforward procedures than a conventional tail or a V-tail, which concedes T-tail configurations the best portable capabilities.

Payload transportation volume favors the quadcopter, that can arrange it vertically, beneath the main structure, covering the widest set of possible dimensions for a cargo up to 10 N. With respect to airplane's available volume, pushers have moderate importance over tractors because of the extra room left upfront the fuselage. Furthermore, the double boom group receives a slight payload volume score discount since two separate booms increase the UAV's average width while providing less gathered room than the rear portion of a single fuselage.

The highest score for Manufacturing and Maintenance went to the quadcopter's simpler airframe, that does not pose the same manufacturing challenges as an airplane UAV. Among fixed-wing alterna-tives, double-boom UAVs have less relevance to Manufacturing and Maintenance since they have more parts to assemble, that require more effort to construct and provide preventive technical support. In sin-gle fuselage designs, tractors are preferred to pushers because of the additional difficulty of harboring motors in the vicinity of wings or stabilizing surfaces. It is also known that the favorable demountable characteristics of the T-tail also ease maintenance, for that reason the T-tail tractor is considered the best airplane choice for Manufacturing and Maintenance.

Ultimately, after adding up all the justified scores given with respect to criteria, the overall winner of the AHP was the rear pusher with V-tail (Figure 2.13e) that got a preference of 17%, surpassing the second classified, T-tail tractor, by a slight margin of 1%. The decisive factor was aerodynamics, that was the only criteria where the rear pusher excelled over the remaining alternatives. Unsurprisingly, the quadcopter was ranked last, however, its 9.24% of importance ended up unexpectedly close to the double boom group, mainly due to the importance of the remote-person-view system.

Chapter 3

Aircraft Initial Sizing

With the concept decided, the next step of the project consists in scaling out the airframe. This chapter describes all the processes involved in the first estimation of the LEEUAV's dimensions and weight. Through market research and historical data review, an empirical model has been obtained for the airframe's empty weight as function of the wing dimensions. Regarding stipulated components masses, an overview of all required on-board systems allowed to understand the cargo that must be accounted for each piece of equipment, as well as their functions and operating modes during flight.

3.1   First Generation Prototype

The previous design, implemented for the first generation's manufacture in UBI, was not only an addition to the research historic but also served as basis to initially estimate inputs for the weight prediction model [58]. It is a conventional configuration, exclusively radio controlled, whose differences from the updated concept are the inverted T-tail assembly and engine tractor positioning.
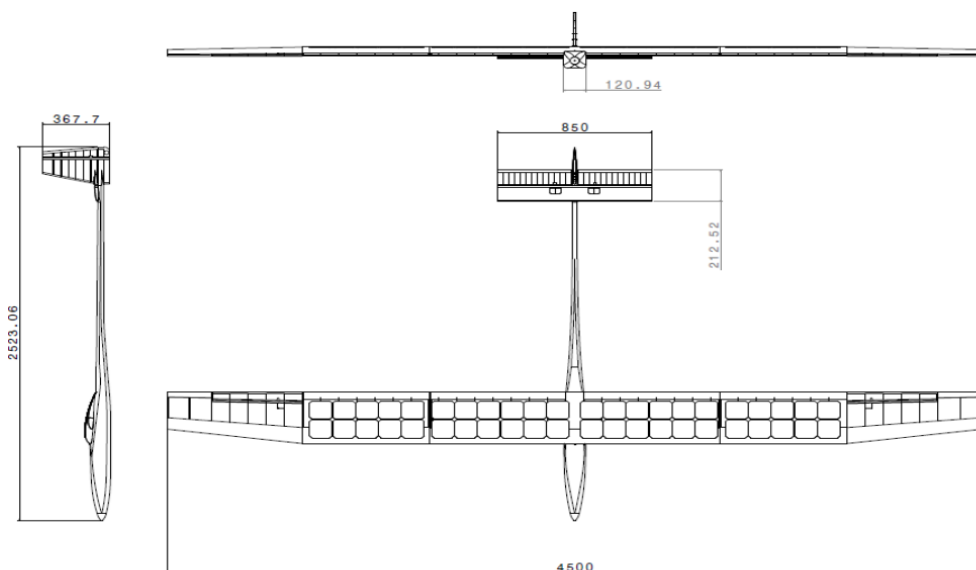
Figure 3.1: Three view drawing of first generation LEEUAV [58].

Its wing breaks up in three parts, to ease ground transportation, and each part holds a C shape spar with a torsion box, to increase tolerance to maintenance damages. The airfoil, developed using an in-house gradient based aerodynamic shape optimization tool, was also revised in order to prevent structural damages, namely in the trailing edge. Attending to the results of a parametric study, a two row array of solar panels was considered the most efficient solution, which, given the airfoil's camber, corresponded to an admissible mean chord of 33 cm.

The fuselage can be divided in three parts as well, which are the main container body, a tail boom and an empennage support rearwards. Storage room is diminished by making the horizontal tail detachable, while the vertical one and the empennage support are bonded as a single piece. The construction materials applied are shown in Table 3.1.

Component	Material	Application
Wing	Balsa wood	Ribs, trailing edge, ailerons
	Extruded polystyrene foam	Torsion box core
	Plywood	Outboard section ribs
		Central ribs connecting to fuselage
	Carbon fiber laminate with epoxy resin	Torsion box shell
	Unidirectional carbon fiber	Boom
		Outboard ribs reinforcement
	Heat shrink covering Film	Skin
Fuselage	Carbon fiber laminate with epoxy resin	All parts
Empennage	Balsa wood	Skin, ribs and booms
	Heat shrink covering Film	Skin
	Unidirectional carbon fiber	Booms

Table 3.1: Materials used in airframe components of the first generation LEEUAV.

Although the installation of solar arrays over the wing was not included on the manufacturing process, parametric computations concerning the energy generation system indicated the set of electric propulsion components in Table 3.2 as the most efficient alternative found for the mission [54].

Motor	Motor characteristics [69]				Propeller	Battery
	Kv [RPM/V]	I_{max} [A]	P_{max} [W]	m [kg]		
Hyperion ZS 3025-10	775	65	1150	0.1976	13x8	LiPo 3S 11.1 V

Table 3.2: First generation propulsive system characteristics.

3.2 Mass Prediction Model

At the early sizing stage of the work, the maximum take-off weight prediction can be divided into fractions that must fall under one of three categories:

Fixed masses) Include prescribed payload and communications systems defined by Figueiredo [57] and Miller [56]. Do not depend on the sizing of other parts, there is no uncertainty associated.
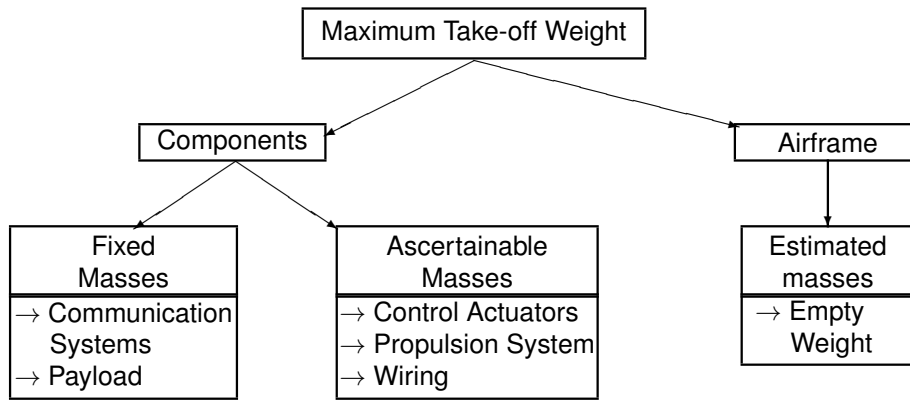
Figure 3.2: Schematic of the LEEUAV mass categories in early sizing stages.

Ascertainable masses) Composed by components whose choice is influenced by the aircraft's dimensions, such as the ones on the propulsion system, remarked in Subsection 3.2.3. Ascertainable masses first calculation is also based on previous designs, but it undergoes an iterative process throughout all studies included on the preliminary design (Chapters 4 and 5). The uncertainty of the converged solution is negligible since the components are sized to enable the propulsion system to handle the most pessimistic scenario and their exact weight is prescribed.

Estimated masses) Airframe weight is estimated with analytic relations obtained empirically, having the highest degree of uncertainty associated it relies on the descriptive quality of the mathematical model. This uncertainty is only mitigated as the airframe detailed analysis progresses, notwithstanding, it is always present until the construction stage. Subsection 3.2.4 will describe in detail how the empty weight estimation model was obtained for this work.

3.2.1 Communication Systems

The communications systems, labeled as fixed masses in Section 3.2, have already been settled, thus their avionic components are only briefly introduced. In order to perform long endurance flights, the radio control sub-system must possess two mandatory add-ons, a Long Range System (LRS) and a flight controller or autopilot.
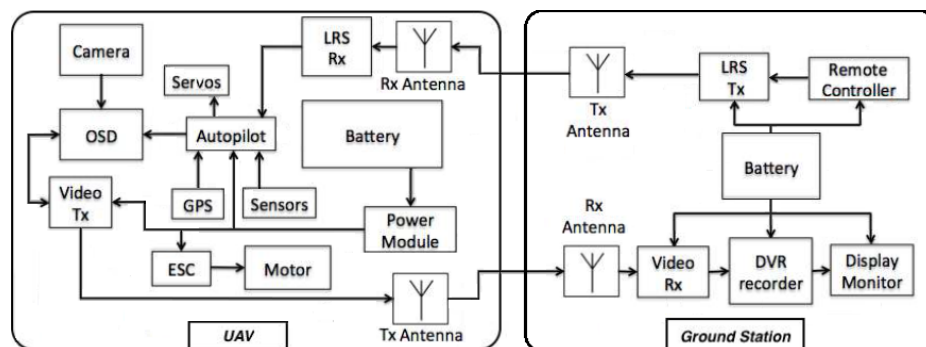
Figure 3.3: UAS functional equipment structure.

The autopilot system autonomously guides the UAV to follow reference paths or navigate through

pre-set waypoints, so it has to be linked to all on-board systems, as shown in Figure 3.3. Ardupilot APM2.6 was the chosen flight controller (Figure 3.4).

Achieving longer flight distances became possible with the LRS. This device, that consists of a small box transmitter mounted on the back of the existing RC transmitter, greatly increases the distance over which a radio signal reaches the airborne receiver. The Thomas Scherrer, whose receiver is in Figure 3.5, is the selected long range RC system.

Figure 3.4: Autopilot Ardupilot APM 2.6 [70].

Figure 3.5: Long range radio receiver Thomas Scherrer Rx700. [71].
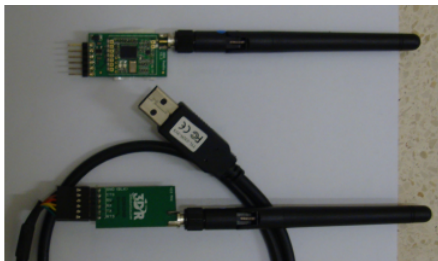
Figure 3.6: 3DR radios [57].
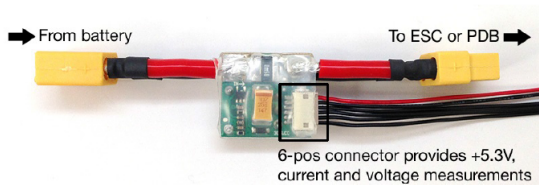
Figure 3.7: Power module from 3DR [72].

Air-to-ground data link between the autopilot and the ground station is provided by a telemetry 3DR radio, shown in Figure 3.6, which is a supplement to the autopilot. The operator can access real time data from the UAV such as the battery voltage level, which is also supervised thanks to a Power Module (Figure 3.7) that supplies power the autopilot board.

The GPS Module in Figure 3.8 provides GPS and Compass data. The GPS information combined with sensor readings are passed to a filter that estimates the current states for later control uses.

Two sorts of sensor are linked to the autopilot, an airspeed sensor and a sonar.

Figure 3.8: GPS Module [73].
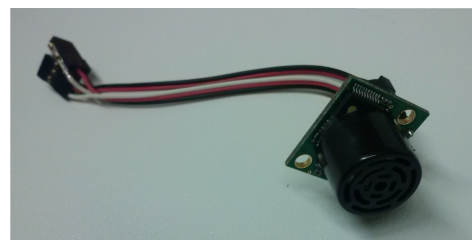
Figure 3.9: Sonar sensor.

The sonar sensor (Figure 3.9) may confer an obstacle avoidance functionality to the Ardupilot by measuring the distance between the sensor and an obstacle in front of it, however, in the present proto-type it is only used as a support system for landing.

Windy conditions, slow flight and autonomous landing are handled with the airspeed sensor, whose components are shown in Figure 3.10. It has a pressure sensor that is connected to a pressure measurement unit. This unit has a pitot tube and a static pressure port. The pitot tube measures the total pressure of the air flow, and the static pressure port measures the static pressure on the air. The top tube that exits the unit is connected to the bottom port of the pressure sensor using a silicon tube.

(a) Pressure sensor [74].

(b) Pressure measurement unit [57].

Figure 3.10: Airspeed sensor's components.

Remote-Person View (RPV) is the method used to radio-control the UAV from the cabin's point of view. The video system installed includes primary components such as the camera, video transmitter and receiver, On-Screen Display, also ground display and recorder and high gain antennas. This enables the LEEUAV to fly beyond visual range, limited only by the range of the equipment used.

The selected camera was the Kx-181 CCD Sony, in Figure 3.11, because it has the recommendable imaging device, its voltage range is within the 2S/3S batteries and it is fairly priced.

Flight information, like the UAV's altitude, heading, direction to home, distance from home, velocity or power, can be overlaid onto the video stream provided that the telemetry module of the autopilot is connected to an On-Screen Display (OSD) device. MinimOSD, in Figure 3.12, was the chosen OSD circuit board.

Figure 3.11: Video Camera Kx-181 CCD Sony.
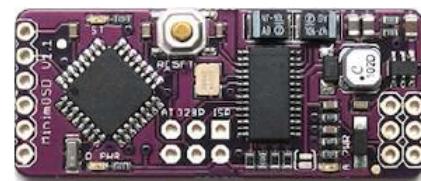
Figure 3.12: On-Screen Display MinimOSD from 3DR Robotics [75].

Unlike digital video systems, analog systems are within the project's budget range and admit long ranges if used with the appropriate antennas. With weight and consumption reduction also in the balance, the video transmitter (Figure 3.13a) and ground receiver developed by Partom were preferred.

Miller [56] verified in flight tests, up to a distance of 7 km, that the best overall image quality is obtained with a skew planar wheel antenna (Figure 3.13b) on-board and an helical antenna on the ground station. The video receiver, for having a higher gain ground antenna such as the helical, concentrates its focus into a more specific area and can interpret the signal much easier, which is ideal in long range

flights. In addition, the system works best if the helical antenna is coupled with the skew planar because they have the same polarization.
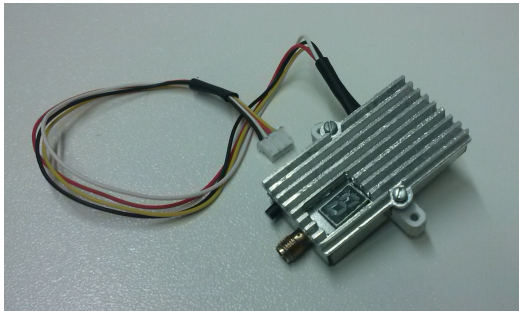
(a) Partom's video transmitter.

(b) Video Tx Skew planar wheel antenna [76].

Figure 3.13: On-board components responsible for video transmission.

Mass values of the communications systems airborne elements and payload have been fixed and are summarized in Table 3.19a. For further querying, the components of the ground station are specified in [56].

3.2.2 Control Actuators

Flight control surfaces are provided with motion due to mechanical actuators known as servos. Unlike the avionics mentioned so far, these essential elements of the RC system have not been considered fixed masses in the scheme of Figure 3.2 because their weight is related to the required torque ratings, which depend on control surfaces sizing and positioning. After the stability studies of Section 4.2 were performed, servos Corona DS-939MG were preliminarily confirmed for both ailerons and ruddervators. Their weight and dimensions can be found in Table 3.19a.

3.2.3 Propulsion System

The design of the propulsion system has determined a solution combining both lithium-polymer batteries and solar panels to provide energy to the electric motor, as schematically illustrated in Figure 3.14 [55]. During climb, the battery is the main source of energy, as the the aircraft can not reach the necessary power with solar energy alone. In cruise, when the solar panels provide more than enough electric energy to propel the aircraft, the energy excess can be utilized to recharge the battery, or to power auxiliary electronics, such as the video transmitter. In a situation of energy deficiency, power is drained from the battery, that is no longer recharged. Naturally, night flights are performed solely with a pure battery powered system.

For this project the acquired photovoltaic (PV) cells are the SunPower C60 (Figure 3.15a). These thin mono-crystalline silicon PV cells have an efficiency that can go up to 22.6% and its modules are semi-flexible (bending is possible in one axis), which allows mounting arrays on a wing's upper surface.

The Maximum Power Point Tracker (MPPT) is a solar charge controller that extracts the maximum electrical power from the arrays by adjusting more efficiently the electric current. Since it will be charging
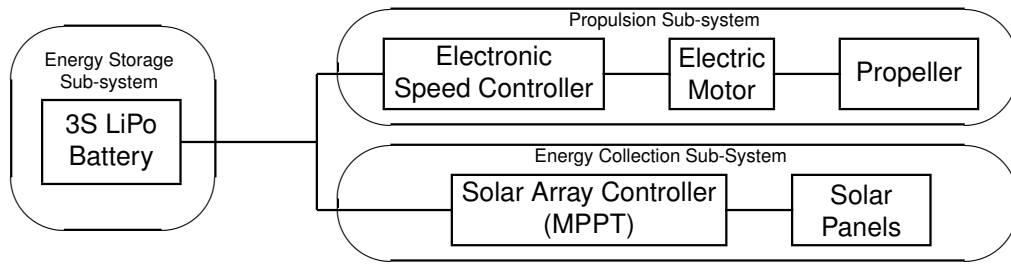
Figure 3.14: Architecture of the hybrid propulsion system.

a LiPo battery, it also needs to manage its charge without damaging the cells. Thereby, the MPPT chosen is the GV-10-Li-12.5V from Genasun (Figure 3.15b). While being compatible with 3S LiPo batteries, it has a maximum output of 140 W which surpasses the expected power output of the solar arrays.
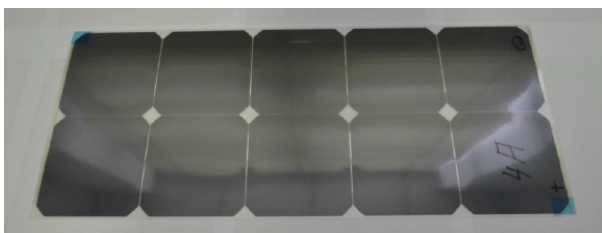
(a) SunPower C60 PV cells panel [55].
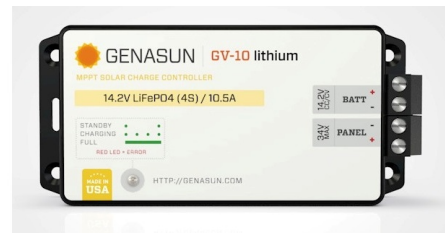
(b) Genasun's GV-10 Lithium MPPT [77].

Figure 3.15: Elements of the energy generation sub-system.

High energy density is indispensable for energy storage in this application and the available sort of battery that best suits such demand is the lithium polymer (LiPo) battery. Moreover, a three cells connection in series (3S), meaning a nominal voltage of 11.1 V, matches properly with all systems. Ultimately, the propulsion analysis performed in the preliminary project (Section 4.3.1) allowed to select two LiPo batteries, model Hyperion G3 VX 3S (Figure 3.16b), with 4200 mAh capacity each.

(a) Electric motor Hyperion ZS 3025-10 [78].

(b) Battery Hyperion G3 VX 3S [79].

(c) APC 15" x 8" Propeller [80].
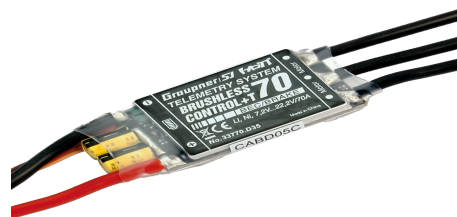
(d) ESC Groupner T70 [81].

Figure 3.16: Components of the propulsion system.

The electric motor and respective propeller were also selected in agreement with the performance analysis of climb and cruise, detailed in Section 4.3. Figure 3.16a shows an Hyperion ZS 3025-10, which is a motor directed to slow moving high trust propellers, as indicated in Table 3.2 by its relative low value of 775 rpm per V input. Unlike the motor, the propeller's choice was updated to a folding 15" x 8", illustrated in Figure 3.16c, in which the first designation number is the diameter and the second its pitch, both in inches. Its spring system retracts the two blades when they are not turning, which is advantageous for landing and gliding. Once powered again, they will open thanks to centrifugal forces. All propellers in this work have been made by Advanced Precision Composite (APC) manufacturer from injection molded material, whose light weight contributes to increase propulsive efficiency.

To interpret control information regarding the rotational speed of the motor an electronic speed controller (ESC) is needed. Knowing that it must be able to work with a current higher than the maximum current drawn by the motor, the Groupner T 70 in Figure 3.16d was chosen. This ESC has a voltage input limit of 25 V and a current input limit of 70 A.

At the end of this chapter, Table 3.19a stipulates the mass and dimensions of each component of the hybrid propulsion system that has been described in this section.

3.2.4 Empty Weight Estimation

Given the lack of solid bibliographic background concerning empirical correlations for empty airframe weight fractions of low wingspan UAVs, a market research for similar aircraft data was deemed necessary. The research focused mainly on model gliders (with electric propulsion or not), due to their high aspect ratio and absence of landing gear. Throughout manufacturers and retailers, the available technical information was often limited and even though the offer was extent, only around 40 models, listed in Table C.1 in Appendix C, have shown perceivable empty weight values and dimensions comparable to the LEEUAV in Figure 3.1. Within the arranged database, three major wing construction types were identified:

Foam Cored Construction) Foam cored wings variations include fully sheeted wings with obeechi veneer or balsa. This group may feature only heat shrink covering film or also vac-bagged carbon and glass partial coverings.

Molded Construction) Wing skins are completely molded under vacuum with composite materials and do not depend on internal structural components to possess the airfoil shape.

Rib Construction) The presence of rib components, attached or not to a spar, provides the desired airfoil shape. The skins are mostly composed by heat shrink film.

Among each construction type the aspect ratio does not vary expressively, but there is still a large variety of custom inset spars and other reinforcing details. The scatter chart in Figure 3.17 displays the appointed empty weight $m_{airframe}$ and wing area S of the researched aircraft. It is noticeable that models with rib conceived wings tend to be lighter for the same wing area. For that reason, the rib construction type should be selected for the wings manufacture, as it had been previously for the first

generation LEEUAV. Looking exclusively to the aircraft with rib constructed wings in Figure 3.17, it was possible to obtain a regression equation relating empty weight with wing area,

$$m_{airframe} = 512.99 \, e^{0.01 \, S}, \tag{3.1}$$

where $m_{airframe}$ is measured in grams and S in square decimeters (dm^2).
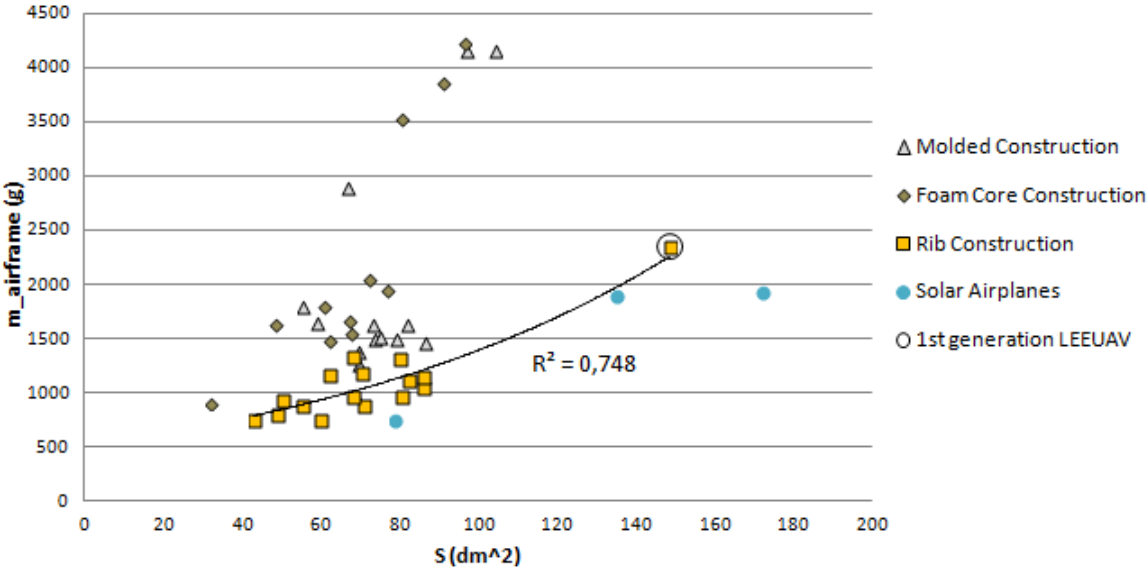
Figure 3.17: Empty weight as function of wing area obtained with model glider scattered data.

The correlation coefficient R^2 obtained in the exponencial regression presents a fair value of 0.748, however, it is only an indicator of how Equation (3.1) minimizes the distance between the fitted line and all of the data points. In the wing area range containing an higher density of points ($43dm^2 \leq S \leq 85.7dm^2$) the non-linear model follows the scattered data towards a mean increase of weight with wing area. All scattered data present slight deviations from the theoretical model, with no apparent biased nature, not only because there can be distinct types of rib constructed wings, but also due to the absence of additional airframe weight predictors, such as the fuselage and the empennage, whose characteristics are not constant among the researched aircraft. The remaining portion of the regression domain ($85.7dm^2 < S \leq 148.5dm^2$), in which the upper limit is represented by the first generation LEEUAV, includes no data besides its boundary values. In fact, with the exception of a few solar airplane prototypes, most existing UAVs with rib constructed wing do not reach such large wingspan. Such occurrence reduces even more the regression's confidence level in terms of precision.

Observing that the number of accounted airborne components has increased since the first prototype, it becomes clear that lift must increase and so does the wing area. Hence, the airframe weight is expected to surpass the range of regression. Although it was not possible to obtain a precise estimate, a conservative value, with high probability of surpassing the effective empty weight, could be determined. Since the the correlation in Equation (3.1) was conceived with an exponential growth nature, the more the wing area increases, the more likely it is that an overestimated airframe weight fraction will be achieved. The most recent estimate, registered in Table 3.19, assumes an airframe empty weight of

2731 g for a wing area of 167 dm^2.

The few solar planes pinpointed in Figure 3.17 also have rib constructed wings, but none was used as a regression point because their weight values were considered optimistic. For instance, the collected airframe with the largest wingspan is also the most recent (Atlantik solar in Figure 1.5b) and its degree of weight optimization was promptly recognized as unachievable with the manufacturing technology available. Another example is the SunSaylor, an older UAV project implemented at the Faculty of Aerospace Engineering in Haifa, Israel [82]. Having a wing area of 135 dm^2 and an empty weight 1900 g, the SunSaylor was not used to obtain Equation (3.1), though it is much closer to the theoretical model, because its inclusion would diminish the model's probability of overestimating the empty weight at higher wing area values. Given the accuracy of the current empty weight model, overestimation is preferable to underestimation since the later may cause the endurance to fall bellow the 8 hour requirement, while ending up with less weight then predicted will only allow the UAV to surpass the required endurance.

3.3 LEEUAV Provisory General Characteristics

As mentioned before, the first generation LEEUAV was a guideline to assign general dimensions beforehand. Observing Figure 3.18, the wingspan increased to 5 m, but the taper ratio was kept from the first prototype. Another similarity recovered is the wing tip portion without solar arrays, solely meant for aileron control. On the remaining wing surface, solar arrays fill as much area as possible.
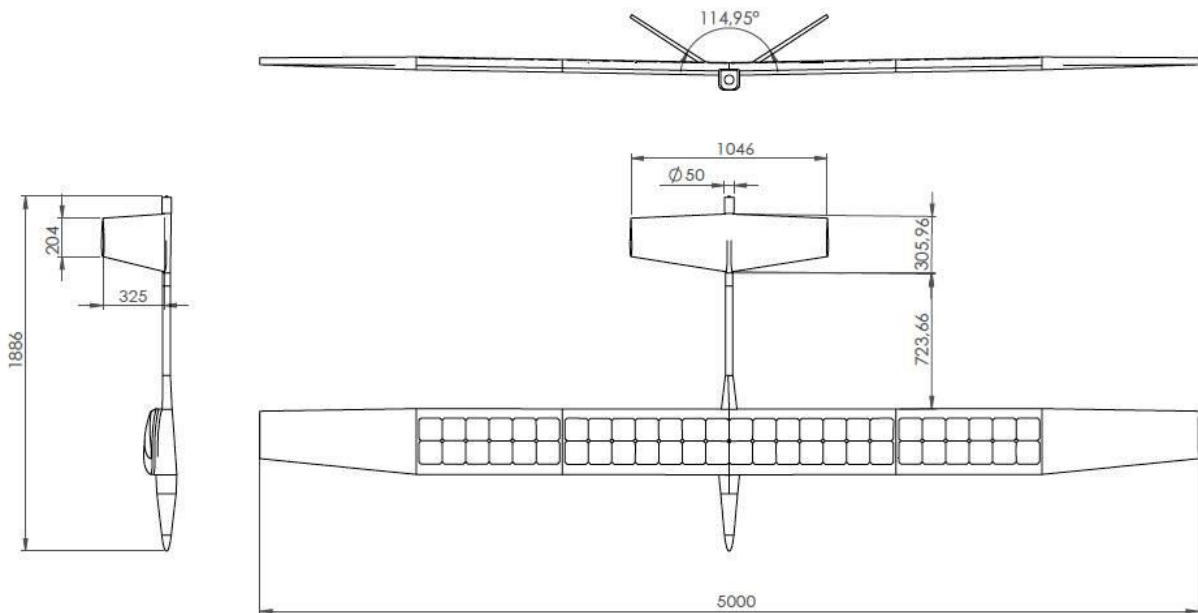
Figure 3.18: Three view drawing of the provisory LEEUAV (dimensions in mm).

The V-tail was initially sized as an equivalent conversion from the first generation's conventional tail. Its planform area S_{V-tail} and dihedral angle ν are calculated under the assumption that V-tail's aspect ratio equals that of its conventional counterpart's horizontal tail, that is $AR_{V-tail} = AR_H$. In the

following equations, taken from [83], S_H stands for the conventional horizontal area and S_V is the area of the vertical stabilizer.

$$S_{V-tail} = S_H + S_V \qquad (3.2) \qquad\qquad \nu = arctan\left(\sqrt{\frac{S_V}{S_H}}\right). \qquad (3.3)$$

The wingspan b and mean chord $\bar{c}$ are then calculated from known relations, $b = \sqrt{AR \cdot S}$ and $\bar{c} = S/b$, where AR is the wing aspect ratio.

Altogether, with the mass of all on-board components remarked throughout this chapter, and the airframe weight, computed by inserting the wing area of the provisionally sized LEEUAV in Equation (3.1), an estimate of the complete weight distribution was obtained in advance.

Airborne Elements	Dimensions (mm)	Absolute Weight (g)	Weight (%)
Airframe	Figure 3.18	2731	45.5
FV Cells (52 x)	125x125(each)	758	12.6
MPPT	140x65x31	185	3.1
Batteries (2 x)	136x43x28	702	11.8
ESC	70x31.5x10	73	1.2
Motor	49.6x37.7	198	3.3
Propeller	381 (length)	25	0.4
Wiring & others	-	240	4
Wing Servos (2x)	32x23x12	25	0.4
Tail Servos (2x)	32x23x12	20	0.3
LRS	62x34x10	18	0.3
APM 2.6	67x41x15	32	0.5
Radio Telemetry	130x17x12	14	0.2
Power Module	152x22x12	24	0.4
GPS	38x38x8.5	24	0.4
Airspeed Sensor	35x30x17	15	0.2
Sonar	25x22x20	10	0.2
Camera set	35x25x25	63	1
OSD	43x21x8	5	0.1
Video Tx	49x25x8	31	0.5
Tx Antenna	-	14	0.2
Wiring & others	-	110	1.9
Extra Payload	-	690	11.5
Total		6007	100
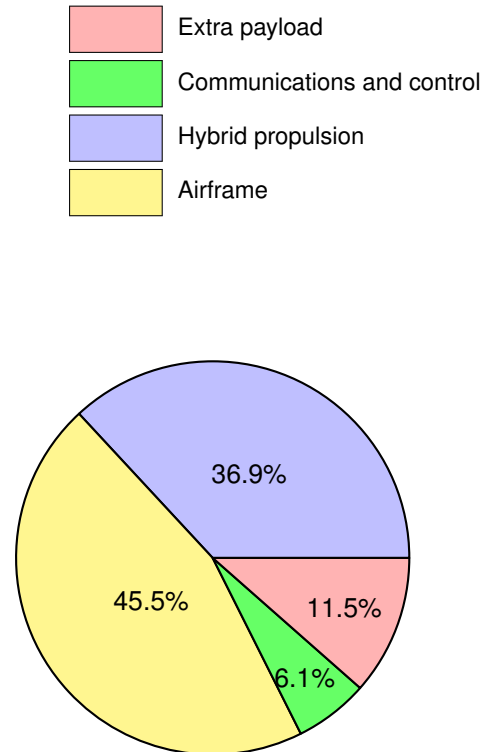
(a) Components dimensions and weight distribution.

Extra payload

Communications and control

Hybrid propulsion

Airframe

36.9%

45.5%

11.5%

6.1%

(b) Relative mass distribution.

Figure 3.19: LEEUAV's weight summary results.

Throughout the project there are going to be observed several mass distribution variations, from the initial sizing, through preliminary and detailed designs, until the construction stage. The weight proportions present in Figure 3.19 are converged values that resulted from the completion of the next stage, the preliminary project. It should be noted that the sum of the extra payload weight with communication components yields a value close to the maximum payload of 10 N specified on the mission requirements.

Chapter 4

Preliminary Project

In this chapter the iterative process involving preliminary performance calculations is described. Aerodynamics, propulsion, stability and control are all related to each other, as schematized in Figure 4.1, so the work is not necessarily presented by the order it was done. By the end of this chapter, the overall dimensions of the aircraft will have been defined, as well as the propulsion system and general placement of all airborne components.
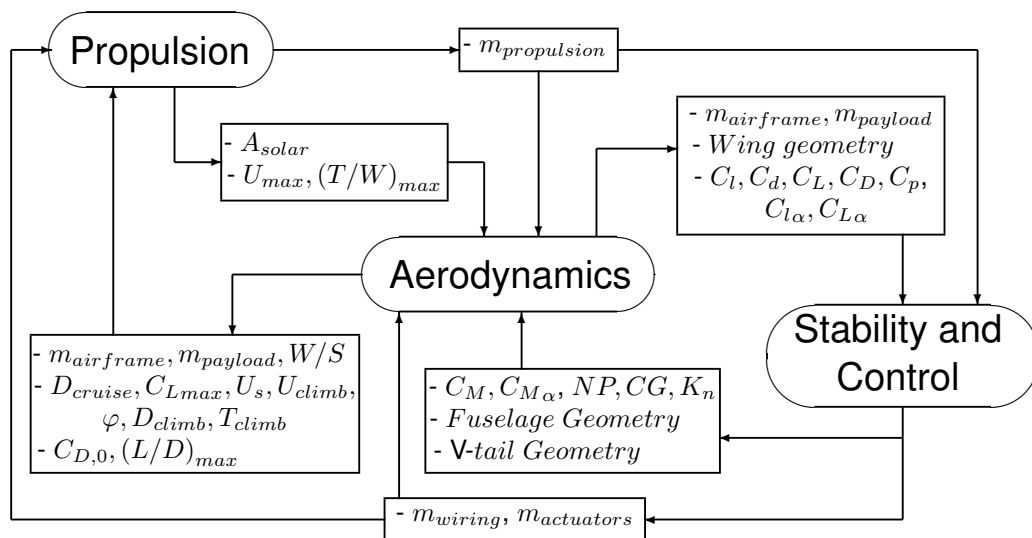
Figure 4.1: Data transfer scheme between Aerodynamics, Propulsion and Stability and Control.

Since there are variables in Figure 4.1 that still have not been mentioned, it is recalled that their meaning can be found in this thesis nomenclature section.

4.1 Aerodynamics

Due to time restrictions, it was not possible to perform Computational Fluid Dynamics (CFD) analysis with high fidelity tools capable of managing multi-physics and complex geometries like the commercial software STAR-CCM+$^{®}$ used in [35]. Instead, to enable a swift processing of aerodynamic results, an open source software called XFLR5 was chosen. XFLR5 was developed from the two-dimensional

panel method implementation XFOIL by Drela [84], which was an interactive program that utilized a two dimensional panel method code with integral boundary layer theory to analyse airfoils in viscous or inviscid flow fields. Presently, the XFLR5's capabilities include 2D airfoil direct analysis as well as 3D wing analysis based on several methods at choice including the Lifting Line Theory (LLT), the 3D Panel Method and the Vortex Lattice Method (VLM), all explained in [85].

4.1.1 Aerodynamic Software Accuracy

Since 3D Panel Method is only available for single wing analysis and LLT does not produce accurate results for geometries with low aspect ratio and high dihedral, such as the V-tail of the updated LEEUAV concept, the most appropriate 3D analysis method found is VLM. To verify the accuracy of VLM, XFLR5 was employed with airflow characteristics and lifting geometries similar to the ones used in the high fidelity CFD analysis made for the first generation LEEUAV in steady flight [35]. The results of both software were compared afterwards.

In all simulations computed on XFLR5, both wing and tail are the only aerodynamic geometries present, as perceptible from Figure 4.2. Incorporating a fuselage, like it was done in STAR-CCM+® [35], is also possible in XFLR5 but not recommended by software developers, as the results of its aerodynamic influence are generally not very satisfactory [85]. Still, XFLR5 results are known for being reasonably accurate for model sailplanes operating at low Reynolds number.

(a) Geometry drawn with CAD [68].   (b) Geometry considered in XFLR5.
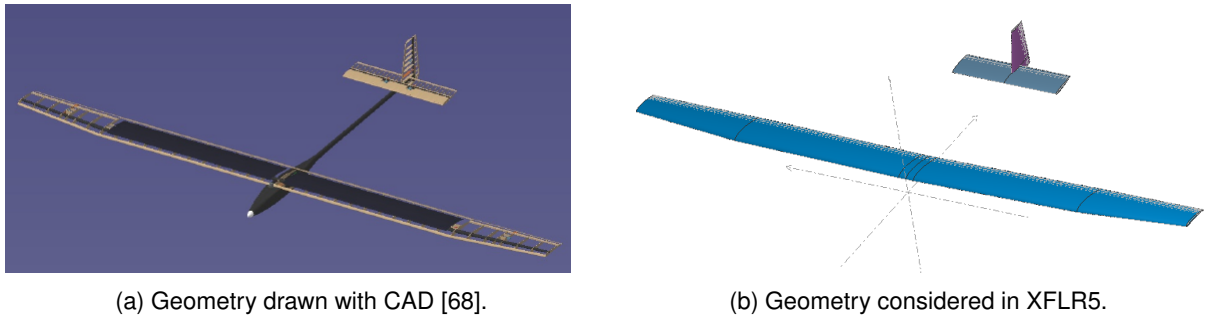
Figure 4.2: First generation LEEUAV geometry.

This software allows the user to control the density of the computational grid, always with rectangular divisions, within a certain range of panel elements. In this project, the grids applied on the geometry portions with constant chord are uniformly divided in chord-wise and span-wise directions. As for tapered surfaces, the only difference is that the grid suffers geometric shrinkage span-wise, thinning from the inner sections to the tip.

Three grids were generated for this study, having 822, 1600 and 3968 elements. Figure 4.4a shows that the lift coefficient C_L predicted with every grid considered in XFLR5 is rather accurate, when compared with STAR-CCM+®, for angles of attack α between -5º and 2º. A closer analysis shows that in cruise conditions ($\alpha = 0$) the coarser grid presents the higher discrepancy, while the 1600 element grid has the closest result to the STAR-CCM+® analysis, followed by the finer grid (3968 elements), which was the only one that overestimated C_L.

(a) C_L as function of α.

(b) C_D as function of α.
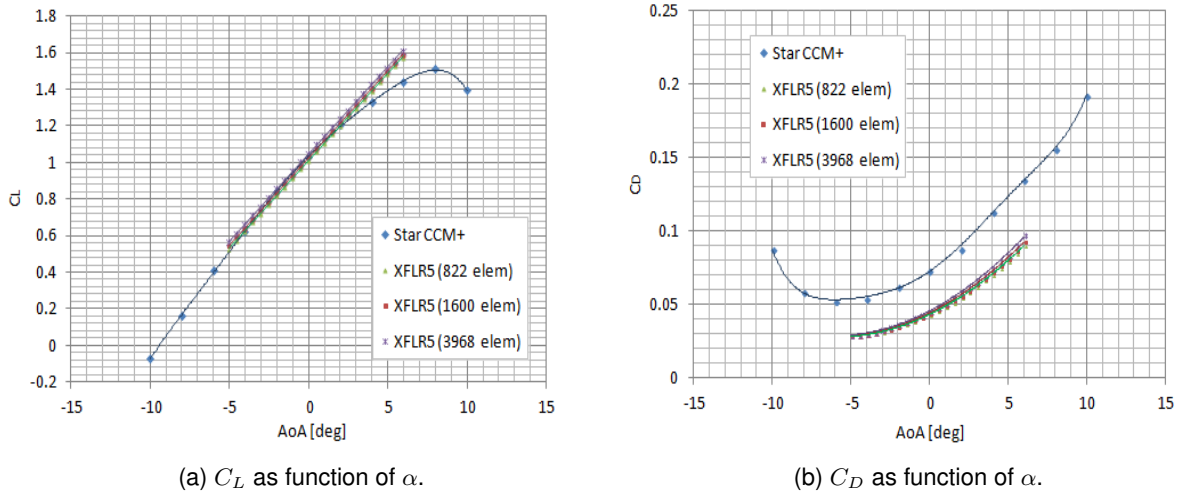
Figure 4.3: Original LEEUAV cruise performance charts (U=7.53 m/s) [35].

On the other hand, Figure 4.4b confirms that XFLR5 underpredicts global drag coefficient real values. This outcome was expected since XFLR5 utilizes information within previously XFoil-generated polars, at several Reynolds number, to extrapolate the 3D viscous drag component. For this same reason, the airplane performance outputs do not include results close to stall angles, in this analysis the computed angle of attack has been limited to values between -5º to 6º. A closer inspection on the output files revealed that both shear and pressure components of drag were underpredicted by VLM.

(a) C_L.

(b) C_D.
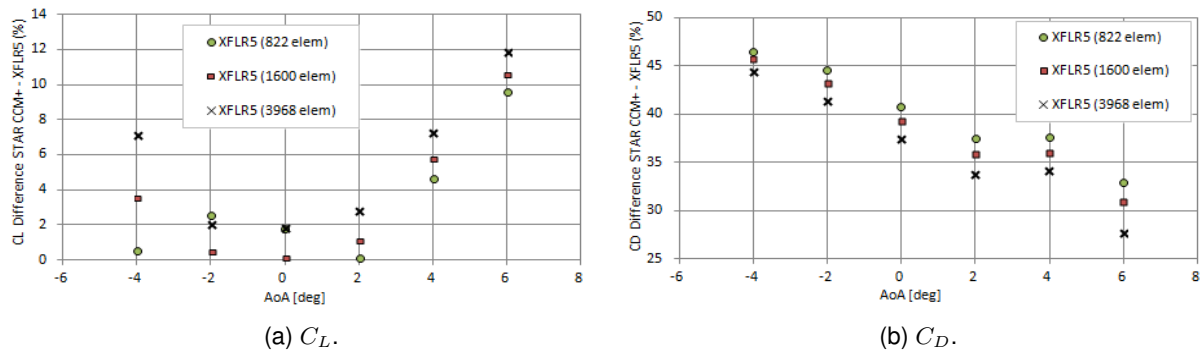
Figure 4.4: Percentage difference between XFLR5 and STAR-CCM+® analysis results.

Analyzing the percentage difference between XFLR5 and STAR-CCM+® analysis results of the first generation LEEUAV cruise flight, illustrated in figure 4.4, it was observed that a grid with 1600 elements provides the best compromise between accuracy and computation time. Therefore, for those specific analysis results, in Figure 4.3, correction functions (4.1) and (4.2) were calculated, assuming the form $Z_x(\alpha) = C_x(\alpha)_{STAR-CCM+}/C_x(\alpha)_{XFLR5}$, where x is either lift (L) or drag (D).

$$Z_L(\alpha) = \begin{cases} 1.008 - (8.41 \cdot 10^{-3})\alpha - (2.96 \cdot 10^{-3})\alpha^2 + (3.56 \cdot 10^{-4})\alpha^3, & \text{if } \alpha \le -2.8º \text{ \& } \alpha \ge 0.7º \\ 1, & \text{if } -2.8º < \alpha < 0.7º \end{cases} \tag{4.1}$$

$$Z_D(\alpha) = 1.6375 - (2.723 \cdot 10^{-2})\alpha + (6.105 \cdot 10^{-3})\alpha^2 - (9.951 \cdot 10^{-4})\alpha^3 - (1.264 \cdot 10^{-4})\alpha^4 \tag{4.2}$$

To recoup for XFLR5 output discrepancies, it was decided to apply Z_x functions to all XFLR5 3D

43

analysis performed while iterating the preliminary project. Such early generalization of these equations has not been acknowledged bibliographically, therefore, by retracing the differences between the preceding and new LEEUAV concepts while recalling flow natural transitions on an aircraft, the accuracy of the correction becomes at least doubtful.

For instance, the evolution of laminar separation bubbles on the wings surface and development of separated flow until massive lift loss, as described thoroughly in [35], is influenced by variables, such as the wingspan, airfoil or fuselage shape, that kept diverging from the first concept as the project progressed. So, stall is not guaranteed to start occurring at the pace imposed by expression (4.1). The same logic applies to the drag polar reformulation due to Equation (4.2), that also does not hold into account flow interactions between updated aerodynamic surfaces.

In spite of the mentioned incoherence, the practical purpose of this correction to the mission is achieved by improving the XFLR5 output margin of error while rearranging lift and drag predictions, for angles of attack between -5º and 5.5º, more conservatively.

4.1.2 Cruise Stage Computation

Steady flight is achieved when the overall lift produced matches the airplane's flying weight. Subsequently, sizing the wing to generate a resultant lifting force matching the maximum take-off weight, at a stipulated cruise velocity, was appointed as the first design requirement to be met.

Recalling the mission requirements in Section 2.1, the project cruise speed is 7.53 m/s and the altitude is fixed at 1300 m. Having defined cruise velocity and atmospheric data, the aerodynamic geometries (wing and tail) of the LEEUAV conjectured on the initial sizing (Figure 3.18) went trough VLM computational analyses. By counter-weighing the software's output lift with the initial MTOW estimate, it was clear that the wing had to produce more lift. Thereupon, at this stage, the geometry update focused solely on the wing. As adjustments were being made and reinserted in XFLR5, the airframe weight was recalculated with Equation (3.1) and the wire length linking servos updated as well. The whole process, illustrated by the flowchart in Figure 4.5, was reiterated until MTOW equaled the lift computed aerodynamically.
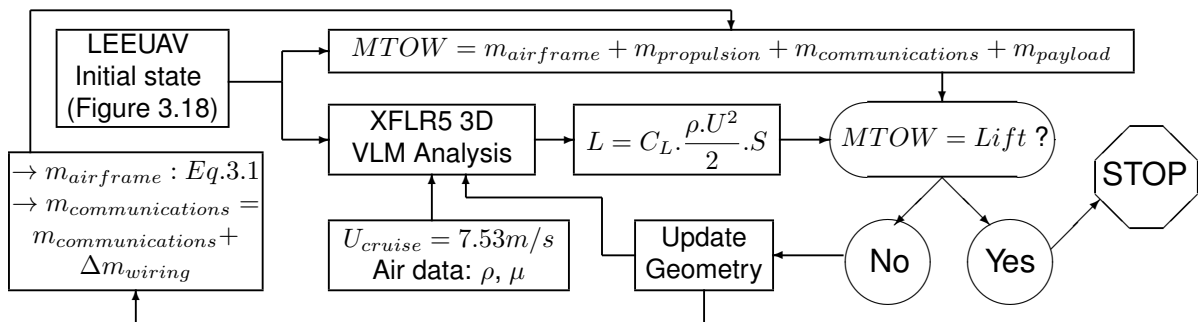
Figure 4.5: Initial aerodynamic iterative scheme for cruise stage.

Chordwise there were not any changes on the wing, because increasing the mean chord would admittedly enlarge the existing gap between MTOW and produced lift at cruise speed. Conversely,

raising the wingspan beyond the mark of five meters could narrow down that difference, however, that possibility was not embraced since it would add further structural and transportation issues.

Instead, the approach followed was to modify the wing's airfoil, while increasing the wingspan up to five meters. Formerly the airfoil had a curvature of 5.3%, which was renewed to 7.5% so that its lift coefficient raised. Envisioning the prototype's construction, the minimum trailing edge thickness, at the wingtip, was increased to 2 mm, as portrayed in Figure 4.6. Such modification made the relative thickness go up from 12 % to 13 %, which increases maintenance damage tolerance and eases the manufacturing process.
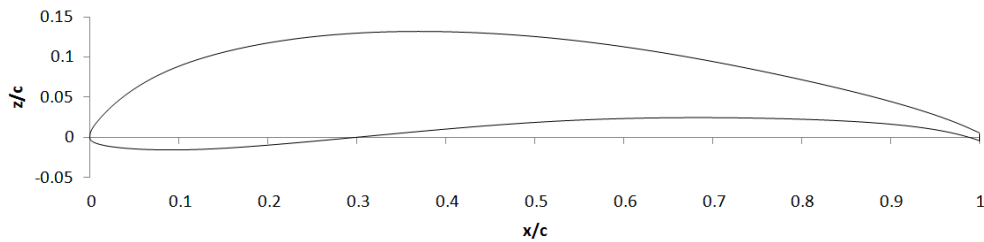
Figure 4.6: Updated wing airfoil of the LEEUAV ($t/c = 13\%$).

Figure 4.7 shows the aerodynamic charts of the preceding and updated airfoils, obtained from XFLR5 airfoil direct analysis tool at $Re = 150000$, where each airfoil is signalized by its relative thickness.

(a) C_l as function of AoA.

(b) C_d as function of AoA.

(c) C_l as function of C_d.

(d) C_l/C_d as function of C_l.
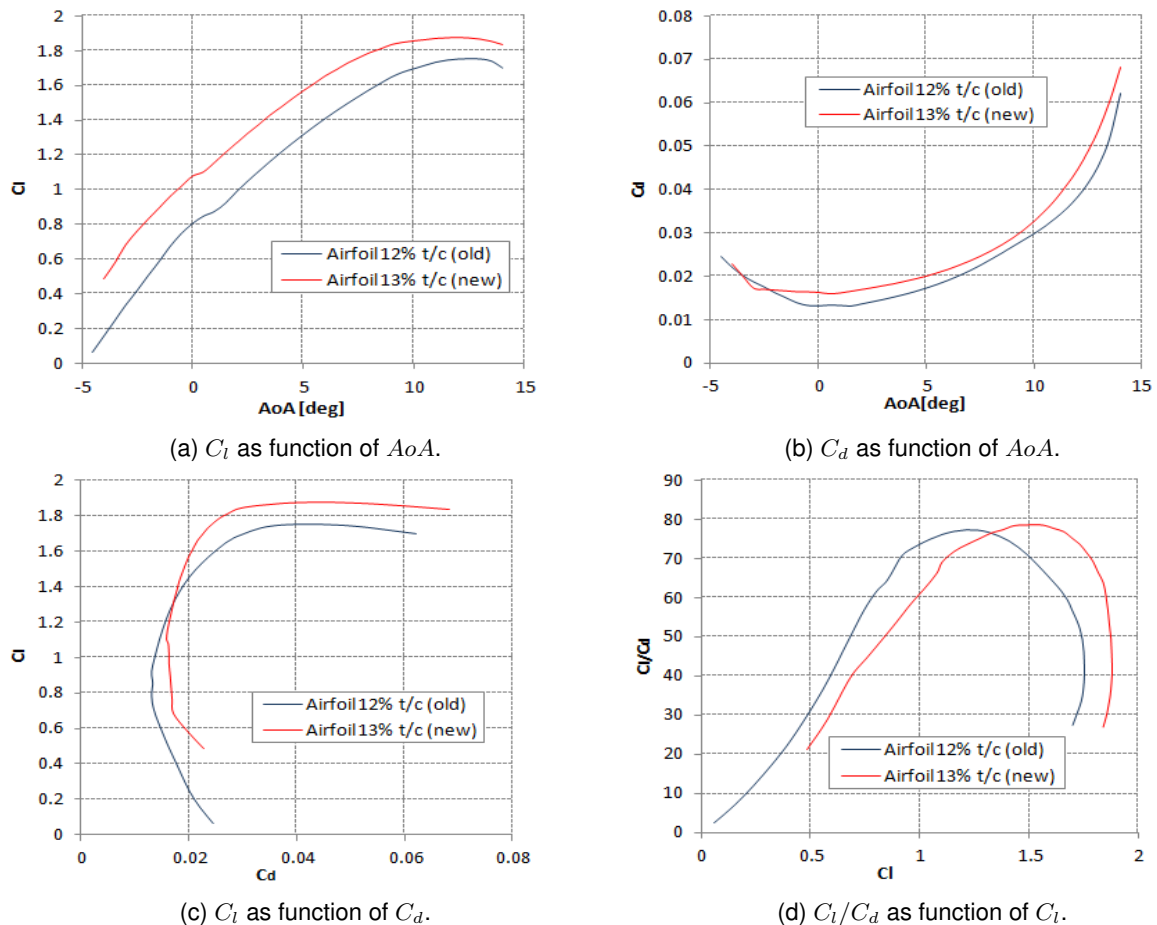
Figure 4.7: LEEUAV Airfoil aerodynamic charts ($Re = 150000$).

45

Lift gains are more perceivable on the C_l vs AoA curves of Figure 4.7a, in which a positive 5º incidence angle, with respect to the fuselage longitudinal axis, was assigned to most wing sections. Therefore, the correspondent C_l of 1.57 is the approximated value considered for cruise conditions.

Increasing the airfoil's curvature, and thereby its lift, came at the expense of adding more drag to the operation, as observed in Figure 4.7b. Notwithstanding, it'll be verified, still on the preliminary project, that the additional airfoil drag does not prevent the LEEUAV from fulfilling its 8 hour cruise requirement.

It is noticeable, in Figure 4.7c, that the airfoil drag coefficient was kept minimum between the lift coefficient range of 0.6 to 1.5, assuming a value of 0.016 when the lift coefficient equals approximately 1.1. Another occurrence to point out from the C_l vs C_d graph is the fact that at the cruise lift coefficient (C_l=1.57) the drag is smaller on the more recent airfoil, which is justified by the difference on the angle of attack required in both airfoils to achieve such lift coefficient. Looking at Figure 4.7d, the updated airfoil's glide ratio, that is maximum when C_l equals 1.52, surpasses its predecessor at current cruise conditions. The updated wing airfoil aerodynamic performance data is listed in Table 4.1.

C_{lmax}	$\alpha_{C_{Lmax}}$	$C_{l\alpha}$	C_{dmin}	$C_l/C_{d_{max}}$	$\alpha_{C_l/C_{d_{max}}}$
1.88	12º	0.1014/º	0.016	78.56	4.5º

Table 4.1: LEEUAV airfoil aerodynamic performance data.

On his detailed aerodynamic analysis of the first generation LEEUAV, Silva [35] described how the laminar separation bubbles form on the wings as a consequence of the laminar boundary layer detachment and later re-attachment, and how, passing an angle of attack of 8º, leading edge loss bursts. During a parametric optimization study, also performed in [35], wing washout was foreseen as an option to delay this effect. Thereupon, the analyzed geometry of the LEEUAV had its wing modified by reducing its incident angle of attack in 4º from the aileron inner section until the wing tip.

(a) Original LEEUAV configuration.   (b) LEEUAV with wing washout.
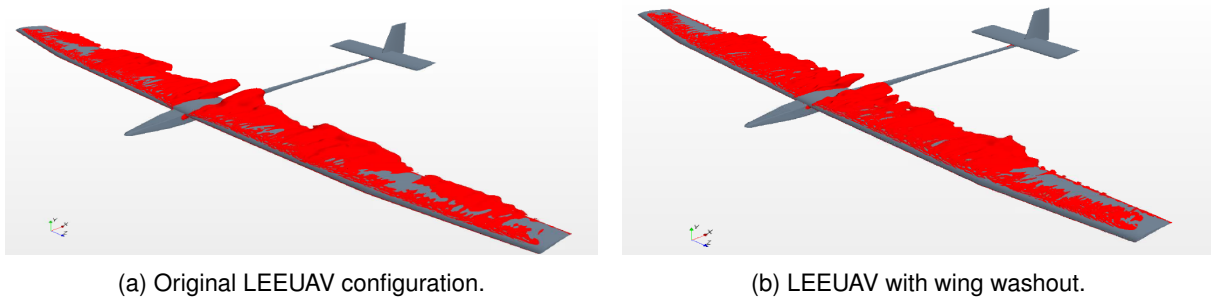
Figure 4.8: LEEUAV isosurfaces of reversed flow (AoA=10º) [35].

Figure 4.8, obtained from high fidelity CFD software STAR-CCM+®, allows to compare the regions of reversed flow at an angle of attack of 10º between the plain LEEUAV design and the one with wing washout. Reducing the wing twist proved to reduce flow separation in the wing region where the ailerons are located, thus guarantying aileron control at that angle of attack. According to Silva [35], the wing washout applied on the conventional configuration resulted in a decrease in the lift coefficient of 7% and 20% in the drag coefficient. Seeing the benefits it could have had on the first airplane prototype, it was decided to add the wing washout feature in the iterative process of Figure 4.5. The same absolute

torsion was applied on the aileron sections, meaning a wing AoA of 1º on the tip and 5º on the sections with constant chord.
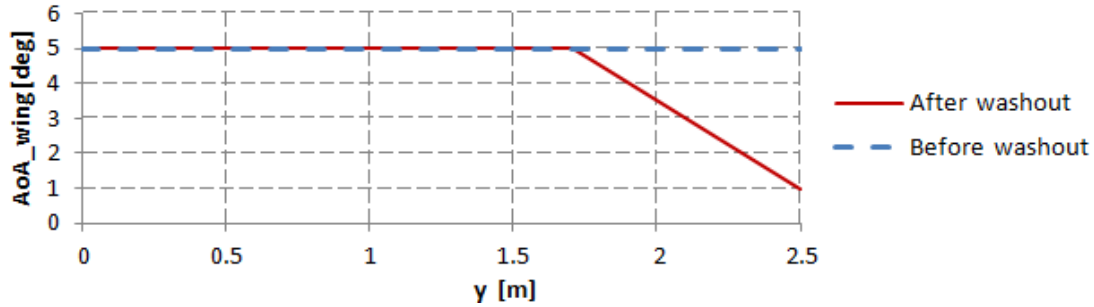
Figure 4.9: Wing AoA distribution along half the wingspan of the LEEUAV.

As seen in Figure 4.9, that shows the angle of attack of the wing spanwise before and after the washout, in XFLR5 the twist distribution is linear between two cross sections. Moreover, the twist rotation center is located at the quarter chord point from the leading edge. From the ensuing VLM computational analysis came that washout reduced lift and drag coefficients 3% and 5.7% respectively, which, in comparison with the values given in [35], denotes a rather conservative lift-to-drag ratio increase, that was assumed throughout the project.

The final design lift and drag data, computed at cruise velocity, is shown in Figure 4.10 for all simulated angles of attack. A total of twenty two angles of attack were simulated from -5º to 5.5º, with increments of 0.5º on XFLR5, using VLM method.

Figure 4.10a displays the LEEUAV lift coefficient evolution with the angle of attack. At steady flight ($\alpha_{airplane} = 0^o$, $\alpha_{wing} = 5^o$), the lift coefficient is rounded to 1.153 . Due to computational limitations of the adjustment defined in Section 4.1.1 it was not possible to determine the maximum lift coefficient and its angle of attack, so those values were extrapolated from the curve in figure 4.10a, in a conservative way, whenever necessary. The lift curve slope $C_{L\alpha}$, whose value in steady flight is approximately $0.08943/^o$, will be employed for stability studies.

Figure 4.10b shows the LEEUAV drag polar. Again, given the aerodynamic software correction limitations, minimum drag and respective angle of attack factual values remain unknown. At angles of attack below 0º, C_D increases very little when compared to C_L because, recalling that it has an incidence angle of five degrees with respect to the fuselage, the wing becomes more aligned with the flow, which makes form drag is considerably lower. In the lift coefficient range of 1.32 to 1.53, that corresponds to an angle of attack in the range of 1.28º to 5.5º, the drag polar presents an almost linear behavior. It is also at this angle of attack range that the lift slope slightly decreases. An explanation for this behavior might be related with the region of separated flow that starts to develop at this angle of attack range in the wing root region. For angles of attack above 5.5º it is uncertain when does massive flow separation occur over the wing surfaces.

Figures 4.10c and 4.10d show the C_L/C_D and $C_L{}^{3/2}/C_D$ evolution with C_L. The first figure gives an idea of the lift coefficient the airplane should have to maximize its range and endurance, while the second indicates the airplane maximum endurance in terms of its lift coefficient. Figure 4.10c shows

(a) C_L as function of AoA.

(b) C_L as function of C_D.

(c) C_L/C_D as function of C_L.

(d) $C_L{}^{3/2}/C_D$ as function of C_L.
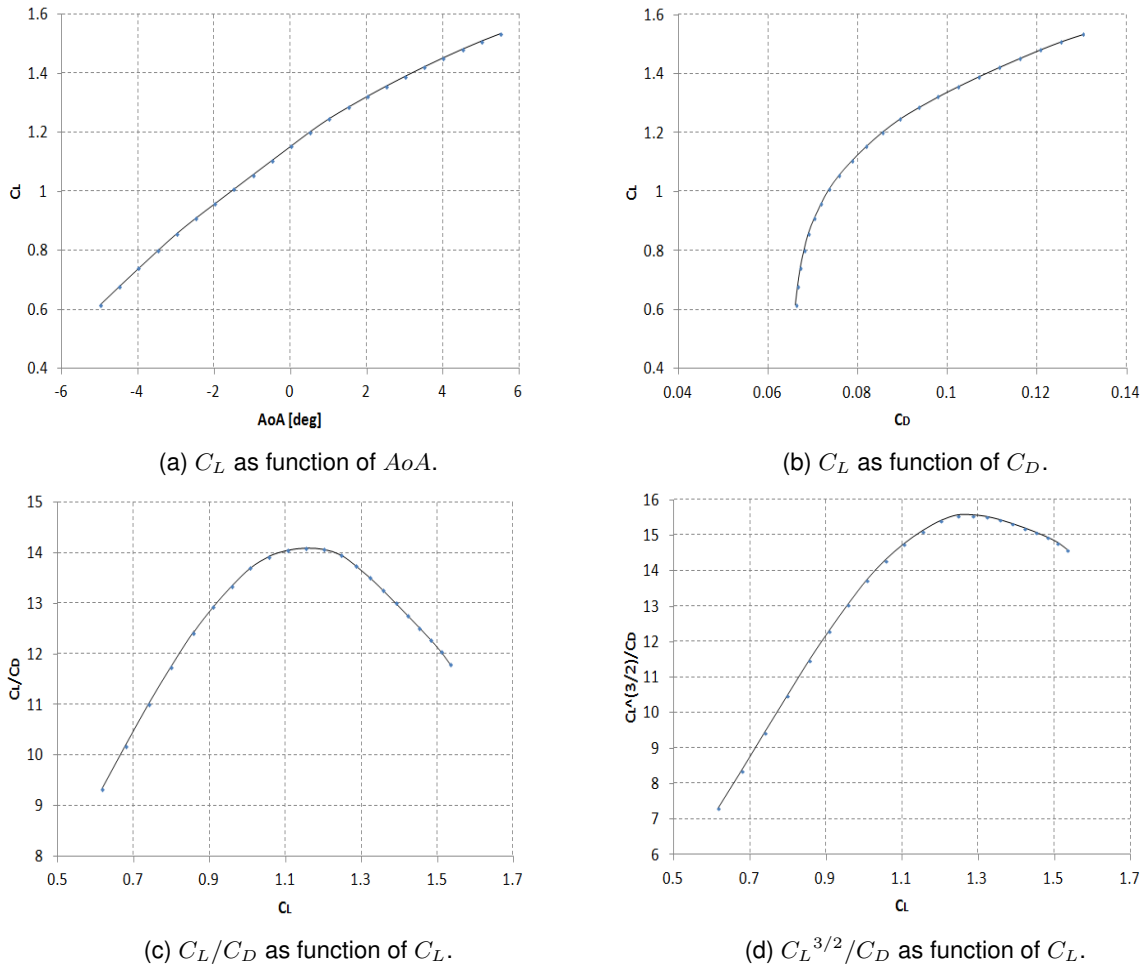
Figure 4.10: LEEUAV aerodynamic performance charts (U=7.53 m/s).

that the glide ratio has its peak when the lift coefficient is between 1.1 and 1.2, which occurs when flying the aircraft at angles of attack close to 0º, thus it is at this angle of attack the LEEUAV should operate to maximize its range and endurance during its cruise flight phase. From Figure 4.10d it is discernible that to maximize endurance the airplane would have to fly at higher lift coefficients, in the order of 1.3, which means increasing the angle of attack in about 1.5º.

Table 4.2 summarizes the LEEUAV aerodynamic performance data. It should be noted that climb, whose performance calculations are explained in Section 4.3.1, occurs at a slightly different velocity than cruise. Therefore its drag coefficient C_{Dclimb} was estimated using distinct aerodynamic performance charts, similar to the ones in Figure 4.10 but computed in XFLR5 at the respective free stream speed (U_{climb}=7.67 m/s), providing a more conservative value.

Maximum lift coefficient *	C_{Lmax}	1.6
Maximum lift angle of attack *	$\alpha_{C_{Lmax}}$	7.4 º
Zero lift angle of attack *	$\alpha_{0\,lift}$	-9.33 º
Lift vs angle of attack curve slope	$C_{L\alpha}$	0.0894 /º
Minimum drag coefficient *	C_{Dmin}	0.066
Zero lift drag coefficient *	$C_{D,0}$	0.104
Maximum lift-to-drag ratio	$C_L/C_{D\,max}$	14.09
Angle of attack of maximum lift-to-drag ratio	$\alpha_{C_L/C_{D\,max}}$	0 º
Cruise lift coefficient	$C_{Lcruise}$	1.153
Cruise drag coefficient	$C_{Dcruise}$	0.08
Climb drag coefficient *	C_{Dclimb}	0.129
Climb angle of attack *	α_{climb}	5.5 º

Table 4.2: LEEUAV aerodynamic performance data (extrapolated or estimated data is marked with *).

4.2 Stability and Control

The stability project branch came pursuant to propulsion and energy management studies. Recalling the AHP results from Chapter 2, stability and control have 4% relative importance, easily surpassed by propulsion and solar panels integration, with priority values of 13% and 20%, respectively. Notwithstanding, given the close relation between aerodynamic and stability results and the computational procedures followed to obtain both, it was seen as permissive to report stability studies at this point.

4.2.1 Static Stability

To support airworthiness towards long endurance missions at low speed, natural longitudinal stability was targeted by fulfilling two design prerequisites. Defined as the dimensionless distance, given in percentage of the mean aerodynamic chord (MAC), between the neutral point (NP) and the center of gravity (CG), the static margin K_n was assured positive. By other words, assuming a longitudinal axis with origin upstream and pointing towards the tail, the CG was placed behind of the AC, that is

$$K_n = \frac{x_{NP} - x_{CG}}{MAC} > 0. \tag{4.3}$$

At the same time, the V-tail was arranged to counteract the moment that comes from the wing, so that the overall moment coefficient is kept close to null in steady flight conditions.

Resorting to CAD software SolidWorks®, the second generation LEEUAV and the majority of on-board components were modeled, as shown in Figure 4.11, and the respective mass centers positioning pinpointed from there. Then, the airplane's updated inertia was transferred to XFLR5, where components and parts, excluding wing and tail-plane, were replaced by punctual masses.

Figure 4.12 displays the aircraft visualized in XFLR5 with a merely symbolic representation of individual mass centers. Again, it is remarked that the only geometries considered in XFLR5 3D analysis are the wing and the V-tail. Table 4.3 lists the mass center position and weight of all parts and components of the LEEUAV, that served as final input to the stability analysis. The components numbering

matches the labels attributed to the mass representations in Figure 4.12. The extra payload was not accounted for because it was assumed that its position corresponds to the center of gravity. The axis position considered is also pinpointed in Figure 4.12.
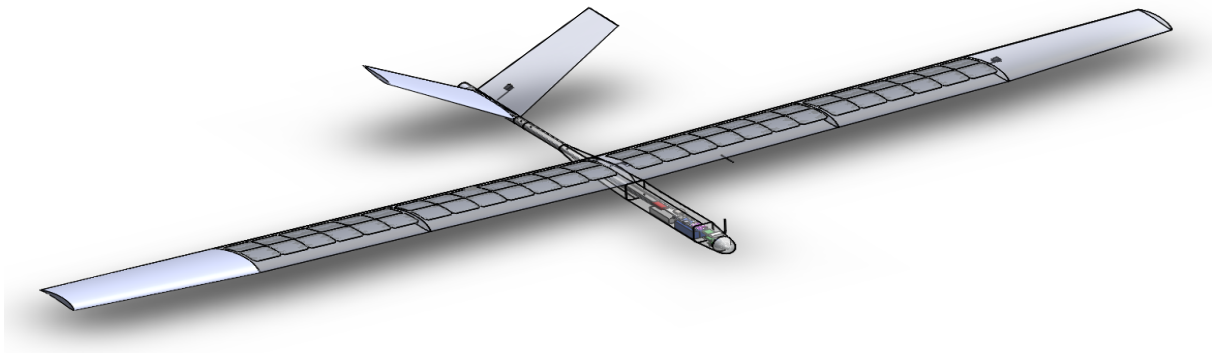
Figure 4.11: LEEUAV assembly drawn in CAD software SolidWorks®.
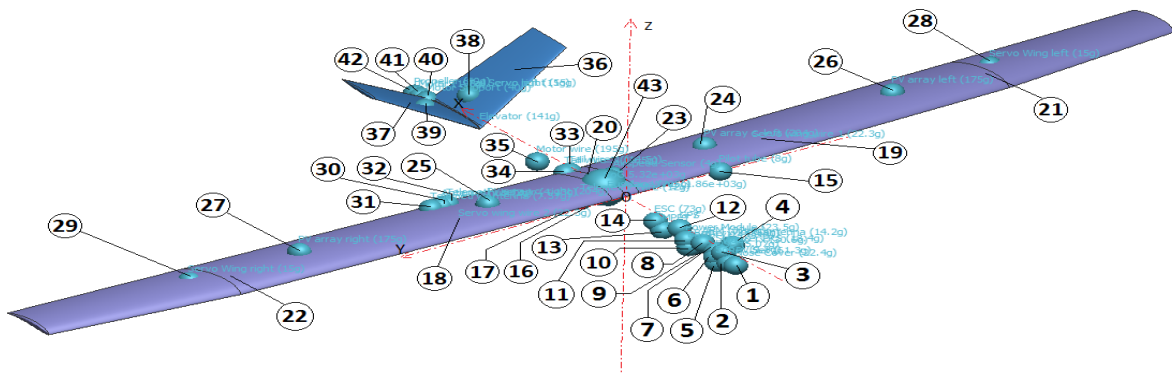
Figure 4.12: LEEUAV represented in XFLR5 with individual mass centers used in stability studies.

To achieve the mass distribution listed in Table 4.3, the VLM analysis loop had to be resumed with incremental modifications in the weight distribution and V-tail characteristics until the results indicated that the longitudinal stability prerequisites were accomplished. Figure 4.13 illustrates the whole procedure, which also includes the previous aerodynamic loop for cruise (Figure 4.5) to attest that lift keeps matching with flying weight.
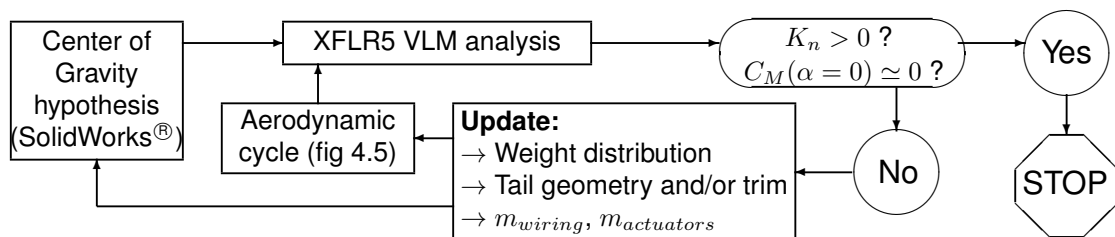
Figure 4.13: Static stability iterative scheme.

Arranging the present stability solution for the rear pusher configuration was an intricate task. On one hand, pushing the engine too far back from the AC readily causes a deficit of static margin , on the other hand, the tail-plane cannot cancel the pitch moment from the wing if it is not distant enough.

The overall moment coefficient as function of angle of attack, in Figure 4.14a, evidences that the

#		1	2	3	4	5	6	7	8	9	10	11
Component		Nose cover	RPV Set	Video Tx	Video Antenna	Sonar	OSD	LRS	Autopilot	Battery 3S LiPo		Power Module
Mass Center	x	-667.32	-625.61	-583.05	-582.93	-556.06	-547.48	-532.55	-466.48	-402	-402	-386.75
Position	y	0	-1.03	-5.95	-46.69	1.35	1.68	-10.72	-1.38	14.61	-15.33	13.77
(mm)	z	-55.27	-62.14	-27.92	2.18	-92.52	-64.77	-45.18	-30.03	-77.39	-77.39	-45.7
Weight (g)		22	61	30	14	9.8	5	18	32	351	351	23
#		12	13	14	15	16	17	18	19	20	21	22
Component		GPS	MPPT	ESC	Pitot tube	Fuselage	Telemetry wire	Wing servo wire		Wing central part	Wing lateral part	
Mass Center	x	-326.42	-230.22	-188.83	0.26	104.51	104.9	121.18	121.18	147.77	157.48	157.48
Position	y	-0.21	0.54	5.9	-418.81	0.41	121.37	-652.19	652.19	-0.01	-1638.12	1638.05
(mm)	z	-15.28	-75.2	-42.8	0.05	-52.6	-31.21	-1.18	-1.18	15.75	34.91	34.91
Weight (g)		24	185	73	8	705	12	22	22	673	595	595
#		23	24	25	26	27	28	29	30	31	32	33
Component		Airspeed sensor	7x2 PV array		6x2 PV array		Wing servo		Antenna hub	Telemetry antenna	Telemetry sensor	Tail wire
Mass Center	x	176.6	180.99	180.99	182.46	182.46	218.99	218.99	312.23	312.23	312.46	351.27
Position	y	-72.45	-481.65	481.65	-1318	1318.11	-1779.72	1779.72	588.36	636.72	564.75	-9.4
(mm)	z	4.62	31.21	31.21	46.27	46.28	21.17	21.17	-6.21	-5.34	-6.73	-38.55
Weight (g)		4	204	204	175	175	15	15	2	8	4	14
#		34	35	36	37	38	39	40	41	42	43	
Component		Tail wire	Motor Wire	V-tail halves		Tail servo		Mount set	Motor	Propeller	CG	
Mass Center	x	351.27	534.55	1019.59	1019.59	1066.51	1066.51	1205.05	1247.85	1276.15	131.037	
Position	y	9.4	0.41	-224.87	224.87	-85.15	85.15	0	0	0	0.743	
(mm)	z	-38.55	-67.74	99.38	99.38	11.64	11.64	-55.27	-55.27	-55.27	-11.293	
Weight (g)		14	195	70	70	15	15	40	198	50	5321	

Table 4.3: Individual mass center positions and weights of the LEEUAV (the components numbering matches the labels in Figure 4.12).

LEEUAV, as it was designed, has natural longitudinal stability. At positive angles of attack it produces a pitch-down moment whereas at negative angles of attack its tendency is the opposite. In order to nullify the moment coefficient at cruise AoA of 0º, the V-tail, featuring a modified NACA0008 with 1mm trailing edge thickness, was trimmed with an incidence negative angle of 3º with respect to the fuselage. It has been noted that when the wing stalls ($\alpha = 7.2$º) the angle of attack of the tail is at 4.2º. Knowing that the maximum 2D lift coefficient of the NACA0008 airfoil at the cruise Reynolds number is 7.5º, the empenage is not expected to stall before the wing. Furthermore, the tail-plane dimensions were kept from the initial sizing, because any notorious reduction would impose an excessive fuselage length.

Incidentally, a flaw that is highlighted from this stability study approach has to do with the absence of fuselage weight modifications following dimension updates. This source of error is tolerated during the preliminary project but must be addressed afterwards in the detailed design, mentioned in Chapter 6.

The static margin, as presented Figure 4.14b, was calculated with the following equation from [86]

$$C_{M_\alpha} = -K_n C_{L\alpha} <=> K_n = -\frac{C_{M_\alpha}}{C_{L\alpha}}, \tag{4.4}$$

where C_{L_α} and C_{M_α} correspond to the graph slopes in Figures 4.10a and 4.14a, respectively.

In steady flight it is observed that $K_n = 5.6\%$, corresponding to, according to a referential with origin in the leading edge, a CG position at 38.86% of the MAC, which was considered acceptable for the mission profile. Table 4.4 summarizes the LEEUAV static stability data. The axis used to measure the longitudinal coordinates of the CG and AC is taken from Figure 4.12.
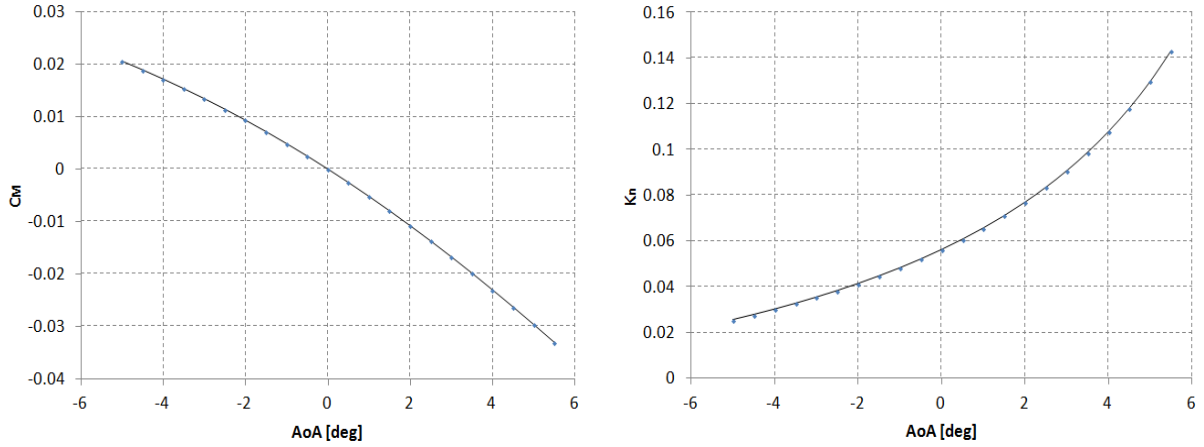
(a) Moment coefficient as function of angle of attack.

(b) Static margin as function of angle of attack.

Figure 4.14: LEEUAV stability charts (U=7.53 m/s).

$C_M\ (\alpha = 0)$	$C_{M_\alpha}\ (\alpha = 0)$	x_{CG}	x_{NP}	$K_n\ (\alpha = 0)$
0	-0.005 /º	131.07 mm	147.936 mm	5.6 %

Table 4.4: LEEUAV static stability data.

4.2.2 Dynamic Stability

The on-board presence of an APM 2.6 autopilot with several flight stabilization modes, associated with an already established natural longitudinal stability, allowed to treat dynamic stability as a non-critical part of the project. Since XFLR5 also features a built-in dynamic stability analysis tool, described in [85], it was possible to swiftly access stability modes in steady flight conditions. This served only to verify longitudinal and lateral stability characteristics.

	Longitudinal modes		Lateral Modes		
	Phugoid	Short Period	Spiral	Roll Damping	Dutch Roll
λ	$-0.0224 \pm 0.901i$	$-4.5760 \pm 1.2089i$	0.2218	-11.2673	$-0.8585 \pm 1.0833i$
ξ	0.025	3.785	——	——	0.792
f (Hz)	0.143	0.753	——	——	0.22

Table 4.5: Dynamic stability modes.

As expected, the longitudinal modes in Table 4.5 have their eigenvalues λ on the left side of the complex plane, meaning they are stable. The phugoid has a particular small damping factor ξ, that is due to its inverse relation with aerodynamics, $\xi_{\text{phugoid}} \approx D/(\sqrt{2}.L)$, further explained in [87]. Figure 4.15 illustrates the time response of the phugoid. The pitch angle θ (Figure 4.15a) starts with a peak amplitude of about 5º and takes about 35 seconds to be reduced to half and more than 200 seconds become negligible. The pitch rate, in Figure 4.15b, presents a similar behavior.

On the other side, the short period is an heavily damped mode. Looking at Figure 4.16a, given an initial state of 9.6º, the pitch angle virtually stabilizes after one second. The same occurs with the pitch rate, in Figure 4.16b, where the initial state assumes a value of -47 º/s.
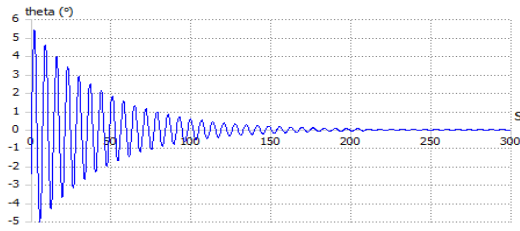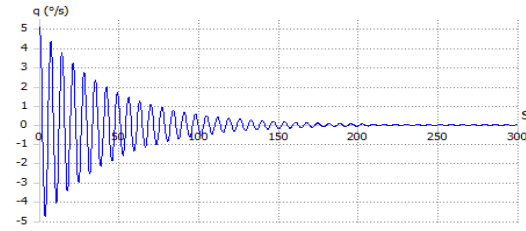
(a) Pitch angle. (b) Pitch rate.

Figure 4.15: Phugoid modal response.
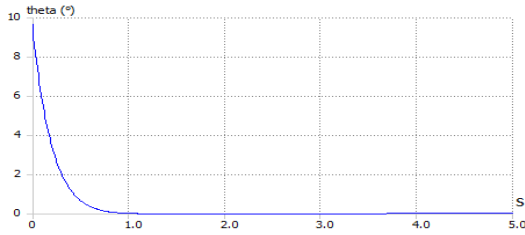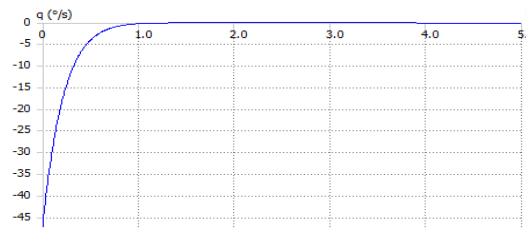
(a) Pitch angle. (b) Pitch rate.

Figure 4.16: Short period modal response.

Among lateral modes, also in Table 4.5, both spiral and roll damping have non-oscillatory nature, therefore it was not possible to retrieve the damping factor and the frequency for those modes. The roll damping is the most stable mode, therefore it is also the fastest to react, as seen in Figure 4.17, where high perturbations in both roll and yaw rates are canceled in less than one second.
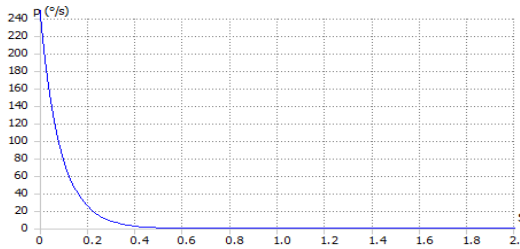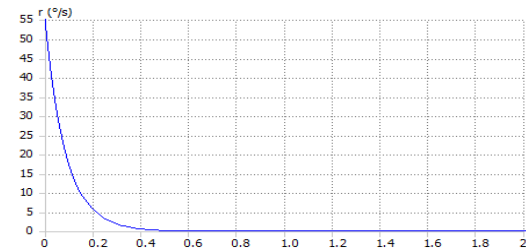
(a) Roll rate. (b) Yaw rate.

Figure 4.17: Roll damping modal response.

The dutch roll is also a mode with solid stability, but it is still notoriously affected by its oscillatory nature. In Figure 4.18 its time response presents an initial overshoot before achieving its settling time, what happens faster for the roll rate than for the yaw rate.

The spiral instability value stands out in Table 4.5. Figure 4.19 shows that both roll rate and yaw rate only need 3 seconds to duplicate initial perturbations of 1.3 $^\circ$/s and 5.3 $^\circ$/s, respectively. This lateral mode is usually unstable and in a conventional configuration airplane it could become marginally unstable, closer to zero, however, that was not possible with the current LEEUAV concept. As a result, the spiral will have to be corrected with the stability augmentation system provided in the autopilot.
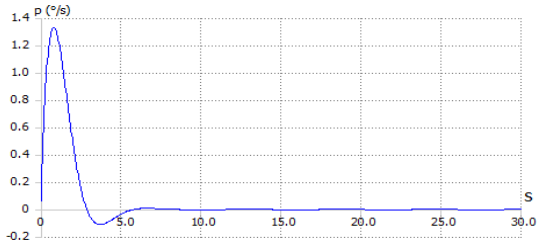
(a) Roll rate.
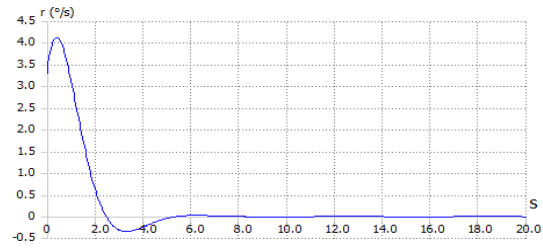
(b) Yaw rate.

Figure 4.18: Dutch roll modal response.
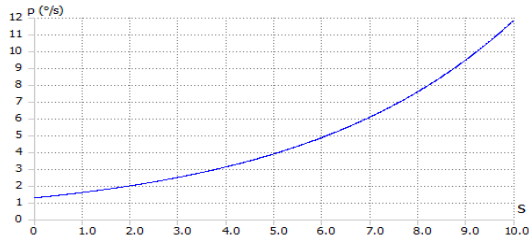
(a) Roll rate.
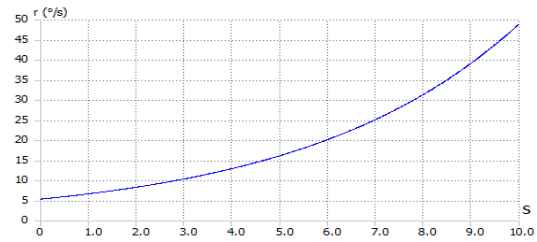
(b) Yaw rate.

Figure 4.19: Spiral modal response.

4.3 Propulsion

Reviewing the mission profile in Figure 2.1, there can be identified two dissimilar steady propulsion states, that correspond to climb and cruise. The choice of components for the propulsive system, already pointed out in Section 3.2.3, has been accredited by knowledge of the exact power requisites during those stages. Short-term climbing flight, most pressing in terms of immediate power consumption, was the first to be examined. Attending to its short duration with respect to the whole mission, it is always assumed that the solar energy received during that stage is negligible.

4.3.1 Required Power and Energy

An aircraft's operational net power corresponds to the product of its thrust with its flying trajectory velocity, $P = T \cdot U$. While thrust in cruise is simply given by the correspondent drag, for climb it was determined using the constant rate of climb, defined as a specific mission requirement. From [88] comes the expression

$$\frac{dh}{dt} = U_{climb} \cdot sin(\varphi) = U_{climb} \cdot \frac{T - D}{W} \tag{4.5}$$

where h stands for altitude, T for thrust, W for weight and φ for the climb angle. The required thrust for climbing was then calculated as $T_{climb} = W sin(\varphi) + D$. Also according to [88], the velocity that is appropriate to the climb conditions can be given by the representative velocity for the take-off, which is defined as a function of the stall velocity (U_s),

$$U_{take-off} = U_{climb} = 1.2 \cdot U_s = 1.2 \cdot \sqrt{\frac{W}{S} \cdot \frac{2}{\rho C_{L max}}} \tag{4.6}$$

54

where C_{Lmax} is the maximum 3D lift coefficient for the aircraft, which was estimated by extrapolation of the C_L plot as function of AoA, in Figure 4.10a. At this point, climb drag is determined with a computational VLM simulation at the respective velocity U_{climb}, whose output is corrected with Equation (4.2). The angle of attack considered is 5.5º, which corresponds to the maximum eligible output in VLM, and the climb angle is 12.5º. Attending to the definition of drag coefficient, $C_D = D/(0.5 \cdot \rho_\infty \cdot U_\infty^2 \cdot S) = D/(q_\infty \cdot S)$, the net power during climb can be given as

$$P_{netclimb} = T_{climb} \cdot U_{climb} = (W sin(\varphi) + C_D q_\infty S) \cdot 1.2 \cdot \sqrt{\frac{W}{S} \cdot \frac{2}{\rho C_{Lmax}}}. \tag{4.7}$$

Considering the efficiency of the different components of the propulsion system, the raw power required in every part of the mission can be determined by Equation (4.8)

$$P_{raw} = \frac{P_{net}}{\eta_{prop}} \qquad , \qquad \eta_{prop} = \eta_{ESC} \cdot \eta_{motor} \cdot \eta_{propeller}. \tag{4.8}$$

Most marked efficiency variations are expected to come from the propeller, which is the only component whose performance is directly affected by aerodynamics. Computed performance data, supplied by APC manufacturer [89], provided estimates of thrust, torque and propeller efficiency over a broad range of model speeds and motor revolutions per minute(RPM). All values of any parameter contained within a certain propeller data file can be represented with a single three dimensional graphic as function of two other listed parameters.

(a) Efficiency as function of thrust and flying speed.

(b) Efficiency graphical calculation with climb regime data.
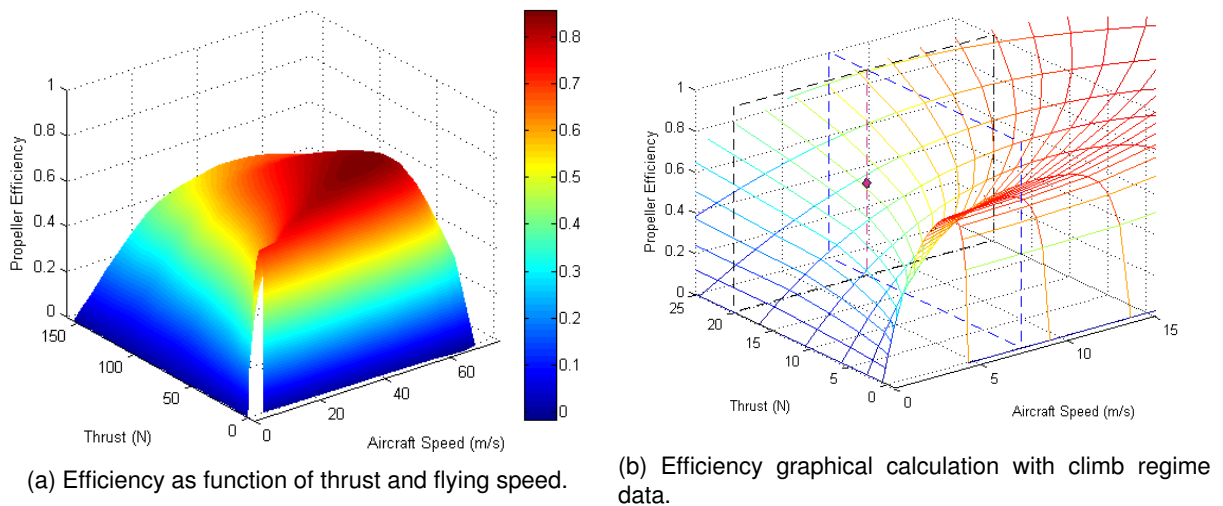
Figure 4.20: Graphical display of 15" x 8" propeller's efficiency data.

Figure 4.20a displays the interpolated efficiency of a 15" x 8" propeller depending on produced thrust and flight velocity. Having already defined the computations for thrust and speed, a MATLAB® routine was written in order to interpolate torque, efficiency and RPM values. A simple way to understand this process is illustrated in Figure 4.20b, where the efficiency surface is zoomed for a better visualization of the climb regime input, which is defined by a plane of constant thrust together with a perpendicular plane that assumes constant aircraft velocity. The resulting intersection from those three surfaces yields

a point in space that corresponds to the propeller efficiency for the respective flight regime. This scheme can be applied to calculate any other parameter registered in the file, like torque or RPM.

Aside from the propellers used in previous propulsion studies [54, 58] a few more were added to the MATLAB® routine. Although this study was not extensive, it allowed to select the 15" x 8" model, whose efficiency surpasses, in both climb and cruise, all other propellers considered. A comparison between propellers can be made by observing Table 4.6, where τ stands for torque and η for efficiency. It is remarked that all propellers have higher efficiency during cruise as a result of their reduced thrust production when compared with the climb situation. Since the 15" x 8" propeller is larger than all others it moves more air, needing less revolutions per minute to produce the same thrust. Seeing that at lower rotational speeds a larger propeller requires less power, the efficiency of the 15" x 8" prevails.

Propeller	12" x 6"		13" x 8"		14" x 7"		15" x 8"	
Stage	Cruise	Climb	Cruise	Climb	Cruise	Climb	Cruise	Climb
RPM	4595	8800	3663	7194	3599	6784	3104	5822
τ $(N.m)$	0.109	0.434	0.129	0.536	0.131	0.502	0.147	0.561
η	0.601	0.384	0.639	0.381	0.648	0.431	0.661	0.448

Table 4.6: Performance data of APC propellers for climb and cruise stages.

If overdimensioned, the propeller can increase the load put on the motor to the point where its reliability ends up severely compromised. For the propeller-motor set chosen in this project, Hyperion motors manufacturer provides test data [90] revealing that at 6270 RPM the selected motor (Hyperion ZS 3025-10) draws an electric current of 51.1 A. Knowing that climb occurs under normal conditions at 5822 RPM, the current is expected to drop near the motor's typical value of 45 A. That, added to a maximum current value of 65 A, admissible for 10 seconds, indicates that the motor's electric current stays within acceptable limits for a 10 min climb.

Attending that at the usual range of amperage the Hyperion motors operate with very high average efficiency, it is assumed in further calculations that motor efficiency remains the same throughout climb and cruise. Based on previous propulsion studies [55], a moderate efficiency value of 89% is attributed to the motor. All information regarding the propulsion subsystem efficiency is presented in Table 4.7, where the ESC, the battery and cables receive typical ratings.

	Battery	Cables	ESC	Motor	Propeller	**Total**
Cruise	100 %	100 %	95 %	89 %	66.1 %	55.9 %
Climb	100 %	100 %	95 %	89 %	44.8 %	37.9 %

Table 4.7: Propulsion sub-system overall efficiency for cruise and climb regimes.

The flowchart in Figure 4.21 sums up how propulsion and energy studies referring to climb are integrated in the design iterative process. Using thrust, velocity and efficiency computations described previously, the raw power required for climb was calculated and evaluated from distinct perspectives.

In the event of any flight predicament during climb, related to weather per example, the motor must be able to provide considerably more than enough power to surpass that stage. The maximum power
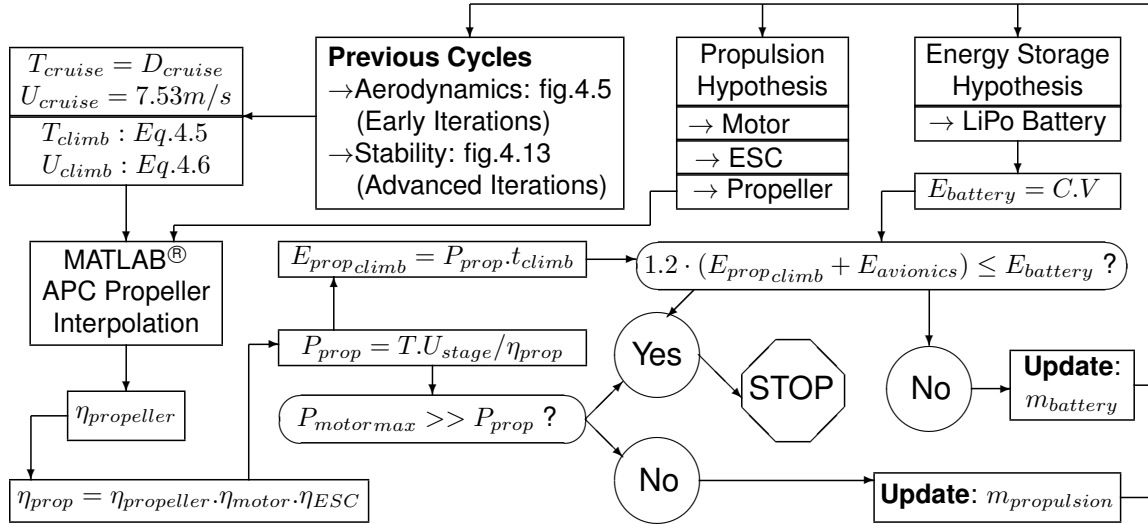
Figure 4.21: Propulsion and climb energy iterative flowchart.

provided by a motor, $P_{motor\,max}$, is given by the product of the motor's maximum electric current (I_{max}) and the voltage (V) applied in the battery. The selected motor was the Hyperion ZS 3025-10, shown in Figure 3.16a, because, together with a 3S LiPo battery, has a maximum power given by $P_{motor\,max} = I_{max} \cdot V = 65A \cdot 11.1V = 721.5W$, which clearly surpasses the climb propulsive power ($405W$). Modifying the initial assumption made for the motor component was not necessary, although the respective update has been schematized.

Besides power, the battery energy consumption is also critical when analyzing climb performance. As mentioned before, the solar energy received during climb is neglected. For safety reasons, it was imposed that the battery maximum storage exceeds the energy needed for the stipulated climb in at least 20%. It should be noted, in Figure 4.21, that the energy required by avionics, $E_{avionics}$, is also included. The communications power consumption is specified in Section 5.4 and the reason why it was decided to have a single battery setup for all on-board systems is discussed in Section 5.5.

The energy required to climb was calculated by integrating power consumption over time,

$$E_{climb} = \int_0^{t_{climb}} (P_{prop\,climb} + P_{avionics})dt = t_{climb} \cdot (P_{prop\,climb} + P_{avionics}). \tag{4.9}$$

From equation 4.9 comes that, for a climb time of 10 minutes, $E_{climb} = 68.39Wh$.

Since the effect that the number of battery discharge cycles has on the capacity is not accounted, the maximum energy contained within a battery was only calculated as the product between its capacity (C) and nominal voltage. It was verified that the initial energy storage assumption, a single 3S LiPo battery Hyperion G3 VX, with 4200 mAh capacity, does not contain enough energy because $E_{battery} = C.V = 4200[mAh] \cdot 11.1[V] = 46.62 < 68.39Wh$. Subsequently, the characteristics of the energy storage system were changed, Table 4.8 lists all battery sets evaluated. To prevent compatibility issues related with motor and ESC adapters this analysis focused solely on Hyperion battery models. The Hyperion G3 VX models are defined by a discharge rate of 35 C. The operating current of the battery, $I_{battery}$, given by the product of the discharge current with the capacity, surpasses the maximum current of the

motor for all cases in Table 4.8.

#	Cells	Voltage (V)	No.	Capacity (mAh)	$m_{battery}$ (g)	$E_{battery}$ (Wh)	E^* (KJ/Kg)	$\dfrac{E_{battery}}{E_{climb}}$
1	3S	11.1	1	6500	527	72.15	492.87	1.055
2	4S	14.8	1	5400	594	79.92	484.36	1.169
3	4S	14.8	1	6500	685	96.20	505.58	1.407
4	5S	18.5	1	5000	699	92.50	476.39	1.353
5	3S	11.1	2	8400 (2 x 4200)	702	93.24	486.47	1.363
6	3S	11.1	2	6600 (2 x 3300)	540	73.26	488.40	1.071

Table 4.8: Hyperion G3 VX battery sets evaluated in terms of climb energy.

The first approach to increase energy storage consisted in increasing the capacity of a single 3S LiPo battery to the maximum available, 6500 mAh. Looking at row 1 of Table 4.8, the resulting ratio $E_{battery}/E_{climb}$ does not obey 20% margin criteria defined in the scheme of Figure 4.21, therefore this option was discarded.

Then, it was observed that it was possible to harbor enough energy by having one battery with 4 or 5 cells. A 4S LiPo battery would need 6500 mAh capacity to respond to the climb requirement, while a 5S battery would require 5000 mAh. Notwithstanding, there were recognized system incompatibilities related to those batteries. For example, the power module, in figure 3.7, has a maximum input voltage of 18 V, which excludes 5S Lipo batteries. Furthermore, the most prominent eliminatory factor was the absence of MPPT models in the market that operate for the 4S and 5S voltage range.

The remaining option was to harbor two LiPo batteries connected in parallel in order to increase the resulting capacity. Having two 3S LiPo batteries with 4200 mAh each (totaling 8400 mAh) proved to satisfy the climb requirement, since $E_{battery}/E_{climb} = 1.363 > 1.2$, while avoiding complex modifications to the remaining on-board systems. In an attempt to reduce weight, two lower capacity battery (3300 mAh each) were also checked in the same way, but did not fulfill the required energy margin.

4.3.2 Propulsion Sub-system Summary

As implied in the beginning of Section 4.2, the set of iterations illustrated in Figure 4.21 emerged in two interleaved stages of the preliminary project. The first instance took place after the lift-weight equality loop of Figure 4.5 had been converged solely with wing updates, including airfoil and washout. Afterwards, the climb iterative study would resume with a higher volume of precedent iterations, covering cruise with solar energy (Chapter 5) and flight stability analysis.

Propeller	Motor: Hyperion ZS 3025-10				ESC: Groupner T70	
15" x 8"	Kv	I_{max}	$P_{maxlimit}$	P_{max}	I_{max}	V_{max}
	775 RPM/V	65 A	1150 W	721.5 W	70 A	25 V
Energy Storage System (LiPo)						
No. batteries	Model	$V_{nominal}$	Capacity	$I_{battery_{max}}$	Discharge Rate	
2	Hyperion G3 VX 3S	11.1 V	2 x 4200 mAh	147 A	35 C	

Table 4.9: Propulsion sub-system data.

Table 4.9 summarizes the characteristics of the resulting main propulsive components. The motor, the battery model, the propeller and the ESC are illustrated in Figures 3.16a, 3.16b, 3.16c and 3.16d, respectively.

4.3.3 Maximum Performance Regime

While the velocity of cruise has been fixed so that the UAV can cover a minimum radius of action within the stipulated time, the whole range of possible speeds appears only as a consequence of the design iterative procedure. Notedly, the maximum velocity under steady flight conditions has been calculated equaling thrust to drag and solving for U_{max}, which resulted in [91]:

$$U_{max} = \sqrt{\frac{(T/W)_{max} \cdot (W/S) + (W/S) \cdot \sqrt{(T/W)_{max}^2 - 1/(L/D)_{max}^2}}{\rho \cdot C_{D,0}}} \tag{4.10}$$

where $C_{D,0}$ is the zero lift drag coefficient, that was extrapolated from the drag polar in Figure 4.10b. Along with the maximum velocity, the thrust over weight ratio, $(T/W)_{max}$, was determined using propeller performance data. Recurring to the same file used to study propeller efficiency, shaft power can also be used to represent possible flight regime variations, as seen in Figure 4.22, which refers to the chosen 15'x8' propeller.
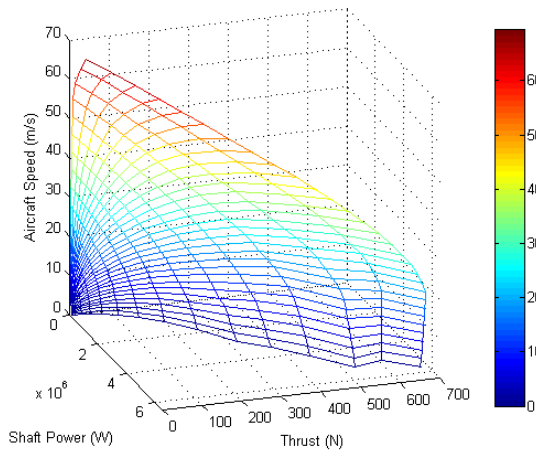
Figure 4.22: Aircraft speed as function of thrust and shaft power applied to 15"x8" APC propeller.
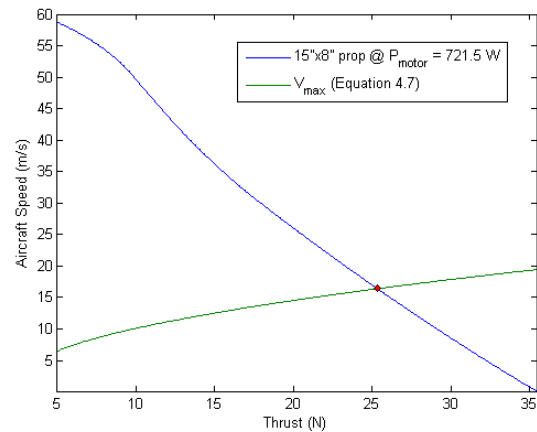
Figure 4.23: Graphical calculation of U_{max} and T_{max}.

Knowing the motor's maximum electric power and efficiency, a single 2D function relating aircraft velocity with thrust at maximum power is obtained by intersecting the surface in Figure 4.22 with the respective constant shaft power plane. Ultimately, the maximum performance regime is calculated by solving graphically a linear system featuring Equation (4.10) and the function obtained from the propeller's performance at maximum power. From Figure 4.23, comes a thrust over weight ratio of 0.43, associated with a maximum project velocity of 16.39 m/s, corresponding to 59 km/h.

4.4 Flight Envelope

So far in the UAV performance analysis, only rectilinear motion with constant velocity was considered. Assuming steady flight conditions, it was assured, by undergoing the iterative loop in Figure 4.5, that during cruise the load factor, defined as the ratio between lift and weight, equals one. However, to accomplish the mission safely, the aircraft structure must be able to withstand additional load sources; such as flight maneuvers and unforeseeable gusts. The operational framework in relation to air speed and load factor defines the limits for a balanced detailed design of internal structures.

Structural specifications concerning general aviation aircraft can be found in Federal Aviation Regulations (FAR) Part 23 [92], where a maximum load factor no larger than 3.8 is imposed. Moreover, according to Raymer [93] the characteristic values for the same type of aircraft lie between 2.5 and 3.8. Although this data refers to general commercial aircraft, when compared with a light-weight UAV project resemblances regarding low maneuverability requirements are recognizable.

Attending to the facts aforementioned, along with the need to spare airframe weight, a maximum load factor, n_{max}, of 2.5 was selected as an achievable mark. Load factor is usually positive, but in some instances it may become negative. With the sort of flight for which the LEEUAV is designed, downward gusts are the scenario most likely to cause a negative load factor. FAR standards also state that for normal utility aircraft the absolute value of the negative load factor must not be less than 0.4 times its positive counterpart. Thus in this project the minimum load factor, n_{min}, assumed a value of -1. The current choice for the load factor upper and lower bounds is also supported by an available flight envelope of small UAVs with a resembling size, weight and maneuverability [94].

Stall is also imposed as an aerodynamic limit on load factor, it obeys the known expression 4.11 that covers both positive and negative stall curves. Seeing how close the cruise velocity is to the stall speed in this specific project, the most suited reference to estimate the maximum velocity the airplane's structure can endure without destructive phenomena was found in [95]. It states that the dive velocity must be higher than the level flight maximum cruise speed, U_{max}, by at least a factor of 1.2 .

$$n_{stall} = \pm \frac{1}{2} \cdot \rho \cdot U^2 \cdot C_{Lmax} \cdot \frac{W}{S} \qquad (4.11) \qquad\qquad U_D = 1.2 \cdot U_{max} \qquad (4.12)$$

With the most conservative assumption in mind, the dive speed was calculated from Equation (4.12), where U_{max} is already known from Section 4.3.3. It is important to remark that it is possible to surpass U_{max} in flight, when encountering tailwind or during descent, per instance.

Figure 4.24 displays a V-n diagram, which represents flight maneuverability load factors as a function of airspeed, at cruise ceiling altitude. It is observed that the load factor is not allowed to increase indefinitely because it is constrained by horizontal lines denoting structural strength limits, n_{max} and n_{min}. In the regions not surrounded by stall curves but within load factor limits, although structural failure does not take place, continuous flight is not possible since C_{Lmax} cannot be surpassed. Retracing the project requirement in Section 2.1, in terms of maneuverability it was only imposed a maximum bank angle for the aircraft's turn of 45º. Such angle is associated with a load factor of 1.414, which can only occur without stall for velocities superior to 7.6 m/s.

60
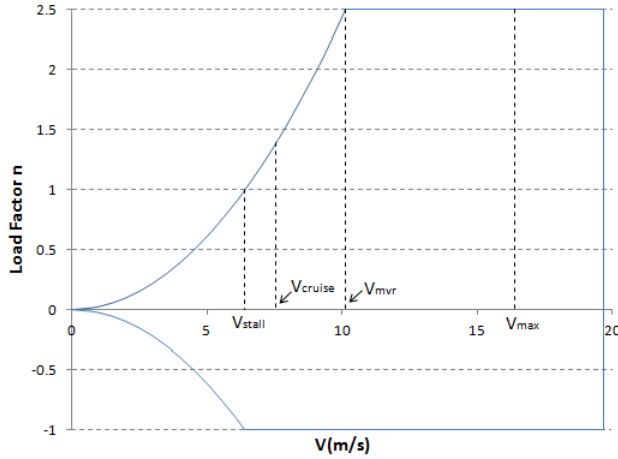
		$n+$	$n-$
U_s	6.39	1	-1
U_{Cruise}	7.53	1.39	-1
U_{Climb}	7.67	1.44	-1
U_{mvr}	10.11	2.5	-1
U_{max}	16.39	2.5	-1
U_D	19.67	2.5	-1

Table 4.10: Maneuver envelope specifications (velocity in m/s).

Figure 4.24: Maneuver V-n diagram of the LEEUAV (h=1300 m).

The maneuvering speed, U_{mvr} , occurs at the point where both lift coefficient and load factor are simultaneously at their highest possible values. At velocities lower than U_{mvr} the bank angle may not be high enough for a tight turn, in contrast, at higher velocities maneuverability decreases. In other words, the maximum load factor at maneuvering speed allows the aircraft to perform the turn with minimum radius at maximum angular velocity.

Seeing that atmosphere is a dynamic system, gusts are expected to occur during most high altitude flights. When an gust occurs, the aircraft experiences an instantaneous change in angle of attack, leading to a sudden change in lift, thus in the load factor as well. Assuming that the airplane is subjected only to symmetrical vertical gusts in level flight, the gust envelope can be determined in a similar pattern to the maneuvering envelope, except that the boundaries are determined by the gust incremental load factor added in equation 4.13.

$$n_{gust} = \frac{L \pm \triangle L}{W} = 1 \pm \frac{\rho u U C_{L\alpha}}{2W/S} \tag{4.13}$$

The normal component of the gust velocity (u) can be calculated as the product of the overall gust velocity ($\hat{u}$) and the response coefficient (K), $u = K\hat{u}$. For subsonic flight, the response coefficient is given by $K = \frac{0.88 \cdot \mu}{5.3 + \mu}$, where μ is a dimensionless equivalent mass ratio defined as $\mu = \frac{2 \cdot W/S}{\rho g \bar{c} U C_{L\alpha}}$ [88].

Usually, the overall gust velocity, $\hat{u}$, presented on the flight envelope is taken from statistical flight data on standards, where its value is specified for a given altitude range and flight condition. However, given the light-weight airframe of this particular project, it was considered more relevant to extract, by reverse engineering, the maximum gust velocity at which structural load factor limits, n_{max} and n_{min}, are not overridden.

Once the maneuvering and gust envelopes were determined, the combined flight envelope in Figure 4.25 was drawn. Two main additional scenarios are presented, at the dive speed the aircraft structure cannot withstand gusts that surpass 2.58 m/s, nevertheless, if velocity does not surpass the maneuvering speed the admissible gust raises to 5.02 m/s. This sort of information will be particularly useful when analyzing weather forecasts prior to the mission date to decide whether the LEEUAV should fly or not.
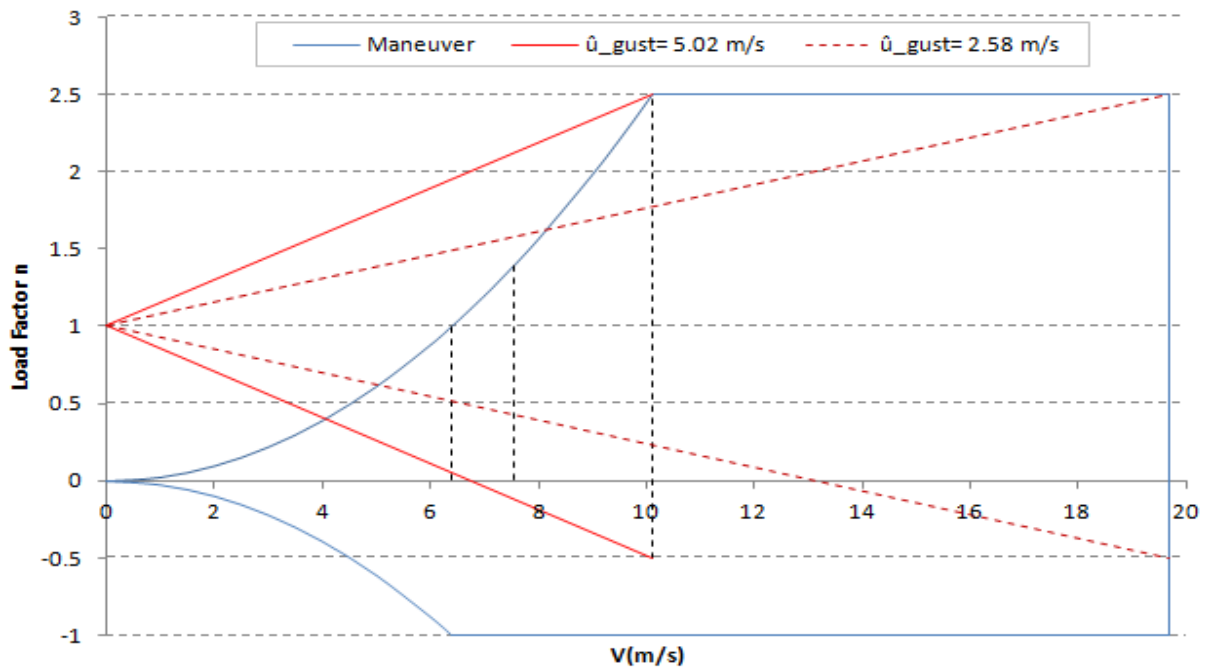
Figure 4.25: Combined V-n diagram of the LEEUAV (h=1300 m).

Adding the effect of flap deflection to the envelope would raise the load factor at lower speeds, due to the increase in C_{Lmax}. That detail was not added since it is not critical to what concerns the true limit loads the airplane's structure will experience.

4.5 Design Point

The design point of an aircraft is usually given by its wing loading and an ascertained value of thrust to weight ratio or power to weight ratio. In this work, it is intended to indicate the working condition at which the motor can be adapted to its use in the UAV to match the endurance requirement. Therefore, cruise was chosen as the representative situation of the design point.

Due to the iteration procedures described in previous sections it was possible to limit the performance according to climb and cruise power requirements, as seen in Table 4.11.

W/S (N/m²)	(T/W)$_{climb}$	(P/W)$_{climb}$ (Watt /N)	(T/W)$_{cruise}$	(P/W)$_{cruise}$ (Watt /N)
35.26	0.34	6.96	0.07	1.04

Table 4.11: Performance specifications.

Observing the difference in power between stages, it is evident that the mission profile includes non-consistent requirements in terms of energy. The representative design point does not allow the LEEUAV to fulfill climb requirements, thereupon the climb performance specifications have been defined as an off-design switch point.

The final overall dimensions of the converged aircraft are presented in Table 4.12 and Figure 4.26. In comparison with the provisory solution presented at the end of Chapter 3, the fuselage length increased

in about 10 cm and the position of the wing with respect to the tail changed in virtue of stability studies. Upstream the wing, the fuselage was resized to harbor all components, including the RPV camera upfront. Furthermore, the wingspan of the tip portions without panels was slightly reduced in order to add some room tolerance in the center, between solar arrays, which is meant to help assure a stiff junction between the wing and the fuselage. The ailerons and ruddervators were not drawn since their conceiving involves assembly solutions not addressed at this stage of the project.

	b (m)	c_{root} (m)	c_{tip} (m)	MAC (m)	Area (m^2)	AR	Dihedral (º)
Wing	5	0.35	0.252	0.334	1.67	14.95	1
V-tail	1.04	0.306	0.204	0.26	0.26	3.95	32.71

Fuselage Length (m)	1.980

Table 4.12: Airframe dimensions.

To comply with the surveillance window of eight hours, the crucial restraint is whether it is possible to maintain the needed cruise power over weight ratio. Patently, the design point is highly influenced by the solar energy collection sub-system, whose performance description has been over-leaped in the document. Chapter 5 explains thoroughly how the present arrangement of solar panels reliably responds to the endurance requirement.
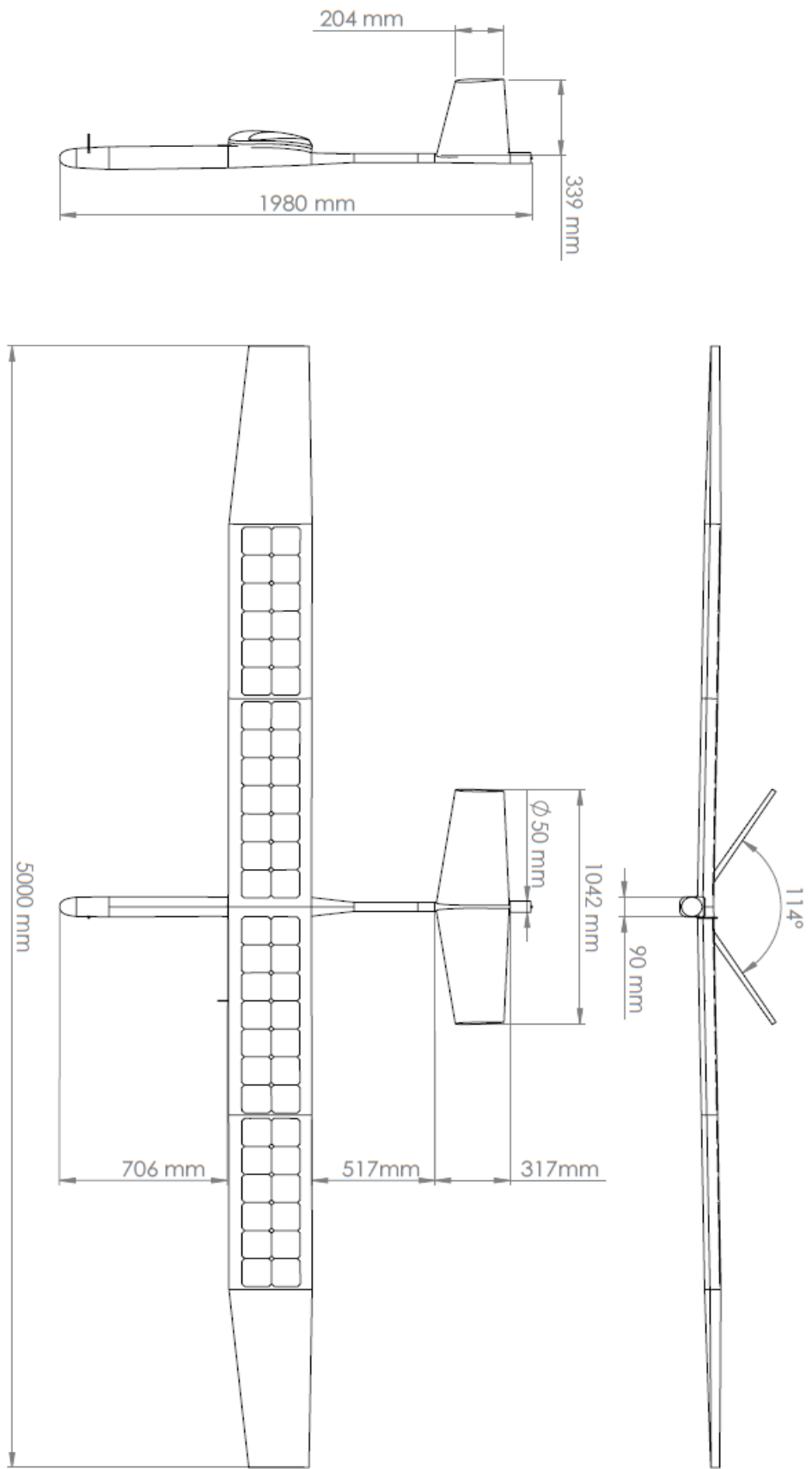
Figure 4.26: Three view drawing of the LEEUAV (dimensions in mm).

Chapter 5

Solar Energy Management

5.1 Solar Energy Sub-System

Likewise in the propulsion sub-system, to run computations concerning the solar energy collection sub-system, the efficiency of its components had to be addressed beforehand. Energy transfer from the solar array to the batteries relies on the current MPPT, Genasun's GV-10 Lithium model, that has been tested in a simple setup described in [54], rating an average efficiency of 88.84%. Since the introduction of the measuring circuits in that experiment may have slightly shortened the result, it was decided to settle with the minimum efficiency reported by manufacturers, 92%.
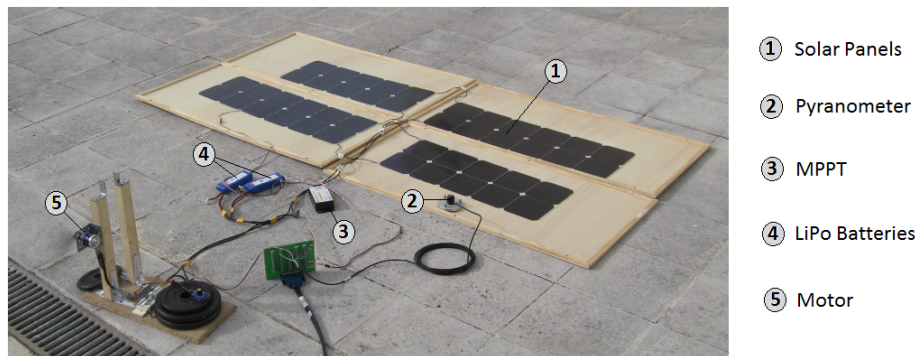
Figure 5.1: Hybrid propulsion system assembly in mission simulation [54].

Recalling Section 3.2.3, it is known that the selected PV cells SunPower C60 have a maximum efficiency of 22.6%. Additionally, that value has been measured in a controlled environment at a room temperature of 25°C. To ascertain more realistic values, a full mission propulsive simulation was run statically in [54], with the flight regime calculated for the first generation LEEUAV. As seen in Figure 5.5, the assembly setup included the previous solar array arrangement and a pyranometer near to measure irradiation values. During a time window of 6 hours and 47 minutes, the simulation confirmed that the PV cells efficiency decreases with higher surface temperatures. The average energy collection sub-system efficiency rated 16.22% at an average solar array temperature of 35.1°C. Assuming the MPPT efficiency considered in this chapter, it yields a solar array efficiency of approximately 17.6%.

There are, however, relevant differences between the simulation and the mission scenario that may

affect the PV cells efficiency. This test was performed in Instituto Superior Técnico, Lisbon, at an altitude of 88 m in relation to sea level, while the mission takes place at higher altitudes, where the ambient temperatures are lower. Moreover, the solar panels surface is going to be under the effects of forced convection, subjected to a thermal boundary layer that will contribute to decrease surface temperature. For those reasons, the PV arrays efficiency was estimated with a moderate value of 20%.

Another fact not accounted during the mission simulation is that the solar cells follow a cambered airfoil. In a series of interconnected cells, the ones with the lowest irradiance limits the current for all the others. According to [37], the cells closer to the leading edge, which have the smallest elevation angle, will penalize the other cells. This occurs mainly at sunrise or sunset, when the sun elevation is low, and depends also on the airplane orientation. An efficiency factor of 90% related to the panels camber was added to cope with this effect. Table 5.1 displays the overall efficiency of the energy collection subsystem along with all factors applied.

Solar Arrays (η_{panels})	Panels Camber (η_{camber})	MPPT (η_{MPPT})	**Total** (η_{energy})
20 %	90 %	92 %	16.7 %

Table 5.1: Energy collection sub-system overall efficiency.

5.2 Daily Irradiation Model

The solar power supplied by the PV arrays will also depend on the incident irradiation, varying with a wide range of unpredictable factors related to meteorological conditions and atmosphere properties. Conversely, it was possible to determine solar radiation profiles for each day of the year in a given location. The calculation methodology applied is explained in detail in the present section, whose content is taken almost entirely from [96].

It is noted that the implemented model has not been prepared to cover irradiation values obtained from extended travel routes, in which location changes on the map over time. For a matter of simplicity, all the results shown refer to the geographical coordinates of an unique location, Pampilhosa da Serra, that already served as reference to decide the project cruise altitude of 1300 m.

5.2.1 Interaction of Solar Radiation with the Earth

The term irradiance is used to consider the solar power (instantaneous energy) falling per unit of area $[W/m^2]$, while the term irradiation is used to consider the amount of solar energy falling on unit area over a stated time interval $[Wh/m^2]$. The same symbols are used for irradiance and irradiation but the two concepts can be differentiated by context or by attached units.

The interaction of solar radiation with the earth's atmosphere and surface is determined by three group of factors:

1. The Earth's geometry, revolution and rotation (declination, latitude, solar hour angle);

2. Terrain (elevation, surface inclination and orientation, shadows);

3. Atmospheric attenuation (scattering, absorption) by:

   (a) gases (air molecules, ozone, CO_2 and O_2);

   (b) solid and liquid particles (aerosols, including non-condensed water);

   (c) clouds (condensed water).

The first group of factors determines the available extraterrestrial radiation based on solar position above horizon and can be precisely calculated using astronomic formulas.

Modeling the terrain's topography is not required since airplanes travel in mid air. Instead, in order to determine the attenuation of radiation by the thickness of the atmosphere, only the aircraft's altitude above sea level needed to be accounted.

Extraterrestrial solar radiation traversing through the earth's atmosphere is attenuated by various atmospheric constituents, namely gases, liquids, solid particles and clouds. Attending to its dynamic nature and complex interactions, the atmospheric attenuation can only be modeled at a certain level of accuracy that decreases from factors 1 to 3.

The attenuation by gas constituents (factor 3.a) describes clear and dry (Rayleigh) atmosphere and is given by its relative optical air mass and optical thickness (m_{opt} and $d_r(m_{opt})$ respectively).

The attenuation by solid and liquid particles (factor 3.b) is described by the Linke turbidity (T_{LK}). It indicates the optical density of hazy and humid temperatures in relation to a clean and dry atmosphere.

Clouds (factor 3.c) are the strongest attenuates. Theoretical analysis of the attenuation of solar radiation through clouds requires great deal of information regarding instantaneous thickness, position and number of layers of clouds, as well as their optical properties. For that reason, in this thesis only sample statistic data is used to estimate the influence of cloud covers. This process is described with more detail in Section 5.2.2.3.

Maximum insolation is obtained when skies are absolutely clean and dry and relatively less radiation is received when aerosols are present. Omitting the clouds attenuation factor (factor 3.c) leads to clear-sky radiation values.

5.2.2 Solar Radiation Model *r.sun* MATLAB® Implementation

A theoretical model that computes both Clear-sky and Real-sky radiation for a given location on Earth has been developed using MATLAB® scripting language. The coding algorithms applied in MATLAB® are based on the r.sun model implemented in the GRASS GIS freeware open source environment using the C programming language [96], hence the designation *r.sun* MATLAB® Implementation. The theoretical groundwork used to obtain global irradiance profiles within a given day are explained in the following Subsections.

5.2.2.1 Position of the Sun

It is considered, throughout all calculations in this annex, that the wing's upper surface can be approximated as an horizontal surface with respect to the sun's position. Keeping this assumption in mind, the position of the sun is simply given by two co-ordinates, the solar altitude h_0(an angle between the Sun path and a horizontal surface), and solar azimuth A_0 (horizontal angle between the Sun and meridian - measured from East).

Since inclined surfaces won't be addressed, calculating the solar altitude will suffice, it is gauged as

$$sin\, h_0 = C_{31} \cdot cos\, T_H + C_{33} \tag{5.1}$$

where

$$C_{31} = cos\, \psi \cdot cos\, \delta,$$
$$C_{33} = sin\, \psi \cdot sin\, \delta. \tag{5.2}$$

Knowing the coordinates of the aircraft, the latitude ψ can be inserted. As for the sun declination δ [rad], it is computed according to [96]

$$\delta = arcsin(0.3978 \cdot sin(j' - 1.4 + 0.0355 \cdot sin(j' - 0.0489))), \tag{5.3}$$

with the day angle j' in radians as

$$j' = 2 \cdot \pi \cdot j/365.25, \tag{5.4}$$

being j the day number which varies from 1 on January 1st to 365 (366) on December 31st.

The hour angle T_H [rad] is calculated from the local solar time t expressed in decimal hours on the 24 hour clock as

$$T_H = 0.261799 \cdot (t - 12) \tag{5.5}$$

5.2.2.2 Computing Clear-sky Radiation

Radiation, selectively attenuated by the atmosphere, which is not reflected or scattered and reaches the surface directly is named beam radiation. On the other hand, scattered radiation that reaches the surface is called diffuse radiation. There is also a small part of radiation reflected from the ground that is not considered because the solar panels don't point towards the ground.

The clear-sky global irradiance of the considered horizontal surface is then solely given as a sum of its beam and diffuse component,

$$G_{hc} = B_{hc} + D_{hc}. \tag{5.6}$$

Beam radiation

Outside the atmosphere, at the mean solar distance, the beam irradiance, also known as the solar constant (I_0), is 1367 $W.m^2$. The Earth's orbit is lightly eccentric and the Sun-Earth distance varies slightly across the year. Therefore, a correction factor e, to allow for the varying solar distance, is applied

in calculation of the extraterrestrial irradiance G_0 normal to the solar beam as

$$G_0 = I_0 \cdot e, \tag{5.7}$$

where

$$e = 1 + 0.03344 \cdot cos(j' - 0.048869). \tag{5.8}$$

The calculation of day angle j' is explained in Equation (5.4).

The beam irradiance normal to the solar beam, B_{0c}, is then attenuated by the cloudless atmosphere, and calculated as

$$B_{0c} = G_0 \cdot exp(-0.8662 \cdot T_{LK} \cdot m_{opt} \cdot d_R(m)). \tag{5.9}$$

Kasten [97] has provided the following guideline for typical values of T_{LK} in Europe.

Air Features	Very clean cold air	Clean warm air	Moist warm or stagnating air	Polluted air
T_{LK}	2	3	4-6	>6

Table 5.2: Typical values of Linke turbidity in Europe.

The parameter m_{opt} in Equation (5.9) is the relative optical air mass, calculated using

$$m_{opt} = (p/p_0)/(sin\, h_0{}^{ref} + 0.50572 \cdot (h_0{}^{ref} + 6.07995) - 1.6364), \tag{5.10}$$

where $h_0{}^{ref}$ is the solar altitude h_0 (in degrees) corrected by the atmospheric refraction component $Dh_0{}^{ref}$ using

$$Dh_0{}^{ref} = 0.061359 \cdot (0.1594 + 1.123 \cdot h_0 + 0.065656 \cdot h_0{}^2)/(1 + 28.9344 \cdot h_0 + 277.3971 \cdot h_0{}^2), \tag{5.11}$$

with

$$h_0{}^{ref} = h_0 + Dh_0{}^{ref} \tag{5.12}$$

The p/p_0 component in Equation 5.10 is the correction for a given elevation z given by

$$p/p_0 = exp(-z/8434.5) \tag{5.13}$$

The parameter d_R in Equation (5.9) is the Rayleigh optical thickness at air mass m and is calculated according to the improved formula [97] as follows:

$$d_R(m_{opt}) = \begin{cases} 1/(6.6296 + 1.7513 \cdot m_{opt} - 0.1202 \cdot m_{opt}{}^2 + 0.0065 \cdot m_{opt}{}^3 - 0.00013 \cdot m_{opt}{}^4), & \text{if } m_{opt} \leq 20 \\ 1/(10.4 + 0.718 \cdot m_{opt}), & \text{if } m_{opt} > 20 \end{cases} \tag{5.14}$$

The beam irradiance on a horizontal surface B_{hc} is then calculated as

$$B_{hc} = B_{0c} \cdot \sin h_0 \tag{5.15}$$

Diffuse radiation

As the cloudless sky becomes more turbid, the diffuse irradiance increases while the beam irradiance decreases. The estimation of the diffuse component on an horizontal surface D_{hc} is made as a product of the normal extraterrestrial irradiance G_0, a diffuse transmission function T_n dependent only on the Linke turbidity factor T_{LK}, and a diffuse solar altitude function F_d dependent only on the solar altitude h_0:

$$D_{hc} = G_0 \cdot T_n(T_{LK}) \cdot F_d(h_0) \tag{5.16}$$

The estimate of the transmission function $T_n(T_{LK})$ gives a theoretical diffuse irradiance on a horizontal surface with the Sun vertically overhead for the air mass 2 Linke turbidity factor. The following second order polynomial expression is used:

$$T_n(T_{LK}) = -0.015843 + 0.030543 \cdot T_{LK} + 0.0003797 \cdot TLK^2. \tag{5.17}$$

The solar altitude function is evaluated using

$$F_d(h_0) = A_1 + A_2 \cdot \sin h_0 + A_3 \cdot \sin^2 h_0, \tag{5.18}$$

where the values of the coefficients A_1, A_2 and A_3 depend on the Linke turbidity T_{LK} as

$$A_1' = 0.26463 - 0.061581 \cdot T_{LK} + 0.0031408 \cdot {T_{LK}}^2$$
$$A_1 = \begin{cases} 0.0022/T_n(T_{LK}), & \text{if } A_1' \cdot T_n(T_{LK}) < 0.0022 \\ A_1', & \text{if } A_1' \cdot T_n(T_{LK}) \geq 0.0022 \end{cases} \tag{5.19}$$

$$A_2 = 2.04020 + 0.018945 \cdot T_{LK} - 0.011161 \cdot {T_{LK}}^2 \tag{5.20}$$

$$A_3 = -1.3025 + 0.039231 \cdot T_{LK} + 0.0085079 \cdot {T_{LK}}^2 \tag{5.21}$$

5.2.2.3 Computing Real-sky Radiation

For the assessment of global irradiance/irradiation on a horizontal surface under overcast conditions G_h, the clear-sky values G_{hc} are multiplied by clear-sky index k_c:

$$G_h = G_{hc} \cdot k_c. \tag{5.22}$$

The index k_c represents the atmospheric transmission expressed as a ratio between horizontal global radiation under overcast and clear-sky conditions. For a set of ground meteorological stations the clear sky index can be calculated from measured global radiation G_{hs} and computed values of clear-sky global

radiation G_{hc} as

$$k_c = G_{hs}/G_{hc}. \tag{5.23}$$

The values of measured global radiation, G_{hs}, have been determined by using the SoDa online service [98], which is a broker to a list of webservices that provide historic solar radiation data. The sample of global irradiance used in this work corresponds to roughly 16800 satellite measurements , per location (latitude, longitude and altitude), in every hour between the years of 2004 and 2005.

Monthly hour index values, $k_{c\,(hour,\,month)}$, were calculated for each hour of the day as the average of all measurements made at that precise hour during that month, this is

$$k_{c\,(hour,\,month)} = \frac{\sum\limits_{i=1}^{no.\,days} G_{hs\,hour} \Big/ \sum\limits_{i=1}^{no.\,days} G_{hc\,hour}}{no.\,days} \tag{5.24}$$

Where the clear sky component, $\sum\limits_{i=1}^{no.\,days} G_{hc\,hour}$, is obtained by performing the computations described in Subsections 5.2.2.1 and 5.2.2.2 for all hours considered. For each geographic position, the values of $k_{c\,(hour,\,month)}$ were assembled on a 24x12 matrix, where rows correspond to hours of the day and columns to months of the year.

$$
\begin{bmatrix}
0 & 0 & 0 & 0 & 0 & 0 & 0 & 0 & 0 & 0 & 0 & 0 \\
0 & 0 & 0 & 0 & 0 & 0 & 0 & 0 & 0 & 0 & 0 & 0 \\
0 & 0 & 0 & 0 & 0 & 0 & 0 & 0 & 0 & 0 & 0 & 0 \\
0 & 0 & 0 & 0 & 0 & 0 & 0 & 0 & 0 & 0 & 0 & 0 \\
0 & 0 & 0 & 0 & 0 & 0 & 0 & 0 & 0 & 0 & 0 & 0 \\
0 & 0 & 0 & 0.0086 & 0.0871 & 0.1329 & 0.0793 & 0.0128 & 0 & 0 & 0 & 0 \\
0 & 0 & 0.0206 & 0.191 & 0.3466 & 0.4073 & 0.3479 & 0.1876 & 0.1183 & 0.0247 & 0 & 0 \\
0.0037 & 0.0532 & 0.2212 & 0.4497 & 0.5332 & 0.5983 & 0.5735 & 0.3845 & 0.4249 & 0.2563 & 0.1132 & 0.0104 \\
0.2147 & 0.3133 & 0.4486 & 0.5924 & 0.6399 & 0.7022 & 0.6899 & 0.4989 & 0.6245 & 0.4667 & 0.3963 & 0.2416 \\
0.5004 & 0.5369 & 0.5812 & 0.6563 & 0.678 & 0.7601 & 0.7578 & 0.5579 & 0.7222 & 0.57 & 0.5835 & 0.5053 \\
0.6824 & 0.6617 & 0.6593 & 0.7012 & 0.7178 & 0.8122 & 0.8159 & 0.6063 & 0.7905 & 0.6173 & 0.6735 & 0.665 \\
0.8088 & 0.7719 & 0.7403 & 0.7389 & 0.7358 & 0.849 & 0.8592 & 0.6528 & 0.8387 & 0.6495 & 0.7166 & 0.7733 \\
0.936 & 0.8464 & 0.8014 & 0.7836 & 0.7376 & 0.8969 & 0.9076 & 0.6899 & 0.8852 & 0.7049 & 0.791 & 0.8596 \\
1.1001 & 0.9664 & 0.8782 & 0.8152 & 0.8033 & 0.9326 & 0.9669 & 0.7327 & 0.9685 & 0.7318 & 0.8772 & 1.0111 \\
1.3708 & 1.1902 & 0.968 & 0.8768 & 0.9047 & 1.02 & 1.0423 & 0.7978 & 1.0738 & 0.852 & 1.014 & 1.2572 \\
2.3458 & 1.7363 & 1.2525 & 1.062 & 1.0132 & 1.1503 & 1.1629 & 0.9267 & 1.2517 & 1.0814 & 1.4364 & 2.2444 \\
24.177 & 6.7838 & 2.0735 & 1.386 & 1.225 & 1.3443 & 1.3974 & 1.1629 & 1.6876 & 2.018 & 16.3047 & 0 \\
0 & 0 & 75.364 & 2.8585 & 1.6854 & 1.7279 & 1.9144 & 1.8342 & 13.6956 & 0 & 0 & 0 \\
0 & 0 & 0 & 9.8231 & 12.6011 & 3.7312 & 5.741 & 46.1439 & 0 & 0 & 0 & 0 \\
0 & 0 & 0 & 0 & 0 & 0 & 0 & 0 & 0 & 0 & 0 & 0 \\
0 & 0 & 0 & 0 & 0 & 0 & 0 & 0 & 0 & 0 & 0 & 0 \\
0 & 0 & 0 & 0 & 0 & 0 & 0 & 0 & 0 & 0 & 0 & 0 \\
0 & 0 & 0 & 0 & 0 & 0 & 0 & 0 & 0 & 0 & 0 & 0 \\
0 & 0 & 0 & 0 & 0 & 0 & 0 & 0 & 0 & 0 & 0 & 0
\end{bmatrix}
$$

Figure 5.2: Monthly hour index value matrix in Pampilhosa da Serra (h=1300 m).

Figure 5.2 displays the matrix with monthly hour index values ($k_{c\,(hour,\,month)}$) in Pampilhosa da Serra, one of the targeted locations on table A.1, for an horizontal surface at an altitude of 1300 m.

The computation procedure continues by, given the month of the chosen day, selecting a certain

column vector in Figure 5.2 (third column corresponds to March, per example) that gets multiplied by a row vector with clear-sky global irradiance components for each hour of that day. The result will bring a vector with values of global irradiance in each hour of that day.

$$\begin{bmatrix} k_{c\,(1\,,\,month)} \\ ... \\ k_{c\,(12\,,\,month)} \\ ... \\ k_{c\,24\,,\,month)} \end{bmatrix} \cdot \begin{bmatrix} G_{hc\,(1\,,\,day)} & ... & G_{hc\,(12\,,\,day)} & ... & G_{hc\,24\,,\,day)} \end{bmatrix} = \begin{bmatrix} G_{h\,(1\,,\,day)} \\ ... \\ G_{h\,(12\,,\,day)} \\ ... \\ G_{h\,(24\,,\,day)} \end{bmatrix} \qquad (5.25)$$

With the resultant vector from Equation (5.25), the daily irradiance distribution is obtained by performing shape-preserving piecewise cubic interpolations between values hourly. Figure 5.3 illustrates distinct graphic plots of daily irradiance distributions coinciding with each astronomical season interval in Pampilhosa da Serra.
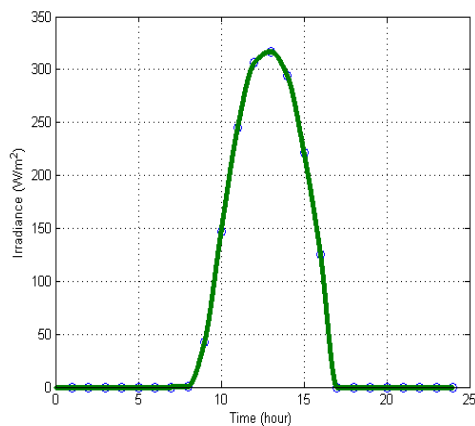
(a) December solstice.
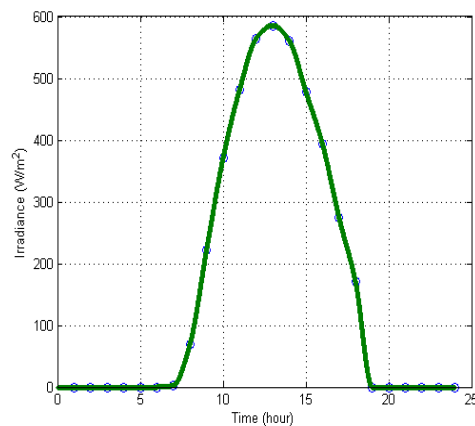
(b) March equinox.
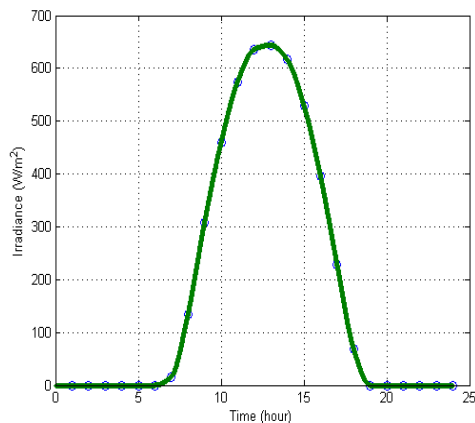
(c) September equinox
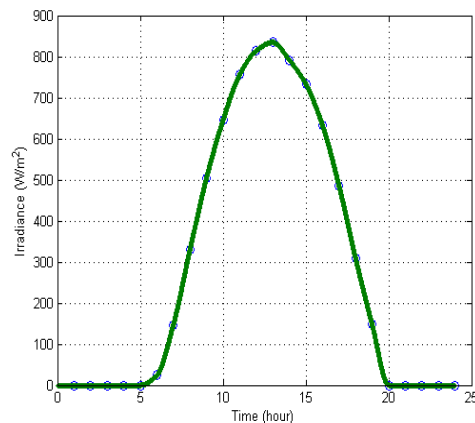
(d) June solstice

Figure 5.3: Daily Irradiance distribution between seasons in Pampilhosa da Serra (h=1300 m).

5.3 Energy and Power Management

By applying the overall efficiency of the solar energy collection system, η_{energy}, to the irradiance profile the solar power harnessed through solar panels area, W_{solar}, was obtained. Thereafter, knowing the battery energy at the beginning of cruise, $E_{battery}$, and the power consumption, P_{cruise}, flight endurance could be computed as explained in Section 5.3.1. The flowchart of Figure 5.4 illustrates how solar energy calculations have been integrated on the iterative design process. It is remarked that the power consumption considered during cruise corresponds to the sum between the propulsion and communications systems consumptions, that is $P_{cruise} = P_{prop_{cruise}} + P_{avionics}$. Section 5.5 discusses the reasons for a single battery setup for all on-board systems.
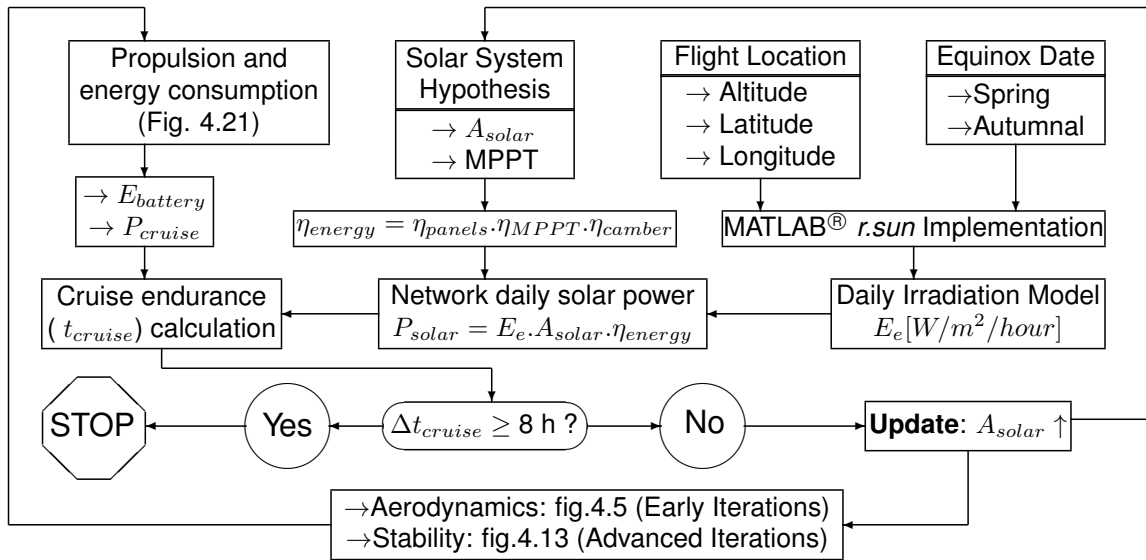
Figure 5.4: Cruise energy management iterative flowchart.

Both spring and autumnal equinox dates were inserted in the loop and since it is not specified for which one the endurance requirement must be fulfilled, the design is considered converged if cruise endurance Δt_{cruise} surpasses the 8 hour mark in at least one of them. In the advent of not being able to accomplish the endurance requirement, the airplane design would have to be completely reiterated in order to increase the wing area available for solar panels, A_{solar}. Fortuitously, the solar energy management loop satisfied the endurance imposition at the first attempt. The resulting setup of the energy collection subsystem is listed in table 5.3 and illustrated by figure 5.5 that displays the updated solar arrays layout. It is noted that there will be two 2x7 PV arrays in the center piece of the wing and a 2x6 PV array in each lateral part of the wing, as seen in Figure 4.26. The chosen SunPower C60 panel array and the GV-10 Lithium MPPT are illustrated in Figures 3.15a and 3.15b, respectively.

Photovoltaic arrays layout			MPPT	
Model	A_{solar}= 0.0798 m^2 (52 panels)		GV-10 Lithium	
SunPower	Wing center (28 panels)	Wing laterals (2 x 12 panels)	$P_{max\,limit}$	$V_{nominal}$
C60	A = 0.430 m^2	A = 0.0.368 m^2	140 W	12 V

Table 5.3: Energy collection sub-system setup.
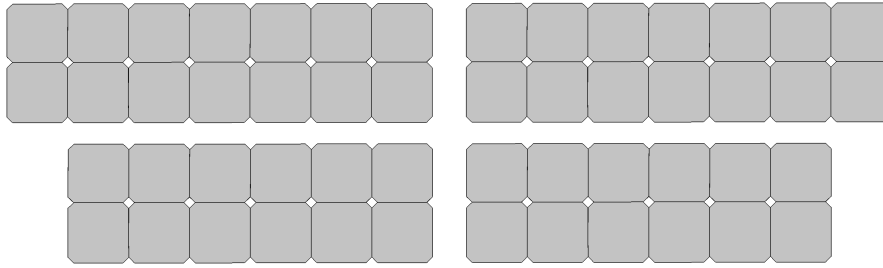
Figure 5.5: Photovoltaic arrays layout.

5.3.1 Standard Mission Profile

To study all energy management scenarios that may occur during a daily mission at any given time of the year, delimiting dates of all northern meteorological seasons have been examined. Figure 5.6 presents the daily solar net power available in all season intervals plotted in MATLAB® against the power required to cruise. The gap observed between the peak values of solar power and the climb power of 410.3 W confirms the need for fully charged battery system at the beginning of the mission. Again, it is reminded that in this analysis the solar energy received during climb is neglected.
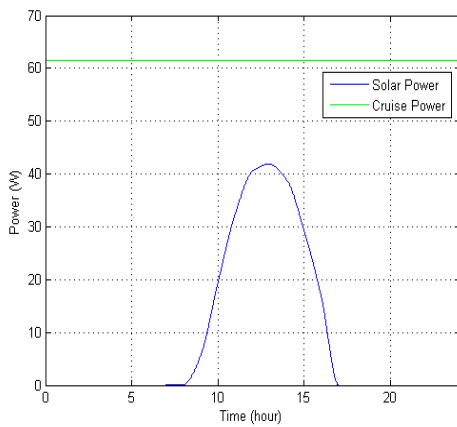
(a) December solstice.
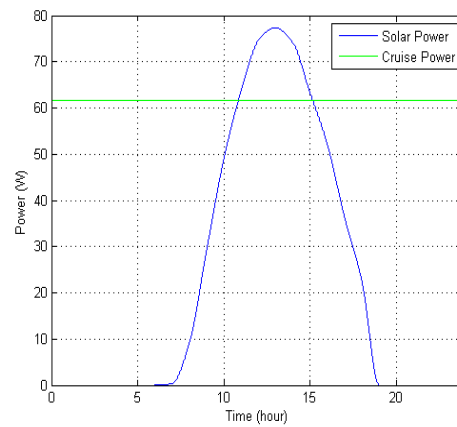
(b) March equinox.
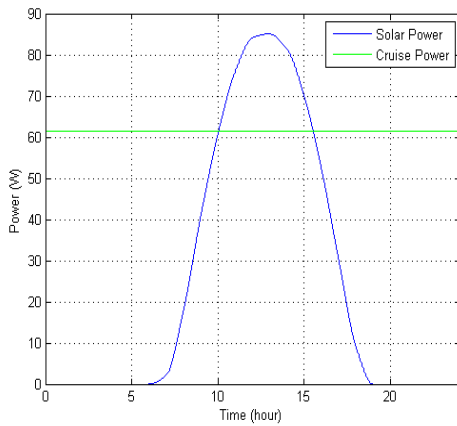
(c) September equinox
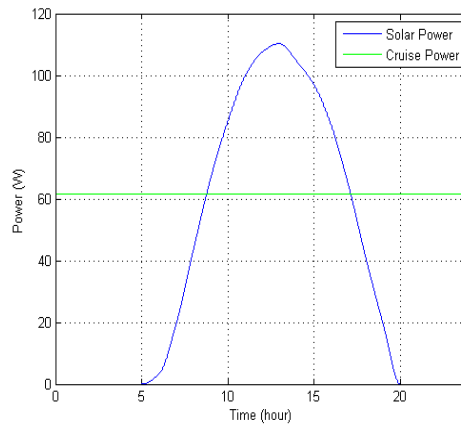
(d) June solstice

Figure 5.6: Power required for steady cruise flight and daily solar net power available at several times of the year in Pampilhosa da Serra (h=1300 m).

74

For each power profile, the energy provided by the solar panels corresponds to the area under the curve, that was calculated by numerical integration with the trapezoidal method.

$$E = \int_a^b P(t)dt \approx \frac{(b-a)}{2N} \cdot \sum_{n=1}^N (P(t_n) + P(t_{n+1})), \qquad (5.26)$$

where the spacing between each point is equal to the scalar value $\dfrac{b-a}{N}$.

Table 5.4 summarizes all information retrieved from the power curves of all equinoxes and solstices. It includes the solar energy harnessed for cruise, $\mathbf{E_{PV\,cruise}}$, as well as maximum endurance, $\mathbf{\Delta t_{cruise\,max}}$, and range. The number of 3S LiPo batteries, with 4200 mAh capacity, used in data treatment ranges from two, that is the standard airborne amount determined in Section 4.3.1, to three, assuming that the third battery is included on the extra payload weight, i.e., the weight of the aircraft does not change. To provide another energy measure reference to the reader, the solar energy used during cruise is also given by the equivalent quantity of airborne batteries, that is the ratio $\mathbf{E_{PV\,cruise}/E_{LiPo\,3S}}$.

	December Solstice		March Equinox		September Equinox		June Solstice	
No. Batteries	2	3	2	3	2	3	2	3
$\mathbf{E_{PV\,cruise}}$ (Wh)	46.11	115.01	440.576	443.50	588.77	606.42	754.43	817.13
$\mathbf{E_{PV\,cruise}/E_{cruise}}$ (%)	64.98	61.67	94.67	86.11	95.94	89.45	96.81	91.95
$\mathbf{E_{PV\,cruise}/E_{LiPo\,3S}}$	0.9893	2.46	9.45	9.51	12.62	13.00	16.18	17.52
$\mathbf{E_{PV\,stored}/E_{PV\,cruise}}$ (%)	0	0	10.37	10.30	15.15	14.71	12.35	17.11
$\mathbf{E_{PV\,lost}/E_{PV\,available}}$ (%)	0	0	0	0	0	0	18.59	13.33
$\mathbf{\Delta t_{cruise\,max}}$ (hour:min)	1:09	3:01	7:34	8:22	9:58	11:01	12:40	14:26
Cruise starting hour	11:25 AM	10:29 AM	10:49 AM		8:28 AM	7:25 AM	7:19 AM	6:18 AM
Cruise ending hour	12:34 PM	13:30 PM	18:23 PM	19:11 PM	18:26 PM		19:59 PM	20:44 PM
$\mathbf{\Delta t_{E\,surplus}}$ (hour:min)	0:00		4:19		5:28		8:21	
Range (km)	31.2	82.1	205.1	226.8	270.3	298.6	343.3	391.4

Table 5.4: Maximum endurance performance between all seasons in Pampilhosa da Serra (h=1300 m).

Observing Figure 5.6a, it is clear that during the December solstice, the shortest day of the year, solar energy alone does not suffice for cruise. The usage of battery energy during cruise reflects on the lower values of $\mathbf{E_{PV\,cruise}/E_{cruise}}$ when compared with the other seasons. In this case, the start time of cruise was calculated iteratively, with the peak of solar power as midpoint, so that the sum of received and stored energy would allow cruise time period to be maximized. Even though solar energy accumulated in batteries, $\mathbf{E_{PV\,stored}}$, is null, the addition of a third battery allows the system to collect about 2.5 times more solar energy, which causes a major range increase from 31.2 to 82.1 km.

In the March equinox profile it is observed that solar power surpasses the required to cruise during a time interval, $\mathbf{\Delta t_{E\,surplus}}$, of 4 hours and 19 minutes. Thereupon, it was established that cruise would start at the hour of the day in which solar power equals the minimum required for steady flight, such instant corresponds to the first intersection between line plots in Figure 5.6b. In the long run, all exceeding solar energy can be stored with 2 batteries and used afterwards during the period of solar energy shortage. Nonetheless, the maximum endurance only reaches the 8 hour mark with a third

battery in line that is not used for solar energy storage but allows to extend endurance throughout the period of solar energy deficit.

During the September equinox, there is an higher amount of solar power when compared with the March equinox, explained by an increase on the angle of incidence of solar beam irradiation. With this, steady flight can be prolonged for over 9 hours, clearly surpassing the endurance requirement. Notwithstanding, it is observed that batteries would not be able to retain all solar energy if, as in the previous equinox, cruise were to begin when available power equals flight consumption. Although the registered surplus of 89.22 Wh can be contained within 2 empty batteries, the energy remaining in the storage system after climb would reduce the storage volume available. Subsequently, to prevent extra energy losses, the cruise starting hour was hastened so that when solar power alone allows steady flight the whole storage system is virtually empty. Hence, cruise is initially powered by batteries along with increasing solar power, which maximizes energy storage afterwards. Adding a third battery, while relying on the same energy storage enhancement plan, boosts the mission during the first period of solar energy deficit by allowing it to begin more than one hour earlier.

In the solstice of June, given as the longest solar day of the year, solar power unsurprisingly achieves optimum ratings. Yet the gains registered are such that the exceeding solar energy even surpasses the storage limits of 3 batteries. Under this circumstance, even maximizing energy storage does not prevent significant energy losses. Still, having a third battery on-board brings a meaningful endurance bonus, from 12 hours and 40 minutes with 2 batteries to 14 hours and 26 minutes, while reducing solar energy loss ratio, $\mathbf{E_{PV\,lost}}/\mathbf{E_{PV\,available}}$, from 18.84 % to 13.35 %. Moreover, with 3 batteries, at evening a flight period of 44 minutes is reached in the absence of solar energy. Alternatively, the solar irradiance daily distribution in the June solstice could be fully harnessed by the LEEUAV, nullifying storage energy losses in the system, if multi-climb mission profiles were to be orchestrated.

5.3.2 Reduced Climb Assumption

Examining more closely the March equinox power plot in Figure 5.6b, solar energy exceeds the required to cruise by an absolute amount of 45.71 Wh, which is less than what can be stored within a single battery, 46.62 Wh. Assuming that the second battery is never recharged in that situation, it would be more efficient to simply drop it outside as empty weight after climb. Simply discarding of an expensive battery is not a foreseeable solution, however, that would not be necessary if climb time were to be reduced so that only one battery provides enough energy to go through that stage.

No. Batteries	Cruise Speed	$\mathbf{E_{PV\,stored}}$ (Wh)	$\dfrac{\mathbf{E_{PV\,stored}}}{\mathbf{E_{PV\,cruise}}}$	$\dfrac{\mathbf{E_{PV\,cruise}}}{\mathbf{E_{cruise}}}$	$\dfrac{\mathbf{E_{PV\,lost}}}{\mathbf{E_{PV\,available}}}$	$\mathbf{\Delta t_{cruise}}$	Range (km)
1	7.08 m/s	46.62	9.6 %	97.11 %	7.76 %	9 h 24 min	239.7
2	7.53 m/s	45.71	8.61 %	89.99 %	0 %	9 h 35 min	259.8

Table 5.5: Energy performance results with climb time reduced to 5 minutes in the March equinox.

Assuming a 5 minute climb at the same rate stipulated in the requirements, it was determined that

subtracting one battery to the overall flying weight in the March equinox does not improve the performance obtained when carrying two batteries with MTOW. The results of that analysis are presented in Table 5.5, it should be noted that the airplane with less 351 grams, the weight of a single battery, can afford to fly steady at a slightly lower speed of 7.08 m/s, which leads to a decrease in cruise power from 61.5 W to 53.18 W. Nevertheless, it was verified that only one battery on-board still brings less endurance and range when compared with the standard double battery arrangement. This is due to the solar losses of 7.76 % caused by the increased solar energy surplus of 79.14 Wh that surpasses the single battery storage limit.

5.3.3   Night Mission (non-rechargeable battery)

Another alternative flight scenario is a night mission, in which there is no solar energy to be collected. When relying solely on battery stored energy, performance ends up abruptly shortened, as shown in Table 5.6, that was obtained assuming the imposed 10 minute climb. Adding a third battery almost triples the energy left to cruise, but it still is remains far from the marks achieved during daytime.

No. Batteries	E_{flight}	E_{climb}/E_{flight}	E_{cruise}/E_{flight}	$\Delta t_{cruise\,max}$	Range (km)
2	93.24 Wh	73.4 %	26.6 %	24 min	10.9
3	139.86 Wh	48.9 %	51.1 %	69 min	31.4

Table 5.6: Energy performance data with non-rechargeable batteries.

Looking back at the standard mission profile, the table above also documents the energy margin that is left in the battery storage system when transitioning from climb to solar powered cruise.

5.4   Avionics Energy Requirements

The communications system power consumption was also accounted for in cruise energy balance computations, described in Section 5.3, as well as in climb energy calculations, in Section 4.3.1.

Regarding control system components, a simple static test has been performed in [56] to the Autopilot and RC receiver. The on-board video transmission (Tx, OSD and camera) was tested in laboratory for this thesis. It was verified that both OSD and camera have negligible energy consumption, while the video transmitter poses most of it.

Component	Current (mA)	Voltage (V)	Power (W)
RC Rx	240	12.33	2.96
Video Tx	178.3	12.46	2.22
Total	—-	—-	5.18

Table 5.7: Communication components testing in energy consumption.

All measured outputs, given in Table 5.7, were considered constant standard values for the entire mission because their energy consumption depends on too many variables, for example, the type of

flight operation (if it is manual or automatic control) or how much use is given to the control actuators.

5.5 Discussion of Energy System Setup

Table 5.8 provides a measure of the impact propulsion and communications have on power consumption during climb and cruise. After comparing the power consumption of both systems it was seen as beneficial for weight reduction to harbor a common set of batteries for all on-board systems.

Stage	$\dfrac{\mathbf{P_{prop}}}{\mathbf{P_{stage}}}$	$\dfrac{\mathbf{P_{autopilot}}}{\mathbf{P_{stage}}}$	$\dfrac{\mathbf{P_{RPV}}}{\mathbf{P_{stage}}}$	$\mathbf{P_{stage}}$ (Watt)
Cruise	91.6%	4.8 %	3.6 %	61.5
Climb	98.8%	0.7%	0.5 %	410.3

Table 5.8: Standard power consumption data for cruise and climb.

Due to the power module feature the battery power source of the autopilot will always be the same as the motor's, the same does not apply to RPV. Analyzing the design of the RPV system [56], it is known that 12 V from a 3S LiPo battery must feed directly the FPV camera and video transmitter. Knowing the standard video power consumption from Table 5.7, an isolated battery would need a capacity of 1600 mAh to power RPV for eight hours, because $C \cdot V = 1600[mAh] \cdot 11.1[V] \approx 17.76Wh$ and $P_{RPV} \cdot t_{cruise} = 2.22[W] \cdot 8[h] = 17.76Wh$. In terms of mass, it means an increase in at least 128 grams, that corresponds to the weight of an Hyperion battery with those characteristics. Looking at the small impact of RPV on the overall consumption during climb, and attending to the losses of solar energy during longer solar days, connecting the RPV system to the rechargeable set of batteries was perceived as the most efficient solution for a wider range of situations.

After analyzing the solar profile of the longest solar day of the year, it was possible to determine the peak of power received by the MPPT due to the double set of 2x6 and 2x7 PV arrays, that is given by

$$P_{MPPTmax} = P_{solarmax}/\eta_{MPPT} \approx 125W, \tag{5.27}$$

where $P_{solarmax}$ corresponds to the maximum power value in the plot of Figure 5.6d. Then, it was verified that $P_{MPPTmax}$ does not surpass the maximum power limit of the MPPT, $P_{MPPTmaxlimit}$, that assumes a value of 140 W.

Chapter 6

Detailed Design Considerations

The structural design of the LEEUAV does not fall under the scope of this thesis, regardless, there are aerodynamic loads that will have to be transferred to a detailed design computational analysis, in which the airframe estimate will be rectified. Besides describing how wing loading data was obtained, this chapter also serves to remark CAD work performed and specific assembly solutions that need to be engineered so that the LEEUAV may advance to manufacturing.

6.1 Main Wing Break-Up

m_{airframe} (kg)	$\dfrac{m_{\text{wing}_{\text{center}}}}{m_{\text{airframe}}}$	$\dfrac{m_{\text{wing}_{\text{lateral}}}}{m_{\text{airframe}}}$	$\dfrac{m_{\text{fuselage}}}{m_{\text{airframe}}}$	$\dfrac{m_{\text{stabilizer}}}{m_{\text{airframe}}}$
2.73	25.5 %	43.6 %	25.8 %	5.1 %

Table 6.1: Estimated airframe mass distribution.

The airframe mass fractions presented in Table 6.1 were obtained during the initial sizing, in Chapter 3, resorting to the aircraft database in Appendix C and assuming that all components have constant mass density. As in the first generation LEEUAV, solar arrays were arranged so that the wing can be divided into three parts. The central part has 1858 mm of span and each lateral 1571 mm, as seen in Figure 6.1, totaling 5000 mm. A continuous central part reduces structural weakness in sections near the axis of symmetry, where strain will be higher.

Figure 6.1: Main wing break-up.

6.2   Wing Loading Estimate

The pressure coefficient (C_p) distribution is a mandatory input to evaluate distinct structural wing solutions with Finite Element Method (FEM) analysis. Admittedly, C_p distribution can only be retrieved in XFLR5 by modeling the wing as a thick surface, what only happens when executing a 3D Panel Method analysis. Recalling aerodynamic software accuracy studies, in Section 4.1.1, the 3D Panel Method could not be applied earlier because it does not accept tail geometries. In this case the tail is expendable, so the 3D Panel Method analysis was performed with the wing as sole geometry. The C_p wing distribution results at cruise speed are visible in Figure 6.2, where suction and pressure surfaces, responsible for the overall lift force during cruise regime, are distinguished.
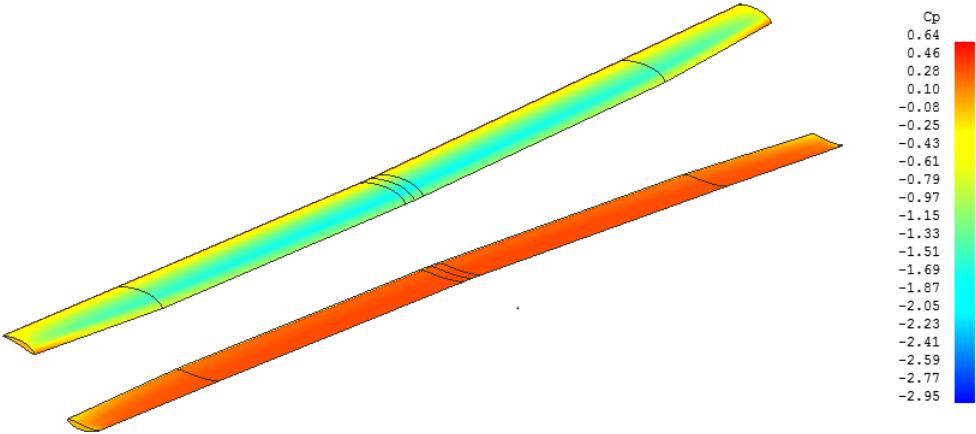
Figure 6.2: C_p distribution in upper and lower wing surfaces (computed in XFLR5).
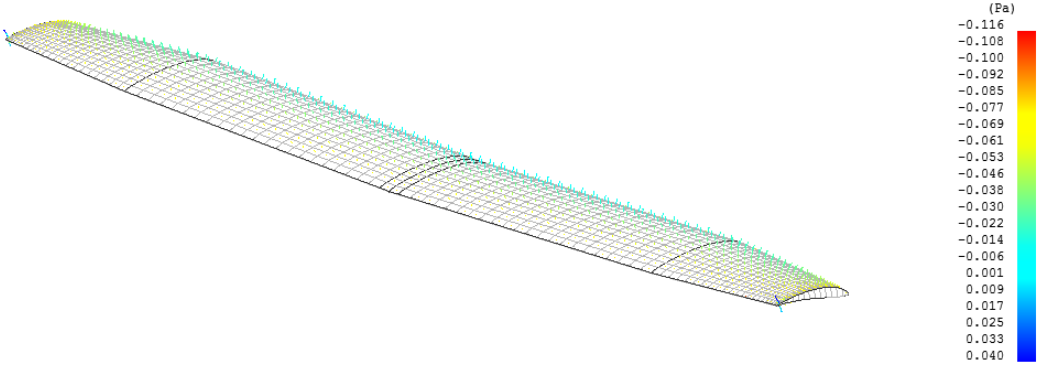
Figure 6.3: Wing panel mesh with singular pressure points.

It is noted that C_p distribution is calculated as the derivative of the doublet strength along the panel chordwise and spanwise strips, displayed in Figure 6.3. Meaning approximately 2500 registered pontual forces, each corresponding to a panel in the mesh, will have to be inserted in the FEM analysis software. This should be done preferentially with programming loops.

Additionally, to assure that the tested solution endures all structural requirements, it is necessary to determine, using iterations, the wing load distribution that occurs at the flight velocity in which the maximum load factor of 2.5 is reached. Such velocity value is expected to be found between the maneuvering

speed and the dive speed illustrated in the V-n diagram of Figure 4.25.

6.3   Fuselage Layout

Unlike the wing, the fuselage's shape was highly influenced by the positioning of on-board components in stability studies. As a whole piece, the fuselage has an overall length of 1.9 meters, which may hamper ground transportation in a small vehicle. For that reason it was divided in two parts, illustrated in Figure 6.4, having a front part with 1.16 meters length and a rear part where the stabilizers are installed along with the motor. It should be noted that it is yet to be designed a snap fit mechanism that allows to assemble fuselage parts with airworthy stiffness.
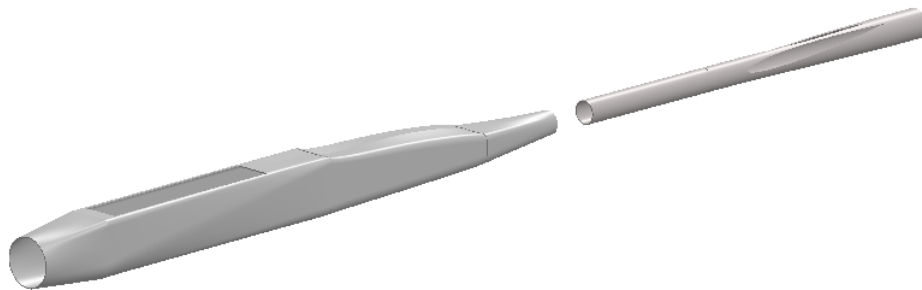
Figure 6.4: Fuselage divided into two connectable parts.

The fuselage front part is meant to support the wing and harbor the majority of components. Figure 6.5 shows how communication systems, batteries and MPPT were fit in the fuselage. In terms of stability, the batteries and the MPPT represent the biggest influence due to their weight, also, there is still enough room to store a third battery.
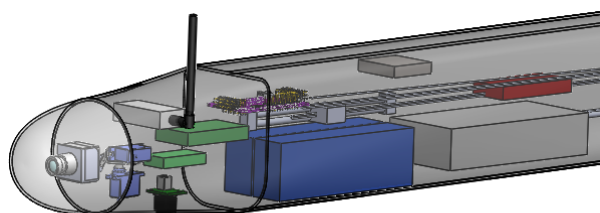
Figure 6.5: Fuselage front part with components.

It is also noted that the RPV camera, with pan and tilt motion provided by a set of two servos, is aerodynamically protected by a transparent nose cover upfront that allows it to record footage from inside. The video transmitter antenna that appears attached outside should be a skew planar wheel model but it was not completely portrayed in CAD for a matter of simplicity, as well as other components that were modeled using only standard geometric volumes with similar dimensions. Although the components positioning has been defined, the current fuselage still lacks an internal compartment fabric to hold them.

6.4   Tail Assembly

The actual V-tail CAD, visible in Figure 6.6, is only made of extruded volumes. Similarly to the wing, it does not have a defined internal structure with the control surface mechanism fully designed. Fixed V-Tails are more susceptible to transportation damages because they cannot be stored in the same plane. A more compact storage can be achieved by using individually removable tail halves, in which servos should be embedded to ease control actuation and wiring. This solution brings further assembly difficulties, as the rear fuselage will have to possess enough volume and stiffness to have a working motor while keeping reinforcing inserts to assure a strong connection between portable parts.
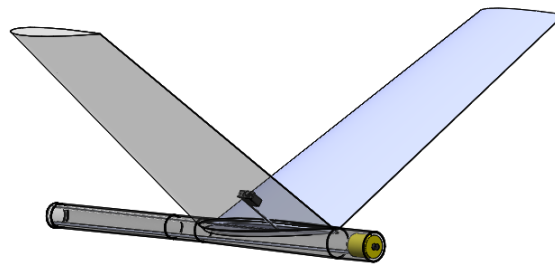
Figure 6.6: Rear fuselage assembly with V-tail.

Ultimately, the future work advanced in this chapter will have to continue the iterative design procedure that has been described in previous chapters. Such discussion is presented in the concluding chapter of this thesis.

Chapter 7

Conclusions

This final chapter starts by summarizing how the working goals of the LEEUAV design have been gradually achieved and reported in the present document. Envisioning the future of the project, a few advice concerning forthcoming works are also exposed at this point. Tasks that must be prioritized are addressed first, while other possible studies are scrutinized lastly.

7.1   Project Achievements

The first relevant achievement of this thesis is the conceptual design selection, that is described in Chapter 2. Resorting to the AHP method, the rear pusher V-tail airplane concept was chosen through pairwise comparisons between mission criteria and 8 prospective candidate configurations.

The initial estimation of LEEUAV characteristics was accomplished by allying knowledge from previous project related works with a newly conceived mass estimation model. A UAV market research, targeting low weight models with dimensions similar to the first generation prototype, allowed to narrow down the type of wing construction, that contains ribs and heat shrinking film skin. From there, a correlation placing empty weight as function of wingspan was computed, enabling an initial estimate of the empty weight fraction.

Afterwards, the aircraft was resized by performing a set of fixed point iterations that ensure it is physically possible to achieve all flight requirements. In Chapter 4, multiple aerodynamic analysis were performed with VLM method on XFLR5 freeware until the overall lift produced at cruise velocity equaled the MTOW obtained in the mass estimation model. The LEEUAV CAD assembly was partially done, it lacks structural details but the arrangement of components inside the wing and fuselage was defined. Each individual mass center was transferred from SolidWorks® to XFLR5, where stability studies were performed, resulting in a static margin of 5.6% with null C_m in cruise conditions. Furthermore, longitudinal and lateral flight modes were also verified with a built-in dynamic stability analysis tool in XFLR5.

The drag polar curves extracted from cruise and climb aerodynamic analysis were used to determine the power consumptions under ideal weather conditions. Propulsion components were selected to provide more than enough power to climb. The propeller, in particular, had its efficiency enhanced thanks to

a study involving performance data-sheets supplied by APC manufacturer. To make climb endure more than 10 minutes, the battery system was sized to sustain the appropriate amount of energy and leave a large portion behind to switch to cruise. The maximum steady flight regime was computed by crossing aerodynamic data with propulsive performance.

Regarding endurance, the power and energy received by the arranged solar arrays was determined for different seasons of the year. A daily irradiation model was computed for a single flight location using analytic relations, bibliographically supported, and historic irradiation data available online. Having estimated the solar system efficiency, the daily solar power profile was traced for each equinox and solstice. Respective endurance values were obtained knowing power consumption during cruise. Attending to the established 8 hour requirement, it was verified that in the March equinox endurance comes up short with a mark of 7 hours and a half. Conversely, the performance in the September equinox excels with a maximum endurance of almost 10 hours.

After concluding solar energy management studies, the airplane's design point, whose representative stage is cruise, was converged along with the off-design point associated with climb. All dimensions of the airframe, featuring a double set of 2x6 and 2x7 PV arrays on the wing, have been determined.

Using preliminary converged data, the flight envelope at cruise altitude was created. It possesses a maximum load factor of 2.5 and maximum gust velocities of 5 m/s and 2.58 m/s, for maneuvering and dive speeds, respectively. As additional groundwork for a prospective aircraft detailed design, the C_p wing distribution at cruise speed was obtained in XFLR5 by performing a 3D Panel Method analysis.

7.2 Future Work

In order to reach manufacture in the nearest future, it is essential to complete the structural project branch of the LEEUAV. Beginning with the wing, its ribbed structure will have to be defined in detail. Among electable designs are D-box wings, which have been produced for the first generation LEEUAV, and more orthodox non-sheeted wings containing a spar connecting ribs instead. The wing must have sturdy mechanical connectors to link each portable part, as well as supports between ribs to mount solar arrays. At least two wing structure proposals should be modeled with a CAD tool and evaluated on a computational FEM stress analysis. Displacement boundary conditions must not be forgotten and wing loading data is to be treated as explained in the previous chapter. Material properties, that can be obtained either by bibliographic research or with experimental tests, are also a required input for FEM analysis. The materials applied on the first generation, which are tabulated in Section 3.1 of the initial sizing, can serve as a starting point. Afterwards, depending on the stress analysis results, manufacture materials may have to be revised. Concerning the fuselage, all CAD assembly issues mentioned in Chapter 6 do not pose the same structural complexity of the wing. Nonetheless, given the bending moment that will be caused by the V-tail and motor on the rear, it is recommended to perform at least a simplified FEM computational analysis on the fuselage as well.

The purpose of the structural project on the overall iterative design procedure is to replace the airframe estimation model, that was given in the initial sizing by Equation (3.1). Supposing that the detailed

design imposes an airframe weight that surpasses the estimate, there is still an error margin assured by the extra payload of 690 g, registered in Table 3.19a. Thus, the design point of the LEEUAV is not expected to suffer reiterations due to the detailed design.

As soon as the structural project is fully complete, advanced construction methodologies will have to be found and applied. Experimental techniques can also be arranged to verify the accuracy of FEM computational analysis and to study the residual resistance of the prototype in the presence of defects. At the same time, the take-off system must be engineered. The 5 meter wingspan LEEUAV will not be able to surpass stall speed when hand-launched by most human operators, therefore a launch trolley will have to be manufactured as well. To prevent collisions with the tail while transitioning to air, it is suggested a trolley geometry featuring support surfaces for each side of the wing and a third fuselage support area ahead of the CG.

With the prototype built, a set of planned flight tests must be progressively carried on. Initially, short range flights will serve to examine airborne communication features and evaluate flight qualities related to stability and maneuverability. After succeeding on the first battery of tests, the defined flight time window will keep increasing until the accomplishment of more critical performance requirements, such as climb and endurance, can be confirmed as well.

Preliminary performance calculations can be improved with experimental determination of propulsion efficiency rates that so far have only been estimated, namely the motor's. The experimental apparatus for wind tunnel testing of electric UAV propulsion systems developed in [99] can be used to access efficiency values under controlled variables, such as airflow speed and RPM.

Regarding aerodynamics, it is possible to virtually eliminate the uncertainty and limitations associated to the results obtained in XFLR5 if a CFD computational analysis is performed on the updated airframe geometry. Observing the XFLR5 accuracy studies in Section 4.1.1, as long as the drag correction applied does not underestimate real values roughly, the current design will still be able to fulfill the mission requirements. Climb performance is expected to end up more changed than cruise's because it depends not only on drag polar computations but also on the estimate made for stall at higher angles of attack. Moreover, the determination of C_{Lmax} may become even more exact by employing CFD to study the aerodynamic effects of deflected ailerons acting as flaps during take-off and climb.

Finally, an additional work with no significant repercussions to the current project consists in the development of an improved radiation prediction model. In terms of mission planning, a major upgrade would be the capability to calculate solar profiles for given routes, which demands the implementation of more complex programming algorithms capable of treating data from several sets of coordinates.

Bibliography

[1] Justin Murphy. *Military Aircraft Origins to 1918*, chapter 1. ABC CLIO, 2005.

[2] Jim Garamone. From U.S. Civil War to Afghanistan: A Short History of UAVs. http://www.defense.gov/news/newsarticle.aspx?id=44164, 2002. Accessed: 2015-05-19.

[3] The Ryan Firebee: Grandfather to the Modern UAV. http://gizmodo.com/the-ryan-firebee-grandfather-to-the-modern-uav-1155938222, 2013. Accessed: 2015-11-11.

[4] Consistent Growth for UAV Market to Push Industry Above $ 10 Billion Mark by 2024, IHS Says. http://press.ihs.com/press-release/aerospace-defense-security/consistent-growth-uav-market-push-industry-above-10-billion, October 2015. Accessed: 2015-10-15.

[5] TEKEVER drone tracks lava flow at Pico do Fogo volcano capturing dazzling images. http://tekevernews.blogspot.pt/2015/01/tekever-drone-tracks-lava-flow-at-pico.html, January 2015. Accessed: 2015-10-19.

[6] Tecnologia da Universidade de Aveiro põe drone a vigiar as florestas. http://www.publico.pt/tecnologia/noticia/tecnologia-da-universidade-de-aveiro-poe-drone-a-vigiar-as-florestas-1693988, April 2015. Accessed: 2015-10-19.

[7] Amazon Prime Air. http://www.amazon.com/b?node=8037720011. Accessed: 2015-10-16.

[8] DHL parcelcopter launches initial operations for research purposes. http://www.dhl.com/en/press/releases/releases_2014/group/dhl_parcelcopter_launches_initial_operations_for_research_purposes.html, September 2014. Accessed: 2015-10-16.

[9] TU Delft's ambulance drone drastically increases chances of survival of cardiac arrest patients. http://www.tudelft.nl/en/current/latest-news/article/detail/ambulance-drone-tu-delft-vergroot-overlevingskans-bij-hartstilstand-drastisch/, October 2014. Accessed: 2015-10-19.

[10] 'Ambulance drone' takes to the skies. http://www.bbc.com/news/world-europe-30064687, November 2015. Accessed: 2015-10-19.

[11] Wilborn P. Nobles. Drone hobbyists continue to interfere with wildfire battles in West. http://www.washingtonpost.com/news/morning-mix/wp/2015/08/19/drone-hobbyists-continue-to-interfere-with-wildfire-battles-in-west/, August 2015. Accessed: 2015-10-19.

[12] Manchester fire service uses drone to fight blazes. http://www.bbc.com/news/34637892, October 2015. Accessed: 2015-11-5.

[13] Pedro Sales Dias. Falcões e águias da GNR em teste final para caçar incêndios nos céus do Gerês. https://www.publico.pt/sociedade/noticia/falcoes-e-aguias-da-gnr-em-testes-finais-para-cacar-incendios-nos-ceus-dos-geres-1689184, March 2015. Accessed: 2015-11-5.

[14] K-MAX. http://www.lockheedmartin.com/us/products/kmax.html. Accessed: 2015-10-19.

[15] Drones take to the agricultural skies. https://gereports.ca/drones-take-to-the-agricultural-skies/, September 2014. Accessed: 2015-10-20.

[16] R-MAX Agricultural use. http://rmax.yamaha-motor.com.au/agricultural-usel. Accessed: 2015-10-20.

[17] João Gomes Mota, Ricardo Oliveira, Sandra Antunes, and Vítor Almeida. Testes Utilizando Unmanned Aerial Vehicles para Inspeções em Redes de Transmissão Elétrica. In *I Seminário Internacional de UAV*, March 2016.

[18] João Gomes Mota and Sandra Antunes. Target-fencing for RPAS power line inspections. In *1st International Conference on RPAS related Technologies*, November 2015.

[19] João Gomes Mota, Ricardo Oliveira, and Sandra Antunes. Field trials with Unmanned Aerial Vehicles on Transmission Grids. In *International Conference on Condition Monitoring, Diagnosis and Maintenance (3rd Edition)*, October 2015.

[20] João Gomes Mota, Ricardo Oliveira, and Sandra Antunes. Implementação de Sistemas de Inspeção de Linhas Alternativos ao Helicóptero. In *XVI Encuentro Regional Iberoamericano de Cigré*, May 2015.

[21] Sandra Antunes and Kouamana Bousson. Safe Flight Envelope for Overhead Line Inspection. In *3rd International Conference on Applied Robotics for the Power Industry*, October 2014.

[22] Drone detalha devastação no leito do rio Doce. http://noticias.r7.com/minas-gerais/fotos/drone-detalha-devastacao-no-leito-do-rio-doce-12112015#!/foto/1, November 2015. Accessed: 2015-11-12.

[23] Equipes usam drones e cães em buscas em Mariana neste sábado. http://noticias.r7.com/minas-gerais/equipes-usam-drones-e-caes-em-buscas-em-mariana-neste-sabado-11112015, November 2015. Accessed: 2015-11-12.

[24] Drones are about to change how directors make movies. http://www.wired.com/2015/03/drone-filmmaking/, June 2015. Accessed: 2015-11-12.

[25] PSP autorizada a utilizar aeronave não tripulada com duas câmaras na final da Champions. http://www.publico.pt/sociedade/noticia/psp-autorizada-a-utilizar-aeronave-nao-tripulada-com-duas-camaras-na-final-da-liga-1637285, May 2014. Accessed: 2015-10-20.

[26] UAV em missão no Mar Português. http://www.emfa.pt/www/noticia-569-uav-em-%20missao-no-mar-portugues, May 2014. Accessed: 2015-11-10.

[27] Civil Aviation Safety Authority. CASR Part 101 - Unmanned aircraft and rocket operations History. https://www.casa.gov.au/standard-page/casr-part-101-unmanned-aircraft-and-rocket-operations-history-0. Accessed: 2016-09-28.

[28] Alliance for System Safety of UAS through Research Excellence. http://www.assureuas.org. Accessed: 2016-09-28.

[29] Center of Excellence (COE) and FAA Test Sites. https://www.faa.gov/uas/programs_partnerships. /coe_test_sites/. Accessed: 2016-09-28.

[30] Guidance on operating permissions for drones. http://www.caa.co.uk/Commercial-industry/Aircraft/Unmanned-aircraft/Guidance-on-operating-permissions-for-drones, . Accessed: 2016-09-28.

[31] Apply for a permission to fly drones for commercial work. http://www.caa.co.uk/Commercial-industry/Aircraft/Unmanned-aircraft/Apply-for-a-permission-to-fly-drones-for-commercial-work, . Accessed: 2015-09-28.

[32] Regulation (EC) No 1592/2002 of the European Parliament and of the Counsil on common rules in the field of civil aviation and establishing a European Aviaton Safety Agency, July 2002. Article 4, Paragraph 2.

[33] Lei para drones no início de 2015. http://www.computerworld.com.pt/2014/11/29/lei-para-drones-no-inicio-de-2015/, November 2014. Accessed: 2015-11-11.

[34] Autoridade Nacional de Aviação Civil. I Seminário sobre Regulamentação e Utilização de Sistemas de Aeronaves Pilotadas Remotamente (RPAS), February 2015. Accessed: 2015-11-11.

[35] Nuno Silva. Parametric Design, Aerodynamic Analysis and Parametric Optimization of a Solar UAV. Master's thesis, Instituto Superior Técnico, June 2014.

[36] Project Sunrise - Flight of the Worlds First Solar Powered Aircraft. http://www.projectsunrise.info/First_Solar_Powered_Aircraft.html. Accessed: 2015-11-11.

[37] André Noth. History of Solar Flight. Technical report, Autonomous Systems Lab, Swiss Federal Institute of Technology Zürich, July 2008.

[38] NASA Armstrong Fact Sheet: Pathfinder Solar-Powered Aircraft. http://www.nasa.gov/centers/armstrong/news/FactSheets/FS-034-DFRC.html, February 2014. Accessed: 2015-11-11.

[39] NASA Dryden Past Projects: Helios Prototype Solar-Powered Aircraft. http://www.nasa.gov/centers/dryden/history/pastprojects/Helios/index.html, November 2009. Accessed: 2015-11-11.

[40] NASA Armstrong Fact Sheet: Centurion Remotely Piloted Solar-Powered Airplane. http://www.nasa.gov/centers/armstrong/news/FactSheets/FS-056-DFRC.html, February 2014. Accessed: 2015-11-11.

[41] Zephyr Solar-Powered HALE UAV, United Kingdom. http://www.airforce-technology.com/projects/zephyr. Accessed: 2015-11-11.

[42] QinetiQ's Zephyr solar aircraft double award by IET. http://www.qinetiq.com/media/news/releases/Pages/Zephyr-wins-two-awards.aspx, November 2011. Accessed: 2015-11-11.

[43] Martin Luiz Gomes and Andrew Cox. Flying Aquila: Early lessons from the first full-scale test flight and the path ahead. https://code.facebook.com/posts/268598690180189, July 2016. Accessed: 2016-07-22.

[44] Alan Levin. Google's Solar-Fueled Cyber Drone Crashes in New Mexico Test. http://www.bloomberg.com/news/articles/2015-05-29/google-s-solar-fueled-cyber-drone-crashes-during-new-mexico-test, May 2015. Accessed: 2015-11-11.

[45] Graham Warwick. Google Perseveres After Titan UAV Crash. http://aviationweek.com/technology/google-perseveres-after-titan-uav-crash, June 2015. Accessed: 2015-11-11.

[46] André Noth. *Design of Solar Powered Airplanes for Continuous Flight*. PhD thesis, ETH Zurich, September 2008.

[47] Sky-Sailor. http://www.sky-sailor.ethz.ch/. Accessed: 2015-11-12.

[48] AtlantikSolar. http://www.atlantiksolar.ethz.ch/?attachment_id=452, . Accessed: 2015-11-12.

[49] Atlantik-Solar project brochure, . ETH Zurich.

[50] *A Solar-Powered Hand-Launchable UAV for Low-Altitude Multi-Day Continuous Flight*, 2015. ICRA 2015, ETH Zurich.

[51] Solar-powered 81-hours flight successful: A new endurance world record! http://www.atlantiksolar.ethz.ch/?p=670, July 2015. Accessed: 2015-11-11.

[52] Solar Impulse. http://www.solarimpulse.com/, . Accessed: 2015-11-12.

[53] We are in Abu Dhabi. http://www.solarimpulse.com/leg-17-from-Cairo-to-Abu_Dhabi, . Accessed: 2016-07-06.

[54] Tiago Ferreira. Hybrid Propulsion System of a Long Endurance Electric UAV. Master's thesis, Instituto Superior Técnico, November 2014.

[55] Héctor Vidales. Design, Construction and Test of the Propulsion System of a Solar UAV. Master's thesis, Instituto Superior Técnico, March 2013.

[56] Pedro Miller. Remote Person View (RPV) for a Long Endurance Electric UAV. Master's thesis, Instituto Superior Técnico, May 2015.

[57] Duarte Figueiredo. Autopilot and Ground Control Station for UAV. Master's thesis, Instituto Superior Técnico, November 2014.

[58] Luís Cândido. Projeto de um UAV Solar de grande autonomia. Master's thesis, Universidade da Beira Interior, October 2014.

[59] MODEL ROCKET SAFETY CODE. http://www.nar.org/safety-information/model-rocket-safety-code/, August 2012. Accessed: 2015-06-24.

[60] HIGH POWER ROCKET SAFETY CODE. http://www.nar.org/safety-information/high-power-rocket-safety-code/, August 2012. Accessed: 2015-06-24.

[61] Mark Canepa. *Modern High-Power Rocketry 2*, chapter 10. Trafford, 2005.

[62] S. D'Urso and R.Martinez. Flight Dynamics of the Flying Wing. In *26th International Congress of the Aeronautical Sciences*, 2008.

[63] Ilan Kroo. Nonplanar Wing Concepts for Inceased Aircraft Efficiency. Technical report, Stanford University, June 2005. Von Karman Institute for Fluid Dynamics, lecture series "Innovative Configurations and Advanced Concepts for Future Civil Aircraft".

[64] Lightweight, foldable pneumatic catapult for Wavesight UAV. http://www.pros3.it/?q=node/166. Accessed: 2015-09-01.

[65] Thomas L. Saaty. *The Analytic Hierarchy Process: Planning, Priority Setting, Resource Allocation*. McGraw-Hil, 1980.

[66] Martin Hepperle. *Electric Flight – Potential and Limitations*. NATO-OTAN, Portugal, 2012.

[67] Thomas L. Saaty. *How to make a decision: The Analytic Hierarchy Process*. University of Pittsburgh, Pittsburgh, PA 15260. USA, 1990.

[68] André Calado Marta. Long Endurance Electric UAV. Technical report, Instituto Superior Técnico, 2013.

[69] Hyperion Zs30 Series Outrunners. http://media.hyperion.hk/dn/zs/zs30.htm, . Accessed: 2016-05-15.

[70] 3D Robotics. APM 2.6. https://3dr.com/wp-content/uploads/2013/07/APM-2.6-web-version.pdf. Accessed: 2016-05-10.

[71] Rx700 Long Range. http://www.tslrs.com/products/rx700-long-range/. Accessed: 2016-05-10.

[72] 3DR Power Module. Connecting the PM to a flight controller board. http://ardupilot.org/copter/docs/common-3dr-power-module.html. Accessed: 2016-05-10.

[73] 3DR UBlox GPS + Compass Module. http://ardupilot.org/copter/docs/common-installing-3dr-ublox-gps-compass-module.html. Accessed: 2016-05-10.

[74] Using an Airspeed Sensor. http://ardupilot.org/plane/docs/airspeed.html. Accessed: 2016-05-10.

[75] *Video/OSD kit*. 3D Robotics, June 2014. Technical manual.

[76] Skew Planar Wheel. SPW12 (1200-1360 MHz). https://www.circular-wireless.com/products-page/skew-planar-wheel/spw12r/. Accessed: 2016-05-10.

[77] GV-10 — 140W 10A Solar Charge Controller with MPPT. https://genasun.com/all-products/solar-charge-controllers/for-lead/gv-10-pb-10a-solar-charge-controller/. Accessed: 2016-05-10.

[78] Hyperion 3025 775 KV motor. http://www.scaleflying.com/Hyperian-3025-775-KV-motor_p_3611.html, . Accessed: 2016-05-10.

[79] Battery Hyperion G3 VX - 4200 mAh 3S (35C). http://www.rc-factory.eu/en/katalog/hyperion-battery-pack-248/hp-g3-vx-4200mah-3s-35c-1978.html. Accessed: 2016-10-17.

[80] 15"x8" F Propeller. http://www.apcprop.com/product_p/lp15012f.htm. Accessed: 2016-10-17.

[81] Graupner Brushless Control+ T 70 BEC G3,5 2-6S Drehzahlregler mit hott Telemetrie. https://www.lindinger.at/de/flugzeuge/antriebe-elektro/regler/graupner-brushless-control-t-70-bec-g3-5-2-6s-drehzahlregler-mit-hott-telemetrie. Accessed: 2016-05-10.

[82] A. Weider, H. Levy, I. Regev, L. Ankri, T. Goldenberg, Y. Ehrlich, A. Vladimirsky, Z. Yosef, and M. Cohen. SunSailor: Solar Powered UAV. Technical report, Faculty of Aerospace Engineering, Technion IIT, Haifa, Israel, 2006.

[83] Warren F. Phillips, A. B. Hansen, and W. M. Nelson. Effects of Tail Dihedral on Static Stability. *Journal of Aircraft*, 43(6), November - December 2006.

[84] Mark Drela. Xfoil: An analysis and design system for low reynolds number airfoils. In *Conference on Low Reynolds Number Airfoil Aerodynamics*, University of Notre Dame, June 1989.

[85] André Deperrois. *xflr5 Analysis of airfoils and wings at low Reynolds numbers*, 2013. Technical manual.

[86] Bernard Etkin and Lloyd Reid. *Dynamics of Flight Stability and Control*. John Wiley & Sons Ltd., third edition, 1996.

[87] José Azinheira. Controlo de voo, May 2010. IST.

[88] Thomas C. Corke. *Design of Aircraft*. Pearson Education, 2003. ISBN 13: 978-0130892348.

[89] APC Performance Data Files. https://www.apcprop.com. Accessed: 2016-04-05.

[90] Hyperion Zs30 Series Motor Test Data. http://media.hyperion.hk/dn/zs/ZS30propdata.pdf, . Accessed: 2016-05-15.

[91] John D. Anderson. *Introduction to Flight*. McGraw-Hill, fifth edition, 2005.

[92] Federal Aviation Administration. Federal aviation regulations - part 23 - airworthiness standards: Normal, utility, acrobatic and commuter category airplanes - subpart c - structure, 2016.

[93] Daniel Raymer. *Aircraft Design: A Conceptual Approach*. American Institute of Aeronautics and Astronautics, second edition, 1992.

[94] Zeus Bessoni and Manuel Júnior. Structural design of mini-uavs with conventional and alternative materials. In *14th Brazilian Congress of Thermal Sciences and Engineering*. University of Brasilia, November 2012.

[95] John D. Anderson. *Aircraft Performance & Design*. McGraw-Hill, first edition, 1999.

[96] Jaroslav Hofierka and Marcel Suri. The solar radiation model for open source gis: implementation and applications. In *Proceedings of the Open source GIS - GRASS users conference*, Trento, Italy, September 2002.

[97] Fritz Kasten. The linke turbidity factor based on improved values of the integral Rayleigh optical thickness. *Solar Energy*, 53(3):239–244, March 1996.

[98] SoDa: Solar Energy Services for Professionals. http://www.soda-is.com. Accessed: 2016-04-05.

[99] Miguel Marques Borges. Design of an Apparatus for Wind Tunnel Tests of Electric UAV Propulsion Systems. Master's thesis, Instituto Superior Técnico, June 2015.

[100] Associação Portuguesa de Aviação Ultraleve. Pistas em Portugal - O Roteiro. http://roteiro.apau.org/zpistas_in1.html. Accessed: 2016-04-05.

Appendix A

ISA Data on Portuguese Landscape

#	Location	h [m]	T_0 [K]	p [kPa]	$\rho\ [kg/m^3]$	a [m/s]	$\mu_0\ [kg/m.s.10^5]$
-	Sea level	0	288.15	101.325	1.225	340.3	1.812
1	Portimão	1.5	288.14	101.307	1.225	340.3	1.812
2	Braga	75	287.66	100.427	1.216	340.0	1.810
3	Cascais	99	287.51	100.141	1.213	339.9	1.809
4	Coimbra	179	286.99	99.193	1.204	339.6	1.806
5	Maia	230	286.66	98.592	1.198	339.4	1.805
6	Évora	246	286.55	98.404	1.196	339.3	1.804
7	Seia	433	285.34	96.230	1.175	338.6	1.798
8	Viseu	628	284.07	94.005	1.153	337.9	1.792
9	Bragança	683	283.71	93.385	1.147	337.7	1.790
10	Pampilhosa da Serra	808	282.90	91.988	1.133	337.2	1.786
-	Portugal average altitude	370	285.74	96.958	1.182	338.9	1.800
-	Project cruise altitude	1300	279.7	86.652	1.008	335.3	1.769

Table A.1: International Standard Atmosphere parameters in Portuguese municipal airfields [100].

Figure A.1: Small airfield locations in Portugal

Appendix B

Analytic Hierarchy Process Tables

The present appendix contains pairwise comparison matrices of alternatives, shown in Tables B.1 - B.10, whose results are summarized in figure B.1. The matrix that provides the final ranking of alternatives is also registered, in Table B.11.

	i	ii	iii	iv	v	vi	vii	viii	Priority Vector	Rank
i	1	1/9	1/9	1/9	1/9	1/9	1/9	1/9	0.0142	8
ii	9	1	1/2	1	1/5	2	3	5	0.1298	3
iii	9	2	1	2	1/3	2	3	5	0.1746	2
iv	9	1	1/2	1	1/3	1	3	5	0.1244	4
v	9	5	3	3	1	5	5	7	0.3580	1
vi	9	1/2	1/2	1	1/5	1	2	3	0.0946	5
vii	9	1/3	1/3	1/3	1/5	1/2	1	2	0.0618	6
viii	9	1/5	1/5	1/5	1/7	1/3	1/2	1	0.0426	7
$\gamma_{max} = 8.6930$ $\quad CI = 0.0990$ $\quad CR = 0.0702$										
i - Quadcopter $\quad$ ii - Conventional Airplane $\quad$ iii - Tractor T-tail $\quad$ iv - Pusher T-tail $\quad$ v - Pusher V-tail $\quad$ vi - Double boom pusher $\quad$ vii - Double boom tractor high tail $\quad$ viii - Double boom tractor low tail										

Table B.1: Domination measure of one configuration over another with respect to Aerodynamics.

	i	ii	iii	iv	v	vi	vii	viii	Priority Vector	Rank
i	1	1/7	1/7	1/7	1/7	1/5	1/5	1/5	0.0195	8
ii	7	1	2	3	2	5	5	5	0.2811	1
iii	7	1/2	1	2	2	5	5	5	0.2202	2
iv	7	1/3	1/2	1	1	5	5	5	0.1634	4
v	7	1/2	1/2	1	1	5	5	5	0.1689	3
vi	5	1/5	1/5	1/5	1/5	1	1	1/2	0.0444	6
vii	5	1/5	1/5	1/5	1/5	1	1	1/2	0.0444	6
viii	5	1/5	1/5	1/5	1/5	2	2	1	0.0581	5
$\gamma_{max} = 8.6090$ $\quad CI = 0.0870$ $\quad CR = 0.0617$										
i - Quadcopter $\quad$ ii - Conventional Airplane $\quad$ iii - Tractor T-tail $\quad$ iv - Pusher T-tail $\quad$ v - Pusher V-tail $\quad$ vi - Double boom pusher $\quad$ vii - Double boom tractor high tail $\quad$ viii - Double boom tractor low tail										

Table B.2: Domination measure of one configuration over another with respect to Structures and Weight.

	i	ii	iii	iv	v	vi	vii	viii	Priority Vector	Rank
i	1	3	3	3	3	5	5	5	0.3205	1
ii	1/3	1	1/2	2	2	3	3	3	0.1456	3
iii	1/3	2	1	2	2	3	3	3	0.1739	2
iv	1/3	1/2	1/2	1	1	3	3	3	0.1101	4
v	1/3	1/2	1/2	1	1	3	3	3	0.1101	4
vi	1/5	1/3	1/3	1/3	1/3	1	1	1	0.0466	6
vii	1/5	1/3	1/3	1/3	1/3	1	1	1	0.0466	6
viii	1/5	1/3	1/3	1/3	1/3	1	1	1	0.0466	6
$\gamma_{max} = 8.2339$ $\quad CI = 0.0334$ $\quad CR = 0.0237$										
i - Quadcopter $\quad$ ii - Conventional Airplane $\quad$ iii - Tractor T-tail										
iv - Pusher T-tail $\quad$ v - Pusher V-tail $\quad$ vi - Double boom pusher										
vii - Double boom tractor high tail $\quad$ viii - Double boom tractor low tail										

Table B.3: Domination measure of one configuration over another with respect to Manufacturing and Maintenance.

	i	ii	iii	iv	v	vi	vii	viii	Priority Vector	Rank
i	1	1/9	1/9	1/9	1/9	1/9	1/9	1/9	0.0147	8
ii	9	1	1	3	2	3	1	1	0.1720	3
iii	9	1	1	3	2	3	1	1	0.1720	3
iv	9	1/3	1/3	1	1/3	1/2	1/5	1/5	0.0533	7
v	9	1/2	1/2	3	1	2	1/3	1/3	0.0988	5
vi	9	1/3	1/3	2	1/2	1	1/5	1/5	0.0655	6
vii	9	1	1	5	3	5	1	1	0.2118	1
viii	9	1	1	5	3	5	1	1	0.2118	1
$\gamma_{max} = 8.4514$ $\quad CI = 0.0645$ $\quad CR = 0.0457$										
i - Quadcopter $\quad$ ii - Conventional Airplane $\quad$ iii - Tractor T-tail										
iv - Pusher T-tail $\quad$ v - Pusher V-tail $\quad$ vi - Double boom pusher										
vii - Double boom tractor high tail $\quad$ viii - Double boom tractor low tail										

Table B.4: Domination measure of one configuration over another with respect to Propulsion.

	i	ii	iii	iv	v	vi	vii	viii	Priority Vector	Rank
i	1	1/9	1/9	1/9	1/9	1/9	1/9	1/9	0.0146	8
ii	9	1	1	2	5	5	3	3	0.2624	1
iii	9	1	1	2	3	5	3	3	0.2466	2
iv	9	1/2	1/2	1	2	2	1/2	1/2	0.1026	5
v	9	1/3	1/5	1/2	1	1	1/2	1/2	0.0671	6
vi	9	1/5	1/5	1/2	1	1	1/2	1/2	0.0632	7
vii	9	1/3	1/3	2	2	2	1	1/2	0.1113	4
viii	9	1/3	1/3	2	2	2	2	1	0.1321	3
$\gamma_{max} = 8.4889$ $\quad CI = 0.0698$ $\quad CR = 0.0495$										
i - Quadcopter $\quad$ ii - Conventional Airplane $\quad$ iii - Tractor T-tail										
iv - Pusher T-tail $\quad$ v - Pusher V-tail $\quad$ vi - Double boom pusher										
vii - Double boom tractor high tail $\quad$ viii - Double boom tractor low tail										

Table B.5: Domination measure of one configuration over another with respect to Stability and Control.

	i	ii	iii	iv	v	vi	vii	viii	Priority Vector	Rank
i	1	1/7	1/7	1/7	1/7	1/7	1/7	1/7	0.0194	8
ii	7	1	1/2	1/2	1	1/3	1/3	1/3	0.0736	6
iii	7	2	1	1	2	1/2	1/2	1	0.1281	4
iv	7	2	1	1	2	1/2	1/2	1	0.1281	4
v	7	1	1/2	1/2	1	1/3	1/3	1/2	0.0766	6
vi	7	3	2	2	3	1	1	1	0.2033	2
vii	7	3	2	2	3	1	1	2	0.2215	1
viii	7	3	1	1	2	1	1/2	1	0.1494	3

$\gamma_{max} = 8.2277 \quad CI = 0.0325 \quad CR = 0.0231$

i - Quadcopter   ii - Conventional Airplane   iii - Tractor T-tail
iv - Pusher T-tail   v - Pusher V-tail   vi - Double boom pusher
vii - Double boom tractor high tail   viii - Double boom tractor low tail

Table B.6: Domination measure of one configuration over another with respect to Solar Panels Integration.

	i	ii	iii	iv	v	vi	vii	viii	Priority Vector	Rank
i	1	7	7	2	2	2	7	7	0.3055	1
ii	1/7	1	1	1/5	1/5	1/5	1	1	0.0378	5
iii	1/7	1	1	1/5	1/5	1/5	1	1	0.0378	5
iv	1/2	5	5	1	1	1	5	5	0.1810	2
v	1/2	5	5	1	1	1	5	5	0.1810	2
vi	1/2	5	5	1	1	1	5	5	0.1810	2
vii	1/7	1	1	1/5	1/5	1/5	1	1	0.0378	5
viii	1/7	1	1	1/5	1/5	1/5	1	1	0.0378	5

$\gamma_{max} = 8.0240 \quad CI = 0.0034 \quad CR = 0.0024$

i - Quadcopter   ii - Conventional Airplane   iii - Tractor T-tail
iv - Pusher T-tail   v - Pusher V-tail   vi - Double boom pusher
vii - Double boom tractor high tail   viii - Double boom tractor low tail

Table B.7: Domination measure of one configuration over another with respect to Remote-Person View integration.

	i	ii	iii	iv	v	vi	vii	viii	Priority Vector	Rank
i	1	5	5	5	5	5	5	5	0.4020	1
ii	1/5	1	1	1/3	1/3	1/3	2	2	0.0618	5
iii	1/5	1	1	1/3	1/3	1/3	2	2	0.0618	5
iv	1/5	3	3	1	1	1	2	2	0.1210	3
v	1/5	3	3	1	1	2	3	3	0.1456	2
vi	1/5	3	3	1	1/2	1	2	2	0.1124	4
vii	1/5	1/2	1/2	1/2	1/3	1/2	1	1	0.0477	7
viii	1/5	1/2	1/2	1/2	1/3	1/2	1	1	0.0477	7

$\gamma_{max} = 8.4383 \quad CI = 0.0626 \quad CR = 0.0444$

i - Quadcopter   ii - Conventional Airplane   iii - Tractor T-tail
iv - Pusher T-tail   v - Pusher V-tail   vi - Double boom pusher
vii - Double boom tractor high tail   viii - Double boom tractor low tail

Table B.8: Domination measure of one configuration over another with respect to Payload Volume.

	i	ii	iii	iv	v	vi	vii	viii	Priority Vector	Rank
i	1	7	7	7	7	7	7	7	0.4769	1
ii	1/7	1	1/3	1/3	1/2	2	2	3	0.0647	5
iii	1/7	3	1	1	2	2	2	5	0.1205	2
iv	1/7	3	1	1	2	2	2	5	0.1205	2
v	1/7	2	1/2	1/2	1	3	2	2	0.0817	4
vi	1/7	1/2	1/2	1/2	1/3	1	1/3	1/2	0.0374	7
vii	1/7	1/2	1/2	1/2	1/2	3	1	3	0.0627	5
viii	1/7	1/3	1/5	1/5	1/2	2	1/3	1	0.0357	7
$\gamma_{max} = 8.6768$ $\quad$ $CI = 0.0967$ $\quad$ $CR = 0.0686$											
i - Quadcopter $\quad$ ii - Conventional Airplane $\quad$ iii - Tractor T-tail iv - Pusher T-tail $\quad$ v - Pusher V-tail $\quad$ vi - Double boom pusher vii - Double boom tractor high tail $\quad$ viii - Double boom tractor low tail											

Table B.9: Domination measure of one configuration over another with respect to Take-off and Landing.

	i	ii	iii	iv	v	vi	vii	viii	Priority Vector	Rank
i	1	1/5	1/5	1/5	1/5	1/5	1/5	1/5	0.0252	8
ii	5	1	1/2	1/2	1	5	5	5	0.1711	3
iii	5	2	1	1	2	5	5	5	0.2375	1
iv	5	2	1	1	2	5	5	5	0.2375	1
v	5	1	1/2	1/2	1	5	5	5	0.1711	3
vi	5	1/5	1/5	1/5	1/5	1	1	2	0.0564	5
vii	5	1/5	1/5	1/5	1/5	1	1	2	0.0564	5
viii	5	1/5	1/5	1/5	1/5	1/2	1/2	1	0.0448	7
$\gamma_{max} = 8.7274$ $\quad$ $CI = 0.1039$ $\quad$ $CR = 0.0737$											
i - Quadcopter $\quad$ ii - Conventional Airplane $\quad$ iii - Tractor T-tail iv - Pusher T-tail $\quad$ v - Pusher V-tail $\quad$ vi - Double boom pusher vii - Double boom tractor high tail $\quad$ viii - Double boom tractor low tail											

Table B.10: Domination measure of one configuration over another with respect to Portable Capabilities.

	A	B	C	D	E	F	G	H	I	J	Priority Vector	Rank
	(0.193)	(0.199)	(0.022)	(0.129)	(0.044)	(0.201)	(0.110)	(0.028)	(0.038)	(0.036)		
i	0.0142	0.0195	0.3205	0.0147	0.0146	0.0194	0.3055	0.4020	0.4769	0.0252	0.0839	8
ii	0.1298	0.2811	0.1456	0.1720	0.2624	0.0736	0.0378	0.0618	0.0647	0.1711	0.1472	3
iii	0.1746	0.2202	0.1739	0.1720	0.2466	0.1281	0.0378	0.0618	0.1205	0.2375	0.1592	2
iv	0.1244	0.1634	0.1101	0.0533	0.1026	0.1281	0.1810	0.1210	0.1205	0.2375	0.1326	4
v	0.3580	0.1689	0.1101	0.0988	0.0671	0.0766	0.1810	0.1456	0.0817	0.1711	0.1695	1
vi	0.0946	0.0444	0.0466	0.0655	0.0632	0.2033	0.1810	0.1124	0.0374	0.0564	0.1068	6
vii	0.0618	0.0444	0.0466	0.2118	0.1113	0.2215	0.0378	0.0477	0.0627	0.0564	0.1084	5
viii	0.0426	0.0581	0.0466	0.2118	0.1321	0.1494	0.0378	0.0477	0.0357	0.0448	0.0924	7

A - Aerodynamics   B - Structural Design   C - Manufacturing and Maintenance

D - Propulsion   E - Stability and Control   F - Solar Panels Integration   G - RPV integration

H - Payload Volume   I - Take-off and landing Adaptability   J - Portable Capabilities

i - Quadcopter   ii - Conventional Airplane   iii - Tractor T-tail

iv - Pusher T-tail   v - Pusher V-tail   vi - Double boom pusher

vii - Double boom tractor high tail   viii - Double boom tractor low tail

Table B.11: Local and Global priority weights.

a: Aerodynamics

b: Structures and Weight

c: Manufacturing and Maintenance

d: Propulsion

e: Stability and Control

f: Solar Panels Integration

g: RPV Integration

h: Payload Volume
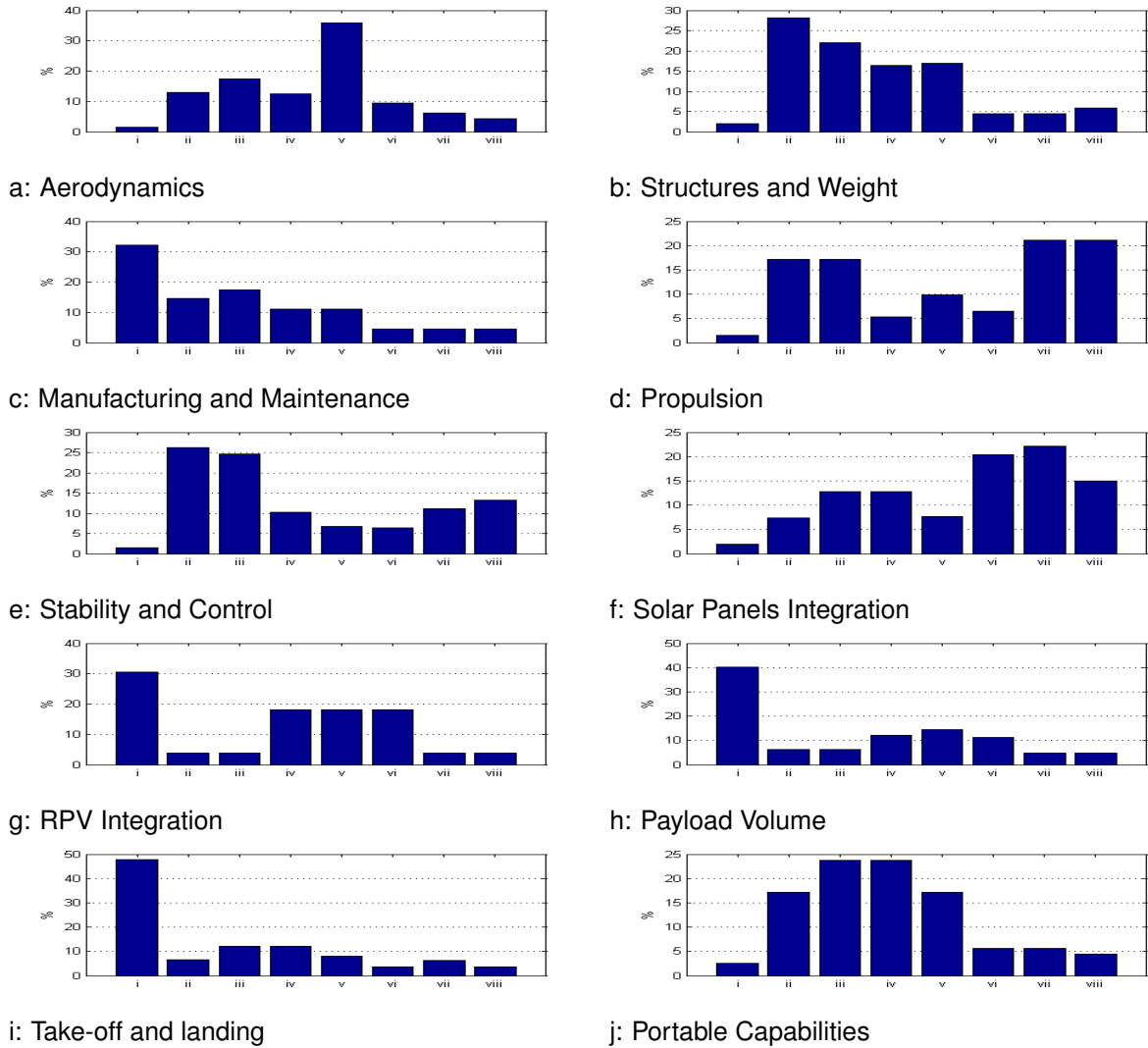
i: Take-off and landing

j: Portable Capabilities

Figure B.1: Local priority vector results

Appendix C

Database of Similar Aircraft

This appendix contains a tabulated database listing all researched aircraft that have been used to obtain the empty weight correlation model illustrated in figure 3.17.

Aircraft	Wing Area (dm^2)	Empty Weight (g)	Source	Wing Type
Shinto EL	55.59	1804	f3j.in.ua	
Soarmaster Compact	58.8	1663.2	www.icare-rc.com	
FS 4000	66.95	2900	www.sport-klemm.de	
Electra 2	68.8	999	www.mibomodeli.com	
Supra Expert EL	69.34	1280	f3j.in.ua	
Graphite 2 EL	69.5	1390	f3j.in.ua	
Stork 4e F5J	73	1635.8	www.soaringusa.com	Fully Molded
Maxa Pro EL	73.84	1508.5	f3j.in.ua	Construction
Dynamic F3J	75.16	1530	www.fvk.de	
Spectra	79	1500	www.mibomodeli.com	
Maxa Pro EL	82.15	1633.5	f3j.in.ua	
Xplorer E 4.0 ST Lite	86.71	1474	www.soaringusa.com	
Royale	88	1276	www.mapleleafdesign.com	
Shark XL	97	4180	www.tun.ch	
Thermik XXXLe 5M	104.257	4167	www.soaringusa.com	
Alpina 2501	32.1	900	www.tun.ch	
Alpina PRO 3001	48.2	1625	www.tangent-modelltechnik.de	
Thermik Dream	60.9	1798	www.topmodelcz.cz	
Rival Abachi	62	1470	www.fvk.de	
Novus Abachi 2	67	1660	www.fvk.de	Foam Core
Ideal V	67.6	1541	www.topmodelcz.cz	Construction
CULT	72	2039	www.tangent-modelltechnik.de	
Fascination V	76.7	1941	www.topmodelcz.cz	
ALPINA 4001 Champ	80.6	3525	www.tangent-modelltechnik.de	
VORTEX Mach I	91	3859	www.tangent-modelltechnik.de	
Alpina 5001 PRO	96.4	4234.3	www.tun.ch	
Vertigo	43	750	www.airtech-rc.com	
Marabu V	48.7	805	www.airtech-rc.com	
Magellan-110	50	926.5	www.icare-rc.com	
Ultrafly	55	889	www.airtech-rc.com	
Topaz SV2-E	59.9	752.2	www.skipmillermodels.com	
Rival Rippe	62	1170	www.fvk.de	
Albatros 3.0	67.8	1134	www.topmodelcz.cz	
AVA PRO EL	67.9	960	f3j.in.ua	
Gracia	70.4	1184	www.icare-rc.com	
Pulsar PRO 3200 E	70.5	880	www.soaringusa.com	
Pulsar PRO 3200 E	70.5	880	www.soaringusa.com	Rib
Gracia MAXI	80.1	1314	www.topmodelcz.cz	Construction
Pulsar PRO 3600 E	80.5	970	www.soaringusa.com	
AVA PRO EL	82.3	1125	f3j.in.ua	
AVA PRO EL	85.62	1145	f3j.in.ua	
Pulsar PRO 4000 E	85.7	1050	www.soaringusa.com	
Sky-Sailor	78.7	748.6	Noth [46]	
SunSailor	135	1900.6	Weider et al. [82]	
Atlantik Solar	172	1942	ICRA 2015 [50]	
LEEUAV 1st gen.	148.5	2358.61	Cândido [58]	

Table C.1: Researched aircraft data.